Development of a remote sensing-based evapotranspiration model for monitoring crop water use and yield estimation in rainfed systems

Report to the
Water Research Commission

By

N. P. Majozi[1], C. R. Masemola[1], A. Ramoelo[2], S. Madonsela[1], M. Cho[1],

[1]Precision Agriculture, Advanced Agriculture and Food Cluster, CSIR
[2]Earth Observation Programme, South African National Space Agency, Pretoria, South Africa

WRC Report no. 3226/1/25
ISBN 978-0-6392-0733-9

September 2025

Obtainable from

Water Research Commission
Private Bag X03
Gezina, 0031

hendrickm@wrc.org.za or download from www.wrc.org.za

This report emanates from a project titled:
Development of a remote sensing-based evapotranspiration model for monitoring crop water use and yield estimation in rainfed systems (WRC Project No. C2022/2023-00957)

Executive summary

Background

Rainfed agriculture, which dominates in the Sub-Saharan African region, faces heightened risk due to its vulnerability to climate change and limited adaptive capacity. South Africa's agricultural sector is already affected by multiple stressors, including water scarcity, changing pest and disease profiles, rising input costs, and a diminishing interest among young people in farming. Enhancing agricultural productivity, through increased output per unit of land and water, is critical to ensuring food security and economic growth. The United Nations Sustainable Development Goals (SDGs), particularly Goals 1, 2, 6, 12, and 13, and South Africa's National Development Plan (NDP), emphasise sustainable agriculture, water-use efficiency, and food security. Achieving these goals requires timely, data-driven decision-making, particularly for smallholder and emerging farmers who operate under resource constraints.

Remote sensing technologies provide scalable, spatially explicit data that are essential for monitoring crop conditions, water use, and productivity. Advances in satellite imagery, drones, cloud computing, machine learning (ML), and artificial intelligence (AI) have enabled the development of smart agriculture systems. These systems form part of the Fourth Industrial Revolution (4IR), offering real-time monitoring and decision support through spatial intelligence and predictive analytics. Several platforms have been developed to monitor agricultural parameters, such as WaPOR, eLeaf, and AFGRI GeoAgro. However, many of these operate on a user-pays model, are oriented toward large-scale commercial farms, or lack the spatial resolution required for smallholder plots. Open-source platforms like Sen2Agri and its successor Sen4Stat have shown potential for cropland mapping, though they face limitations related to regional stratification, crop classification accuracy, and system compatibility with national standards.

Aims

Against this backdrop, the purpose of the project sought to address multi-component objectives within the agricultural and geospatial domains of South Africa: i) Delineation of smallholder agricultural field boundaries across diverse topographies and agroecological zones; ii) Mapping of maize crop evapotranspiration (ET) using remote sensing and meteorological data for selected sites in Gauteng Province; and iii) Development of a geospatial tool for field-scale crop water use monitoring on a cloud computing platform.

Methods

The project began with a comprehensive literature review to assess the state of knowledge and existing methodologies related to field boundary mapping, remote sensing-based ET estimation, and geospatial tool development.

To address the first objective, the study developed and tested a deep learning-based approach using a residual U-Net architecture with topographic attention. The model was trained on manually digitised field boundaries across several provinces, incorporating both spectral and topographic features. A national model was compared against province-specific models. The second objective of the project assessed ET estimation in selected maize-growing sites in Gauteng Province, using a combination of the Penman-Monteith (PM) model, driven by meteorological data from South African Weather Service (SAWS) stations, and medium to high-resolution ET products, including WaPOR and ECOSTRESS. An additional component investigated remote sensing-based maize yield prediction. Traditional crop growth models were reviewed but were found to be data-intensive, limiting their applicability in smallholder systems with limited ground data. Finally, there was integration of the ET model into a cloud computing platform to support field-scale crop water use monitoring. Google Earth Engine (GEE) was selected due to its capacity to handle large geospatial datasets and perform real-time processing. The development process involved transferring the ET model workflows to GEE and evaluating existing platforms to identify if they were aligned with end-user needs, including farmers, researchers, and policymakers.

Main findings

The main outcomes of the project are summarised as follows:

A novel deep learning approach using a residual U-Net architecture with topographic attention was developed to accurately delineate smallholder field boundaries across diverse agro-ecological zones in South Africa. The model demonstrated high generalisation capacity, achieving: Mean Intersection over Union (IoU): ~0.81, Boundary F1-score: ~0.78

The national model performed robustly across most provinces, outperforming or matching province-specific models. However, in areas with complex topography (e.g., >25° slope), localised fine-tuning further improved accuracy. This approach provides a scalable, transferable solution for mapping fragmented agricultural parcels in other data-scarce regions.

The Penman-Monteith (PM) model was employed to estimate maize evapotranspiration (ET), supported by meteorological data and validated against global remote sensing ET products (WaPOR and ECOSTRESS). Key findings include: i) estimated maize ET ranged from 0.17 mm/day to 6.63 mm/day during peak growth. WaPOR and ECOSTRESS showed similar seasonal ET patterns, although ECOSTRESS had limited observations. PM-based ET maps revealed greater spatial detail, important for detecting within-field variability. The comparison underscored the potential of integrating ground-based and remote sensing data for high-resolution water use assessments, essential for informed irrigation planning and drought monitoring. The workflow was implemented on Google Earth Engine (GEE), enabling scalable processing and visualisation of large remote sensing datasets for maize crop water use estimation and monitoring.

General Conclusion

This project highlighted the need for a comprehensive method to delineate our small-scale fields, considering the complexity of the South African climate and topography. The residual U-Net with topographic attention proved to be highly accurate in delineating field boundaries across all provinces. The study concludes that a single national model, augmented with lightweight terrain-specific adapters, can satisfy operational accuracy thresholds while simplifying maintenance workflows; full retraining is warranted only in topographic outliers. The proposed methodology provides a transferable blueprint for automated smallholder-parcel mapping in other data-scarce regions characterised by sharp relief and fragmented agriculture. On the other hand, the Penman-Monteith model was assessed against Priestley-Taylor JPL-driven ECOSTRESS ET and Penman-Monteith (PM) based ETLook-driven WaPOR ET in maize crop water use estimation. The study highlighted the importance of producing high resolution maps of crop water use, particularly for precise crop water monitoring. The PM evapotranspiration model was finally transferred to Google Earth Engine to develop a geospatial tool for monitoring crop water use. The platform's capabilities in handling large volumes of data and applying advanced analytical techniques make it an invaluable resource for enhancing agricultural water management.

New Knowledge and Innovation

Delineating smallholder parcels in rural South Africa presents a unique mix of challenges and variability, with fields characterised by very small, irregular plots. This challenge is further exacerbated by terrain and elevation, with regions like KwaZulu-Natal and the Eastern Cape characterised by rolling hills and steep valleys, where fields often appear as patchworks on slopes. In this project, a deep learning technique, i.e. the residual U-Net architecture with topographic attention, was employed to develop a highly accurate field delineation procedure for these complex South African fields. Meanwhile, the Penman-Monteith model was evaluated for estimating maize crop evapotranspiration. The model was further transferred to the Google Earth Engine platform as a geospatial tool for mapping crop evapotranspiration (ET) in smallholder croplands.

Capacity Building

The project adequately addressed institutional and individual capacity building. The project recruited one PhD student registered with the University of Pretoria. The student is still working on her studies and has been trained in project management, as well as programming and geospatial data utilisation for crop water use modelling. The results of the delineation of small-scale fields were presented at different international conferences, whereas the results of the maize ET modelling were presented at the Neofrontiers workshop in Pietermaritzburg.

Recommendations

- The proposed field delineation workflow should be validated across additional regions and agricultural contexts to test for transferability and robustness.
- South Africa lacks sufficient long-term, ground-based ET measurement stations, especially in small-scale agriculture regions. A national network with open data access is critical for crop model calibration and validation in these neglected areas.
- Most ET studies prioritise irrigated systems. Greater attention to ET dynamics in rainfed cropping systems is necessary, especially for semi-arid regions.
- The initial geospatial tool framework is in place, but further development must incorporate scalability to other crops and regions.

Acknowledgements

This report would not have been possible without the assistance and guidance of others. In particular, the project team would like to thank the following reference group members for their invaluable input and sage advice during the project:

Dr L Nhamo	Water Research Commission
Prof N S Mpandeli	Water Research Commission
Dr S N Hlophe-Ginindza	Water Research Commission
Dr B Petya	Water Research Commission
Dr J Magidi	Tshwane University of Technology
Prof E Mashimbye	Stellenbosch University
Mr T Newby	GeoTerra
Dr M Sibanda	University of the Western Cape
Dr G Ibrahim	International Water Management Institute

The project team is particularly grateful to:

- The Water Research Commission for funding this research, without which we would not have been able to carry it out.
- Prof Mashimbye, for his valuable insights during the reference group meetings and continued support relating to remote sensing and crop water use research.
- Ms N Mthethwa of the University of Pretoria, who contributed to this research project.
- Mr V Mahlangu, Mr W Sikhosana, and Mr Amos for granting us permission and access to their fields as project sites for this project

Finally, the project team would like to extend their appreciation to both Prof N. S. Mpandeli and Dr L. Nhamo for the professional way in which they managed this project. The project would not have materialised had it not been for their vision and understanding of the importance of agricultural water utilisation.

Table of Contents

Table of Tables

Table of Figures

Abbreviations/ Acronyms

4IR	Fourth Industrial Revolution
AI	Artificial intelligence
ALEXI (disALEXI)	Atmosphere Land Exchange model and the disaggregated form of the algorithm
ANN	Artificial neural networks
API	Application Programming Interface
AWS	Amazon Web Services
BC	Blaney-Criddle
BPNN	Backpropagation neural network
CERES	Crop Environment Resource Synthesis
CLI	Command Line Interface
DA	Dalton
DisALEXI-JPL	DisALEXI disaggregation scheme Atmosphere Land Exchange-Jet Propulsion Laboratory
DNN	deep neural network
DSSAT	Decision Support System for Agrotechnology Transfer
EB	Energy balance
EC	Addy covariance
ECMWF	European Centre for Medium-Range Weather Forecasts
ECMWF	European Centre for Medium-Range Weather Forecasts
ECO3ETALEXI	ECOSTRESS ET product derived using the ALEXI model
ECO3ETPTJPL	ECOSTRESS ET product derived using the PT-JPL model
ECOSTRESS	ECOsystem Spaceborne Thermal Radiometer Experiment on the Space Station
ER	Exponential regression
ERA5	ECMWF Reanalysis v5
ESA	European Space Agency
Etp/ ETa	Potential/ actual evapotranspiration
EVI	Enhanced Vegetation Index

EVI	Enhanced Vegetation Index
FAO	Food and Agriculture Organisation
GBDT	Gradient boosting decision tree
GDAS	Global Data Assimilation System
GLDAS	Global Land Data Assimilation System
GLEAM	Global Land Evaporation Amsterdam Model
GMAO	Global Modelling and Assimilation Office
GPU	Graphics processing unit
HA	Hargreaves
HID	Hetao Irrigation District
KGE	Kling–Gupta efficiency
KNN	K-Nearest Neighbours
LAI	Leaf area index
LAI	Leaf area index
LiDAR	Light Detection and Ranging
LIRF	Limited Irrigation Research Farm
LSA SAF	Satellite Applications Facility on Land Surface Analysis
ML	machine learning
MODIS	MODerate Resolution Imaging Spectroradiometer
MSR	multispectral radiometer
NAIP	National Agriculture Imagery Program
NCP	North China Plain
NDP	National Development Plan
NDRE	Normalised difference red edge index
NDVI	Normalised difference vegetation index
NDWI	Normalised difference water index
NLDAS	North American Land Data Assimilation System
PGF	Princeton Global Forcing
PLSR	Partial least squares regression

PML	Penman-Monteith-Leuning
PT	Priestley–Taylor
PT-JPL	Priestley Taylor-Jet Propulsion Laboratory
PT-JPL	Jet Propulsion Laboratory- Priestley Taylor
ReSEM	Remote Sensing-based cropland Ecohydrological Model
REST	Representational State Transfer
RFR	Random forest regression
RMSE	Root Mean Square Error
RS	Remote sensing
SDGs	Sustainable Development Goals
SEBS	Surface energy balance system
Sen4Stat	Sentinel-2 for Agricultural Statistics
SPOT 5	Satellite Pour l’Observation de la Terre- 5
SR	Symbolic regression
STAC	SpatioTemporal Asset Catalog
sUAS	small uncrewed aerial system
SVAT	Soil-Vegetation-Atmosphere Transfer
SVM/ R	Support vector machines/ regression
SW	Shuttleworth
TSEB	Two-Source Surface Energy Balance
UN	United Nations
USA	United States of America
WaPOR	Water Productivity through Open access of Remotely sensed derived data
WMS	Warehouse Management System
XGboost	Extreme gradient boosting algorithm

1. Introduction

1.1. Background

The African population alone is projected to grow to two billion people by 2050, resulting in immense pressure being further exerted on already strained water, energy, and food systems (Ali & Acquaye, 2024; Huntington et al., 2021). Humans need these resources to sustain their livelihoods, grow economies, and achieve sustainable development. This situation is further aggravated by factors such as the changing climate, where temperatures are expected to continue warming, and altered precipitation patterns, with some areas set to become drier, while others become wetter. This will increase risk and uncertainty, especially in a region heavily reliant on rainfed agriculture, that lacks resources to adapt, has poor infrastructure, lacks institutional arrangements, and has low adaptive capacity. Research shows that Southern Africa will experience a hotter and drier climate, as precipitation declines and temperatures rise (Ali & Acquaye, 2024; Nhamo et al., 2019). It is further reported that climate change will result in a reduction in agricultural land productivity of over 50% in southern Africa by 2050 (Field & Barros, 2014; Mperejekumana et al., 2024; Nhamo et al., 2020). The Intergovernmental Panel on Climate Change (IPCC) estimates that by 2050, 350–600 million people in Africa will be at risk of increased water stress due to rainfall variability (AR, 2014).

The increasing stress on water resources, coupled with the energy and food sectors' reliance on them, underscores the need for policymakers and stakeholders across all three sectors to leverage available knowledge and emerging technologies. This will be essential for enhancing water resource management, boosting agricultural production, and ecosystem conservation (Ferroukhi et al., 2015). Given the interconnected nature of these sectors, an integrated approach is crucial to ensuring water and food security while promoting sustainable agriculture and energy production. The South African agricultural sector is also increasingly challenged by climate change, water scarcity, the rise of new pests and diseases, escalating input costs, and a lack of interest from younger generations in farming. To ensure national food security despite these obstacles, there is a critical need to enhance agricultural productivity by producing more and/or higher-quality products per unit of land and water.

Moreover, the United Nations' (UN) Sustainable Development Goals (SDGs) 1, 2, 6, 12 and 13- focused on poverty reduction, zero hunger, water use efficiency, water resource management, and sustainable consumption and production- aim to enhance food and water security by increasing agricultural productivity and optimizing water use, in the backdrop of a changing climate. These efforts are intended to mitigate water scarcity, ensure sustainable agricultural production and support the growing global population. Similarly, South Africa's National Development Plan (NDP) seeks to drive economic growth across multiple sectors, including agriculture, with a particular emphasis on improving productivity for smallholder and emerging farmers. As a result, there is an increasing focus on mapping croplands and crop types, as well as assessing crop water requirements and usage, to enhance agricultural water management (Cai et al., 2011).

Remote sensing technology offers detailed and repeatable spatial data at various scales, essential for monitoring field productivity and providing information that helps managers and policymakers make informed, timely decisions for targeted management strategies (Tariq et al., 2023). The advancement of drone and satellite remote sensing technologies, resulting in the emergence of "Big Data", has been complemented by advances in computing, high-speed internet, machine learning (ML), and artificial intelligence (AI). When properly utilised, these innovations present significant opportunities for agricultural production, particularly through smart agriculture. These innovations are key components of the Fourth Industrial Revolution (4IR), which integrates physical and digital systems to enhance automation and interoperability. The adoption of 4IR technologies in agriculture, including spatial intelligence and predictive analytics, enables more effective monitoring of soil health, crop conditions, and water usage. Consistently updated, reliable satellite-derived cropland maps are crucial for developing crop monitoring and early warning systems, facilitating analyses such as crop inventories, status assessments, water usage tracking, and yield forecasting. Also, integrating these maps with datasets on soil conditions, agronomic practices, and climate can help identify and address gaps in crop and water productivity. This information supports farmers and extension officers in understanding variations in crop growth and water usage within their fields, ultimately leading to informed interventions that boost yields and overall productivity.

Significant efforts have been dedicated to developing remote sensing-based geospatial tools for crop monitoring, assessing crop water use, and predicting crop yield and biomass. The Food and Agriculture Organisation's WaPOR platform provides remote sensing-based data on land use, biomass, and vegetation water use to monitor agricultural water productivity. The platform has, to date, updated its national datasets' spatial resolution from 250 to 100 m, which still presents a challenge for smaller farms and high-level crop water monitoring in South Africa. The Department of Agriculture and Rural Development's Agriculture Census and Baseline Mapping project has mapped croplands using SPOT 5 satellite imagery, a costly solution. Other systems like the AFGRI GeoAgro platform, which offers maps for seeding, crop information, fertilisation, and yield, and the eLeaf platform, which provides insights into crop growth, water use, and yield estimates, serve the agricultural community. However, these platforms often operate on a user-pays model and are primarily targeted at large-scale commercial farmers engaged in irrigated agriculture. The ESA-funded Sentinel-2 for Agricultural Statistics (Sen4Stat) open-source processing system (https://www.esa-sen4stat.org/), the successor of Sen2Agric, uses Sentinel-2 and Landsat 8 imagery for crop monitoring at 10 m and improves the gathering of agricultural statistics (Ambrosio et al., 2023).

Evaluations of the Sen2Agri platform in South Africa reported performance issues due to inadequate regional stratification, combining differing agro-climatic conditions, and mismatches between the Sen2Agri system and national crop nomenclature. Another ESA-funded initiative, the Sentinels for Evapotranspiration (Sen-ET), is a plugin for the SNAP open-source software. While Sen4Stat focuses on cropland and crop type mapping, Sen-ET and its successor ET4FAO provide evapotranspiration and water productivity data. Given these challenges, the proposed research aimed to consolidate and enhance remote sensing data to monitor crop water use, improve water resource management, and forecast yields. This was achieved by developing a remote sensing-based decision support system to delineate crop fields, estimate crop water use, and forecast crop yields. The tool is designed to be easily accessible to medium-scale farmers, extension officers, and water managers to assist in the early detection of growth disparities and water use variations within fields, enabling timely interventions that can improve yields.

1.2. Project Objectives

The primary goal of this project was to develop a remote sensing-based geospatial platform for monitoring crop water use and estimating crop yield. This overarching aim was addressed through the following specific objectives:

1. Literature review: Compile and synthesise existing national and international studies and geospatial systems focused on crop field delineation, maize crop water use, and yield estimation.
2. Remote sensing analysis in selected South African regions:
   - Delineate crop fields and define their spatial extent,
   - Derive spatially and temporally representative estimates of evapotranspiration (ET),
   - Model crop yield estimates based on remote sensing indicators.
3. Geospatial system integration: Integrate the various components—field boundaries, crop type classification, water use data, and yield estimation models—into a unified geospatial platform for monitoring crop development, water consumption, and yield at the field scale.

1.3. Report Structure

The project was structured into four main phases:

i. Crop field delineation
ii. Maize evapotranspiration assessment
iii. Maize yield prediction
iv. Development of the geospatial monitoring tool

Each phase began with a literature review to provide context, followed by the methodology, results, and a discussion of findings. Chapter 2 details the process of delineating smallholder crop fields across diverse South African landscapes. Particular attention is given to the challenges posed by varied terrain, which complicates the automated digitisation of small field parcels. Chapter 3 evaluates maize evapotranspiration using the Penman-Monteith approach as adapted by Mu et al. (2007, 2011). These estimates were compared against ET products from WaPOR, and ECOSTRESS ET maps generated by the Penman-Monteith model were analysed across key maize growth stages and cross-compared with the remote sensing-based ET datasets. Chapter 4 presents maize yield predictions derived from NDVI-based models. Chapter 5 outlines the development and integration of the geospatial tool, combining the outputs of previous phases into a cohesive platform for field-level crop monitoring and yield estimation.

2. Terrain-Aware Deep Learning Delineation of Smallholder Farm Parcels across South Africa: Evaluating a Unified National Model versus Province-Specific Alternatives

2.1. General overview

2.1.1. Challenges in Delineating Small, Irregular Parcels

Mapping the boundaries of smallholder agricultural parcels is inherently challenging due to the nature of these fields. Smallholder parcels are often very small in size (on the order of a few hectares or less) and have irregular, non-uniform shapes. They frequently involve mixed-cropping or intercropping systems, meaning a single parcel may contain multiple crop types or planting patterns. As a result, the boundaries between fields are vaguely defined and sometimes not marked by strong physical boundaries (Fritz et al., 2019; Persello et al., 2019). In high-resolution satellite or aerial imagery, one does not always see clear dividing lines, such as fences or roads separating adjacent small plots. Instead, delineating the field edges requires detecting subtle transitions in texture and vegetation patterns. Standard edge-detection algorithms often fail on such imagery because the physical edges between smallholder fields are indistinct and can be easily confused with within-field variation (Yan & Roy, 2020). This challenge is further exacerbated in complex terrains – for example, hilly or mountainous regions where illumination differences (shadows, sun-facing vs. shaded slopes) and heterogeneous natural vegetation can obscure or mimic field boundaries. In such terrains, fields may follow topographic contours, resulting in non-rectilinear shapes that confound simple geometric assumptions (Fritz et al., 2019). Globally, these issues are common in smallholder-dominated landscapes across Africa, Asia, and Latin America, making automated parcel delineation a difficult task. Many regions of the world lack up-to-date cadastral maps or Land Parcel Identification Systems, so remote sensing is looked to as a solution, yet the above factors pose significant obstacles to reliable field boundary extraction (Yan & Roy, 2020).

A fundamental factor in delineating small fields is the spatial resolution of imagery. Simply put, you cannot reliably delineate what you cannot see. Coarser-resolution satellites like Landsat (30 m per pixel) often blur multiple small fields into a single pixel, eliminating any chance to detect individual parcel boundaries (Xiong et al., 2017). Even moderate resolution imagery, such as Sentinel-2 (10 m), can be insufficient when parcels are extremely small or narrow. For instance, fields in certain densely cultivated smallholder regions (e.g., parts of South Asia or West Africa) may only be a few tens of meters across, making their boundaries only one or two pixels wide in Sentinel-2 data. Comparative studies highlight this issue: fields that are distinguishable in high-resolution imagery become progressively harder to discern as resolution coarsens (Fritz et al., 2019).

Historically, the availability of very high resolution (VHR) satellite imagery (sub-5 m resolution) was limited and expensive, restricting its use to local case studies. Public programs like Landsat and Sentinel provided broad coverage but at resolutions more suitable for larger commercial fields. Only recently has this gap begun to close, with the launch of constellations like PlanetScope (3–5 m) and the integration of commercial basemaps into analysis platforms (Yan & Roy, 2020). Now, platforms such as Google Earth (which aggregates imagery from providers like Maxar) or Airbus OneAtlas offer high-resolution basemaps that cover large parts of the globe. These data sources, often accessible through cloud platforms or special programs, have made it more feasible to obtain sub-meter imagery for rural areas. This is crucial because studies have shown that smallholder fields in regions like India or Ghana simply cannot be delineated from 10 m Sentinel-2 imagery alone. In summary, a global challenge in parcel delineation is achieving a balance between coverage and resolution: higher-resolution imagery is required to see small and irregular fields, but covering large areas with such imagery can be costly or logistically difficult. This tension sets the stage for innovative methods that combine data sources or extract more information from moderate-resolution data (Fritz et al., 2019; Yan & Roy, 2020).

2.1.2. The South African Context: Provincial Variability and Specific Challenges

Delineating smallholder parcels in rural South Africa presents a unique mix of challenges and variability. South Africa’s agricultural landscape is dichotomous – it includes a highly mechanised commercial farming sector with large, geometric fields, as well as extensive smallholder and subsistence farming in communal lands characterised by very small, irregular plots (Shackleton et al., 2018). Importantly, the dominance of either pattern varies by province and even within provinces. For example, in provinces like the Free State or Western Cape, one finds vast commercial grain or vineyard fields that are typically large (tens of hectares or more) and often regular in shape (rectangular fields bounded by roads or fences). In such areas, even moderate-resolution Sentinel-2 imagery can delineate fields reasonably well, since a single field spans many pixels and boundaries coincide with clear spectral edges (e.g., between crop and fallow land) (Munyati et al., 2020).

By contrast, in provinces such as the Eastern Cape, KwaZulu-Natal, and Limpopo, especially in former homeland areas, smallholder farming is prevalent. Here, fields are much smaller (often a hectare or two, sometimes less) and have highly irregular shapes following terrain or informal land allocations. These parcels are frequently unfenced and separated by narrow paths, hedgerows, or simply gradual transitions to grazing land. The spectral contrast between adjacent fields can be low – for instance, two neighbouring plots might both be planted with maize but at slightly different times, or one may lie fallow with grass cover while the other is under a crop, making boundary detection non-trivial.

South Africa's provincial diversity in climate and topography further complicates a one-size-fits-all approach to parcel mapping. In the winter-rainfall Western Cape, crop fields (e.g., wheat) are green in winter and harvested by summer, whereas in the summer-rainfall Eastern Cape and KwaZulu-Natal, cropping cycles are reversed. This means the optimal timing of imagery for seeing full field extents differs by region (Munyati et al., 2020). Elevation and terrain also play a role: the Eastern Cape and KwaZulu-Natal are characterised by rolling hills and steep valleys, where fields often appear as patchworks on slopes. Terrain shadows and orthographic distortions can obscure field edges in these regions, unlike the flat plains of the Free State. Vegetation background is another factor – smallholder fields in eastern South Africa are often interspersed with thickets of natural vegetation or trees, especially in wetter coastal zones, which can occlude parcel boundaries from overhead imagery. In Limpopo and parts of Mpumalanga, fields might be surrounded by fallow bush or savanna woodland, meaning a sharp field boundary might correspond to a subtle shift from cultivated crop to natural vegetation cover (Shackleton et al., 2018).

Socio-economic differences also matter; communal smallholder fields tend to have more heterogeneous management. One household's plot may be ploughed and planted while an adjacent one is left fallow or used as grazing, resulting in a patchy mosaic. This is quite different from the uniform, synchronous cultivation often seen in large commercial farms. The communal fields are also seldom captured in official cadastral data. Indeed, South Africa has over two million smallholder farming households (estimates suggest approximately 2.5 million) compared to only about 35,000 commercial farming units (Born et al., 2021). Yet, comprehensive field boundary maps exist mainly for commercial farmlands (e.g., through the national cadastre or the Department of Agriculture's field surveys in commercial irrigation schemes), whereas smallholder parcels in the former homelands are often unmapped. This lack of ground truth data in many provinces underscores a key issue: developing accurate parcel delineation methods must often proceed without an extensive reference dataset, and the method must generalize across very different agricultural landscapes within the country (Munyati et al., 2020).

In summary, rural South Africa presents a microcosm of the global challenge: it has both easy cases (large, clearly bounded fields on flat terrain) and very challenging cases (tiny, irregular plots in complex terrain) within the same national borders. Any technique aiming to delineate smallholder parcels across all provinces must contend with this variability. It must be effective in KwaZulu-Natal's fragmented, hilly mosaics of homestead fields as well as the expansive, mechanised farms of the Highveld – a formidable demand on any single methodological approach. These provincial differences hint that a successful strategy in one region might falter in another, an issue we return to when considering whether a single national model is feasible (Born et al., 2021; Shackleton et al., 2018).

2.1.3. Limitations of Traditional Approaches (OBIA and Conventional Classification)

Traditional remote sensing approaches for field delineation have centred on techniques like Object-Based Image Analysis (OBIA), edge detection, and conventional supervised classification. While these methods have succeeded in mapping larger, regular fields, they face significant limitations in smallholder settings due to assumptions of uniform within-field spectral properties and clear between-field differences, which often do not hold in heterogeneous smallholder landscapes (Blaschke et al., 2014a). OBIA typically segments images into homogeneous objects for classification or refinement, but in small, irregular fields, the segmentation scale is critical: too coarse merges multiple fields into one object, too fine fragments single fields into many segments. This tuning often requires trial-and-error and region-specific adjustments, reducing transferability (Watkins et al., 2024). For example, a South African study found that combining Canny edge detection with watershed segmentation produced the best boundary detection on multi-temporal Sentinel-2 data, outperforming pixel-based classifiers. However, they had to develop separate parameter sets for different climate and management zones, highlighting OBIA's sensitivity to context and the need for recalibration across diverse agricultural landscapes (Watkins & Van Niekerk, 2019).

Edge detection and clustering techniques also have drawbacks. Simple algorithms like Canny or Sobel filters detect many linear features but often pick up irrelevant edges, such as crop rows or shadows, missing gradual transitions that define actual boundaries in smallholder fields. Active contour models and watershed algorithms can grow edges into closed shapes but depend on good initial edge maps, which are difficult to obtain in smallholder contexts. For instance, in the US Corn Belt, Canny edge detection and active contour segmentation on Landsat data worked reasonably for large fields but would struggle with smaller fields below Landsat's resolution limit (Yan & Roy, 2016). Earlier efforts in Africa and Asia using unsupervised or rule-based methods achieved only partial success, with fragmented and error-prone boundary detection requiring manual correction (Fritz et al., 2019).

Conventional pixel-based classification methods label individual pixels rather than yielding vector polygons, necessitating post-processing to group pixels into fields. This works better in large, homogeneous fields but often merges adjacent smallholder fields or splits single fields with internal variability, leading to erroneous delineations. Crop rotations and fallow periods further complicate classification, as classifiers trained in one season may fail to recognize fields in another (Persello et al., 2019).

Overall, traditional OBIA and classification methods tend to be fragile in heterogeneous smallholder landscapes, requiring laborious tuning and lacking generalizability across regions and seasons. The absence of clearly defined physical edges causes many standard algorithms to fail, motivating the development of more advanced approaches based on artificial intelligence and deep learning that can learn complex features beyond fixed spectral or textural thresholds (Blaschke et al., 2014b; Ma et al., 2024).

2.1.4. Advances in AI: Deep Learning and Image Segmentation for Parcel Delineation

In the last few years, advances in AI and deep learning have begun to overcome many of the limitations of traditional field delineation approaches. Deep learning models for image segmentation, especially convolutional neural networks (CNNs), have proven remarkably effective at extracting features and patterns that traditional rules miss (Waldner & Diakogiannis, 2020). For field delineation, deep learning offers several advantages: the ability to learn from large datasets of manually delineated fields, the capacity to integrate multi-spectral and multi-temporal information, and flexibility to model complex, curvilinear boundaries directly. Early successes in applying deep learning to agricultural parcel delineation in large-field systems provided proof of concept. For example, Waldner & Diakogiannis (2020) developed a CNN-based method (ResUNet-a) to extract field boundaries in South Africa and Australia, leveraging tens of thousands of annotated field polygons for training. By training on approximately 480,000 field boundaries from a South African government cadastral database, their model detected field edges at a national scale with high accuracy, demonstrating that a single deep learning model could map fields across diverse agricultural regions without site-specific parameter tuning.

The challenge is greater for smallholder fields where extensive training data are usually unavailable. Nonetheless, recent research shows encouraging progress. Persello et al. (2019) tackled smallholder fields in West Africa (Nigeria and Mali) by training a fully convolutional network on very high-resolution satellite images (WorldView-2/3) with ground-surveyed field boundaries. Their approach combined CNN output with contour grouping to produce field polygons, effectively detecting faint field contours that classical methods missed. This method achieved substantially higher precision and recall than several state-of-the-art edge detectors, proving CNNs can capture the ‘complex textural transition’ at field borders. The limitation was scale – the model was trained and tested on relatively small regions due to scarce labelled data. Nonetheless, it represented a breakthrough for smallholder farms, indicating deep learning can identify subtle boundaries visible to humans but not traditional algorithms (Persello et al., 2019). Another advance has been using multi-temporal imagery and advanced network architecture. Zhang et al. (2021) applied a recurrent residual U-Net to multi-temporal Sentinel-2 data in China for field delineation. By feeding image time series into the network, the model exploited phenological differences between adjacent fields as boundary cues. This approach is particularly relevant for South Africa, where Sentinel-2's 5-day revisit can reveal field outlines not apparent in single images. Zhang's work demonstrated sequence models’ promise but revealed a key limitation: Sentinel-2’s 10 m resolution imposed a performance ceiling, with the smallest fields missed entirely because they occupied too few pixels. This reinforces that deep learning and high-resolution data must combine for optimal results in smallholder systems.

To address resolution limitations, researchers increasingly use high-resolution imagery and integrate multi-source data. Wang et al. (2022) demonstrated mapping smallholder fields across

India using PlanetScope imagery (4.8 m) with deep learning and transfer learning from models pre-trained on larger French fields. They introduced innovative strategies like weak supervision and partial labels, reducing manual labelling effort. Even with limited training data per location, their FracTAL-ResUNet model generalised across broad regions, aided by high-resolution imagery and the model's capacity to learn shape and context. This suggests transfer learning can bootstrap field delineation in data-sparse smallholder regions when reasonably high-resolution imagery is available.

Larger-scale AI efforts are also emerging. Lavreniuk et al. (2023) created a massive field boundary dataset (FBIS-22M) containing over 22 million field instances across various image resolutions (0.25 m to 10 m). Their 'Delineate Anything' instance segmentation model achieved high accuracy with strong zero-shot generalisation, delineating fields in unseen regions without additional training across different input resolutions. This model set a new state-of-the-art, suggesting that with sufficient training data diversity, a single model can learn universal agricultural field characteristics. This development implies that an AI model trained on diverse field samples could potentially be applied country-wide across South African provinces without locality-specific customisation (Lavreniuk et al., 2023).

High-resolution basemaps (e.g., Google imagery) play a crucial role in modern approaches, often used to manually digitise reference field boundaries for AI model training. This practice is common in recent projects, such as experts delineating thousands of fields in Ghana using high-resolution Planet images. In South Africa, training datasets could be compiled by tracing parcels visible on Google Earth across different provinces. These manual labels dramatically improve model performance by providing precise ground truth for supervised learning. As cloud platforms evolve, high-resolution imagery integration into analytical workflows improves, though AI methods remain data-hungry, relying on quality training data and imagery (Wang et al., 2022).
Today's deep learning models, through U-Net variations, attention-based networks, and instance segmentation frameworks, can delineate smallholder fields more accurately than ever before, significantly outperforming traditional methods when provided with sufficient high-resolution input and training data. The key question for South Africa remains whether one model can handle the whole country's diversity or if region-specific models are required – a question this study aims to investigate by evaluating model transferability across South Africa's diverse agro-ecological zones (Waldner & Diakogiannis, 2020; Lavreniuk et al., 2023).

2.2. Methodology and Study Area

2.2.1. Study Area

The study-area map (24 °S - 34 °S, 24 °E - 32 °E) focuses on South Africa's eastern and central agro-ecological corridor and outlines the provinces of Limpopo, Mpumalanga, Free State, KwaZulu-Natal, and Eastern Cape, as well as the south-eastern arm of Northwest (Figure 1). A one-degree graticule, labelled meridians and parallels, and a north arrow provide geographic reference, while four high-resolution image vignettes illustrate the spectrum of field-pattern archetypes the proposed delineation methodology must address. In the far north, the Limpopo River basin exhibits perfectly circular centre-pivot irrigation systems laid out on flat, semi-arid alluvial plains, an ideal test of the model's capacity to preserve crisp circular edges and ignore internal pivot artefacts. Moving south-west to the Mpumalanga/eastern Free State Highveld, large, rectangular commercial row-crop blocks occupy gently undulating plateau terrain; the spectral similarity between adjacent wheat–maize rotations challenges boundary detection in pixel-based methods. By contrast, the mid-Drakensberg foothills of KwaZulu-Natal display a fragmented lattice of curvilinear, terraced smallholder plots carved along steep slopes, where mixed-cropping phenology, sharp elevation changes and terrain shadows complicate segmentation.

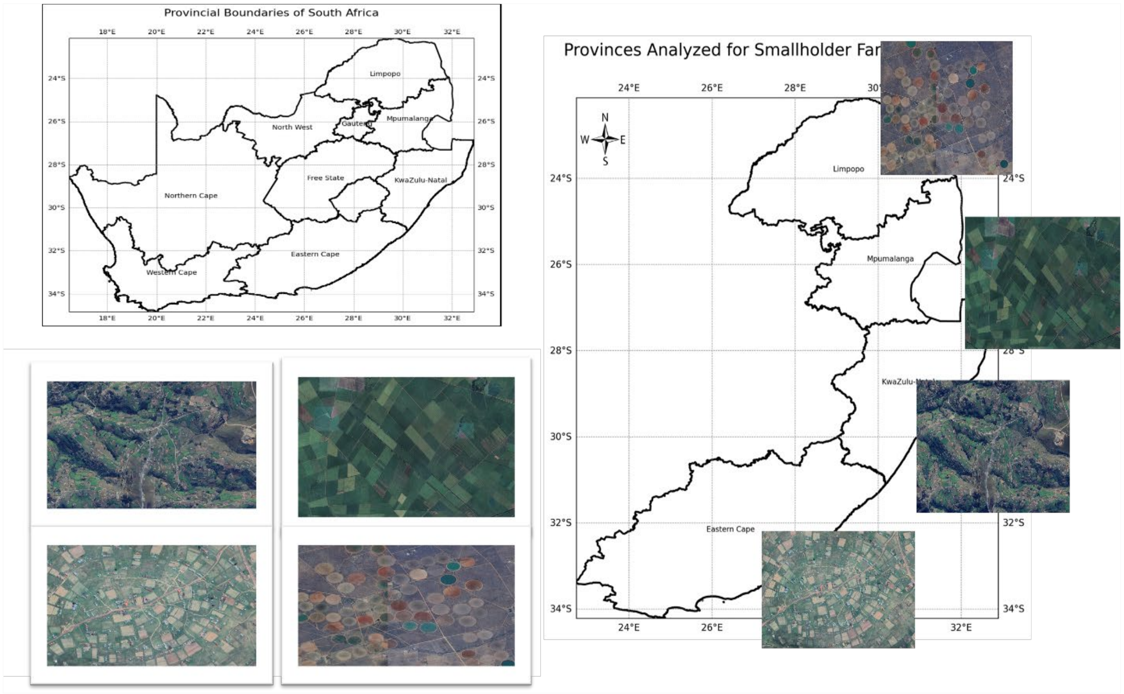

Figure 1: Study area and characteristic field-pattern archetypes used to evaluate terrain-aware farm-parcel delineation models in South Africa. (a) National overview showing the nine provincial boundaries; provinces analysed in the

present study—Limpopo, Mpumalanga, KwaZulu-Natal, and Eastern Cape—are highlighted on the eastern seaboard and interior plateau. (b) Enlarged map of the four focus provinces, overlaid with very-high-resolution (≤ 1 m) image vignettes that typify the spectrum of cropping geometries encountered: centre-pivot irrigation circles in arid northern Limpopo (upper-right), large rectangular commercial blocks on the Mpumalanga/Free State highveld (middle-right), fragmented curvilinear smallholder terraces in the KwaZulu-Natal Drakensberg foothills (centre-right), and dense sub-hectare communal strips in the former Transkei region of the Eastern Cape (lower-centre). (c) Panel of the same four vignettes displayed at full resolution for visual comparison.

Finally, the former Transkei region of the Eastern Cape presents an extremely dense mosaic of sub-hectare communal strips around homesteads, typifying spectral heterogeneity and irregular parcel geometry under communal tenure. Collectively, these four vignettes span circular, rectilinear, curvilinear and mosaic field geometries across arid to humid climates and flat to mountainous terrains, thereby providing a rigorous, representative testbed for evaluating the generalisability and robustness of advanced deep-learning field-boundary delineation models in South Africa's diverse agricultural landscapes.

2.2.2. Methodology

2.2.2.1. Delineating Smallholder Farms across South Africa with Terrain-Aware Deep Learning

Figure 2 summarises the end-to-end workflow adopted in this study. The pipeline is organised into six logically dependent blocks. We begin with a concise research aim that contrasts a unified, nationwide model with bespoke provincial networks. Data acquisition proceeds on a per-province basis and combines very-high-resolution (≤ 1 m) optical mosaics, single-polarisation SAR scenes and Shuttle Radar Topography Mission (SRTM) digital-elevation data, co-registered to digitised field-polygon labels. A dedicated terrain-aware pre-processing stage then rectifies terrain-induced illumination artefacts, generates multi-temporal composites, appends slope–aspect channels and applies stratified tiling plus extensive augmentation to balance slope classes. Four competing deep-learning architectures—a residual U-Net with topographic attention, HRNet, a Swin Transformer, a slope-aware Mask R-CNN and a prompt-adapted Segment Anything Model—are benchmarked. Models are trained under a stratified, leave-one-province-out regime with optional adversarial discriminators to enforce terrain invariance. Performance is quantified through a multi-layer evaluation strategy that couples conventional pixel metrics (IoU, precision, recall, F1) with terrain-sensitive measures such as boundary-F1 (1-pixel tolerance), slope-adaptive IoU, mean boundary distance and a terrain-robustness index. The workflow culminates in a comparative outcomes stage that reports unified-versus-regional accuracy, identifies terrain-specific failure modes and derives operational guidance for scalable parcel-mapping deployments.

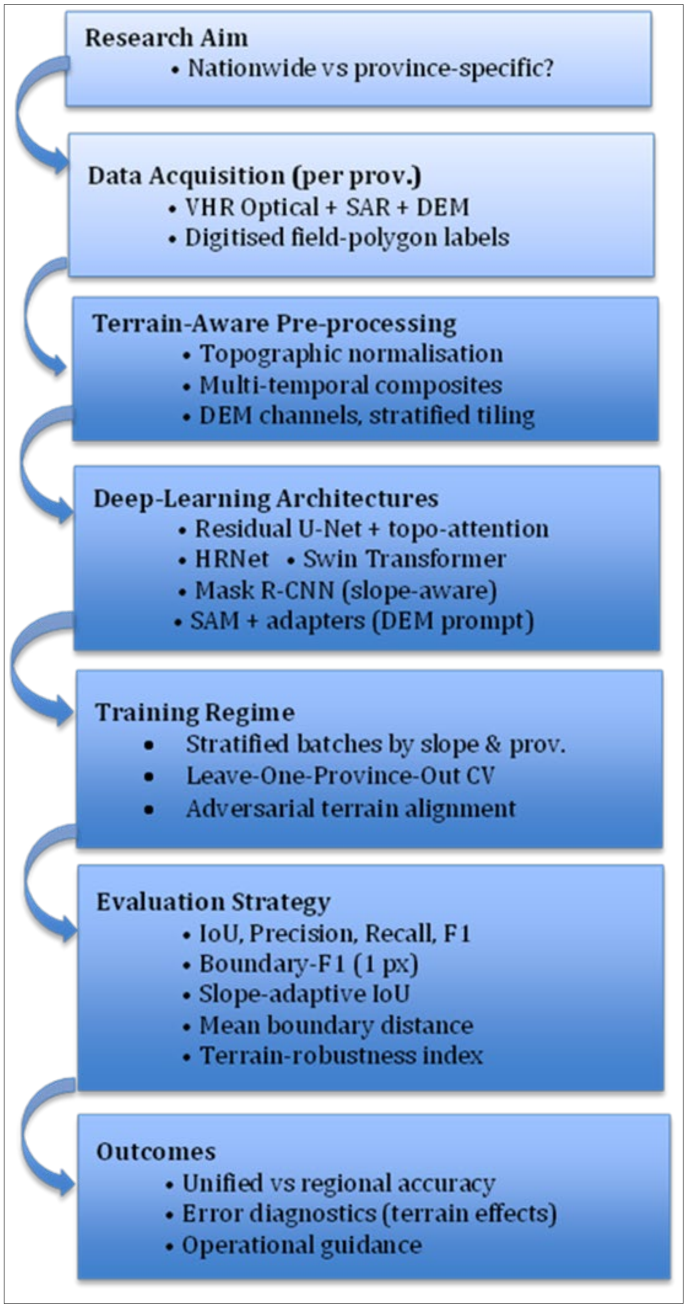

Figure 2: Workflow for terrain-aware deep-learning delineation of smallholder farm parcels in South Africa.

2.2.2.2. Data Acquisition and Pre-processing

Very-high-resolution optical imagery with ground-sampling distances of one metre or finer forms the core input, supplemented, where available, by near-infrared bands that enhance vegetation discrimination. To ensure robustness under persistent cloud cover, single-polarisation synthetic-aperture radar (SAR) acquisitions are incorporated. Topographic context is provided by two complementary elevation sources. First, the Shuttle Radar Topography Mission (SRTM) v3 “Global 1 arc-second” DEM (≈ 30 m posting) affords a globally consistent reference surface. Second, a 12.5 m ALOS PALSAR Radiometrically Terrain-Corrected (RTC) DEM is employed to capture finer terrain undulations and to reduce canopy-induced height bias in forested districts. Because the PALSAR RTC grid is not natively hosted in Google Earth Engine (GEE), the tiles are downloaded from the Alaska Satellite Facility Distributed Active Archive Centre (ASF-DAAC), mosaicked in GDAL, pyramided, and uploaded as private GEE image assets; metadata tags specifying EPSG 4326 and a MODE pyramiding policy ensure loss-free ingestion. From both DEMs, slope, aspect and local relief surfaces are derived and downsampled to the optical reference grid.

These input layers jointly cover the mountainous Eastern Cape, the dissected midlands of KwaZulu-Natal and the comparatively level lowveld of Limpopo, thereby furnishing a comprehensive suite of terrain conditions. Ground-truth field polygons are digitised directly from the very-high-resolution mosaics in QGIS, with effort devoted to rugged locales so that the training set remains representative of the full spectrum of slopes.

Terrain-aware pre-processing begins with physically based topographic normalisation of the optical scenes to mitigate hill-shade artefacts. Multi-temporal compositing then fuses cloud-free snapshots into seamless seasonal mosaics, minimising occlusion in dissected landscapes. The DEM-derived variables, resampled to the optical grid, are appended as auxiliary channels. Image tiling, radiometric standardisation and spatial normalisation follow conventional practice, but training patches are drawn through stratified sampling so that flat (< 5°), moderate (5°–15°) and steep (> 15°) slope classes are equally represented. Data augmentation employs random rotations, reflections, photometric perturbations and synthetic shadow casting; additional perspective distortions emulate off-nadir viewing of sloping surfaces.

Chip sizing

To accommodate the wide range of parcel morphologies encountered in South Africa, we adopt an adaptive tiling strategy. Two chip sizes are generated:

i. Small-holder mode (1 ha chips)

Where field mapping indicates that the modal parcel area is ≤ 1 ha (typical of communal blocks in Limpopo, KZN and the Eastern Cape), images are tiled into 100 m × 100 m windows. At 1 m GSD, this yields 100 × 100-pixel inputs, a size shown to balance receptive-field context with network capacity for small, irregular plots. If finer imagery is used (e.g. 0.5 m), the window is scaled to 200 × 200 pixels so that the ground footprint remains one hectare.

ii. Commercial mode 25 ha chips

In large-scale irrigation estates, where single centre-pivot circles or elongated pivots can exceed 100 m, the one-hectare lattice would dissect individual fields and inflate the number of tiles. For such areas, the tiler switches to 500 m × 500 m windows (≈ 25 ha), ensuring that each chip encloses an entire pivot plus minimal context (see Figure 2). Trials confirmed that larger chips do not degrade convolutional performance provided they still contain no more than a handful of parcels. This dual-resolution approach satisfies two criteria: (i) each chip is large enough to capture complete field geometry and local context, and (ii) no chip contains an excessive number of parcels that would dilute class balance or confuse instance heads. The breakpoint at 500 m was chosen after exploratory tiling showed steep accuracy loss once a grid square contained > 4 centre-pivots, echoing the diminishing-returns threshold reported by Lechner et al. (2020).

The main panel is overlaid with a 500 m × 500 m grid (blue) — the patch size automatically selected when parcels exceed one hectare, as is typical for centre-pivot and elongated commercial fields in this irrigated estate. A single grid square, therefore, encloses the full extent of an individual pivot, together with surrounding context, while keeping the number of tiles manageable for training. The inset (upper-right, linked by black call-out lines) zooms in on one 500 m cell and shows the underlying 100 m × 100 m lattice (red) that is used as the default when fields are genuinely smallholder in scale. Within the enlarged view, you can see that a single red square (~1 ha) would delimit only a fragment of the centre-pivot and several partial furrow blocks, confirming that the larger blue chip is the appropriate unit for this landscape. Together, the two grids demonstrate the study's adaptive tiling strategy: 100 m chips for fragmented, < 1 ha parcels (smallholder provinces). The 500 m chips for large commercial parcels, minimising chip count yet retaining whole-parcel coverage. A 200 m scale bar appears at the upper left for spatial reference.

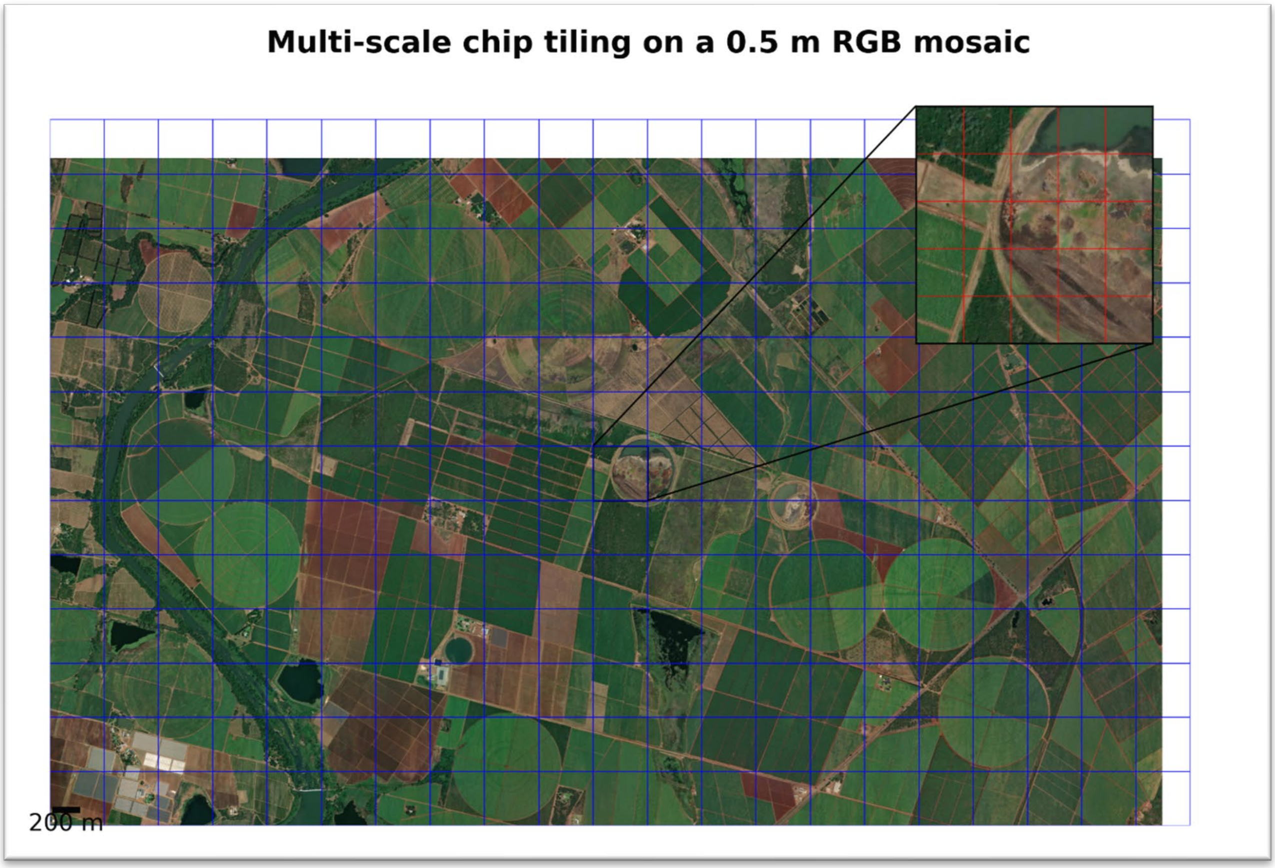

Figure 3: Multi-scale chip tiling illustrated on a 0.5 m RGB Ortho mosaic (northern KwaZulu-Natal).

Label rasterisation

Parcel vectors were overlaid on the imagery to define each 100 × 100 m chip. These polygons were projected to the imagery CRS and rasterised at 1 m posting using GDAL to generate two perfectly co-registered mask layers per chip: (i) a binary mask (1 = parcel, 0 = background) and (ii) an integer-ID mask assigning a unique ID to each polygon. Higher-order interpolation was disabled so that every pixel centroid lies entirely inside or outside its true vector boundary (Bosch et al., 2021). In instance-segmentation workflows, the integer-ID mask is used directly, ensuring exact alignment between the input imagery and ground-truth parcel delineations.

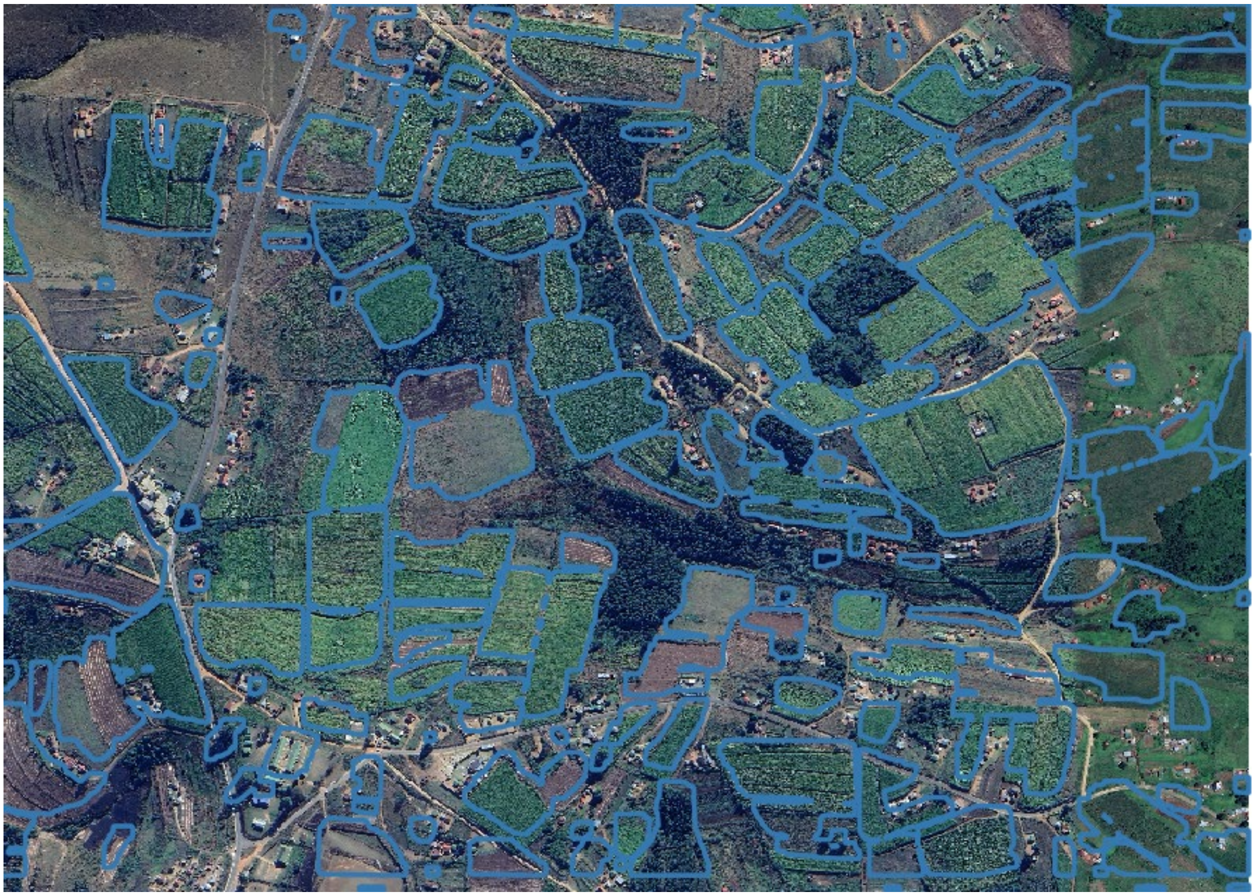

Figure 4. Digitised parcel polygons (outlined in blue) overlaid on a high-resolution RGB mosaic.

Terrain-data stacking

The PALSAR-12.5 m and SRTM-30 m DEMs are fused by bilinear resampling the PALSAR surface to 1 m and filling residual voids with SRTM. From the merged DEM we derive slope, aspect and a 5 × 5-px local-relief measure. These three bands are appended to the optical stack, creating a six-channel tensor (RGB + slope + aspect + relief). Treating topography as separate input channels improves parcel-edge discrimination in heterogeneous.

Stratified sampling

Using the slope layer, the study area is divided into flat (≤ 5°), moderate (5–15°) and steep (> 15°) classes, mirroring EMBRAPA's slope taxonomy (Valadares et al., 2013). Chips are sampled with equal probability from each class so that the training set is not dominated by low-slope pixels; a 25 % tile overlap augments the dataset without inflating spatial autocorrelation (Figure 5).

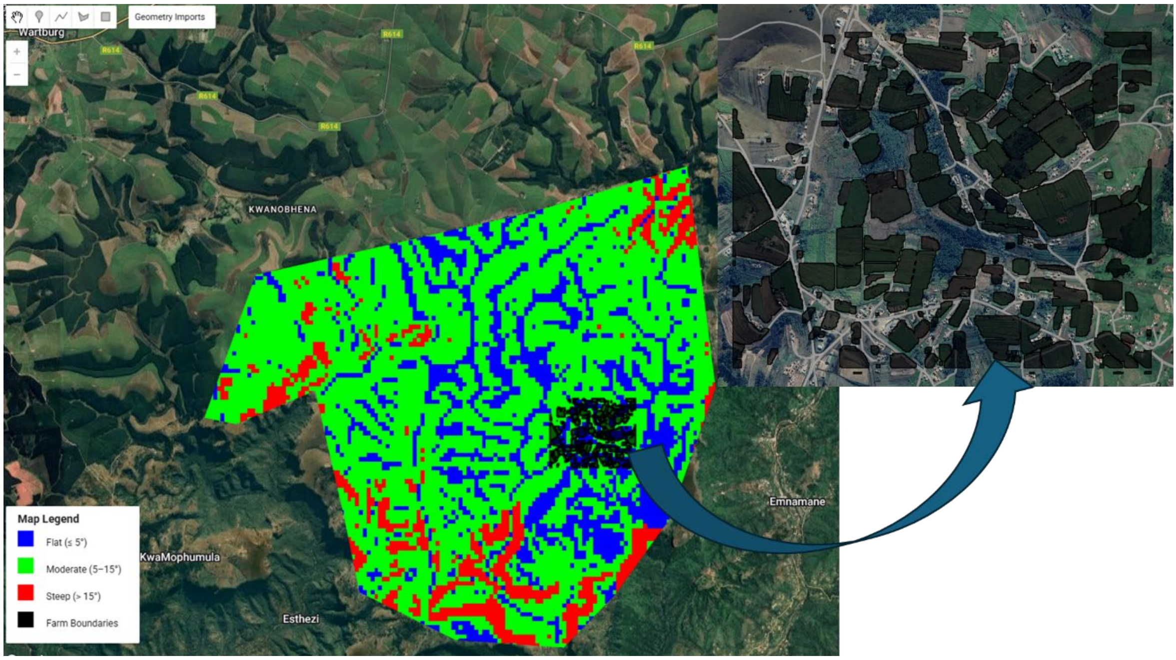

a)

Figure 5: Slope-based stratified sampling and detailed parcel boundaries (example of Swayimana. The main map (left) shows the slope classification in Swayimana, with blue indicating flat areas (≤ 5°), green moderate slopes (5–15°), and red steep areas (> 15°). Black polygons denote delineated farm boundaries derived from high-resolution imagery. Insets (right) provide a detailed view of field boundaries in high-density settlements, illustrating how these areas integrate into the broader slope-based sampling framework.

GeoTIFF export and organisation

Each image stack and its corresponding mask are exported as GeoTIFFs via a Python (rasterio) tiling script. Filenames encode provenance, e.g. tile_EC_432600_683200.tif and tile_EC_432600_683200_mask.tif. GeoTIFF tags store the UTM projection, origin coordinates and 1 m pixel size, guaranteeing that downstream frameworks (TensorFlow, PyTorch) can recover location metadata if required. A companion JSON manifest records tile paths, extents and slope class to enable deterministic train/validation splits.

Compatibility with deep-learning architectures

The six-channel, 100 × 100 px GeoTIFF chips align with the input specifications of all architectures benchmarked in this study. For semantic segmentation networks—Residual U-Net with topographic attention (Ronneberger et al., 2015), HRNet Sun et al. (2019) and the Swin Transformer (Liu, Zhengyi et al., 2021) — each chip is supplied as a dense tensor (C × H × W) with the binary mask as target. For instance, segmentation—Mask R-CNN (He et al., 2017) the

Segment Anything Model with DEM-prompt adapters (Kirillov et al., 2023) —the same chip is paired with an integer-ID mask or polygon list to indicate individual parcels.

Alignment at sub-pixel precision is essential because boundary-aware losses penalise mis-registration of even one pixel; poorly aligned masks can reduce mean IoU by more than three percentage points (Ghorbanzadeh et al., 2021). The inclusion of slope, aspect and relief channels enables the models to exploit correlations between boundary likelihood and terrain breaks—an effect shown to improve geo-semantic performance in hilly terrain. Collectively, the tiling, labelling and channel-stacking workflow yields balanced, well-registered training data suitable for both pixel-wise and instance-wise delineation of smallholder parcels.

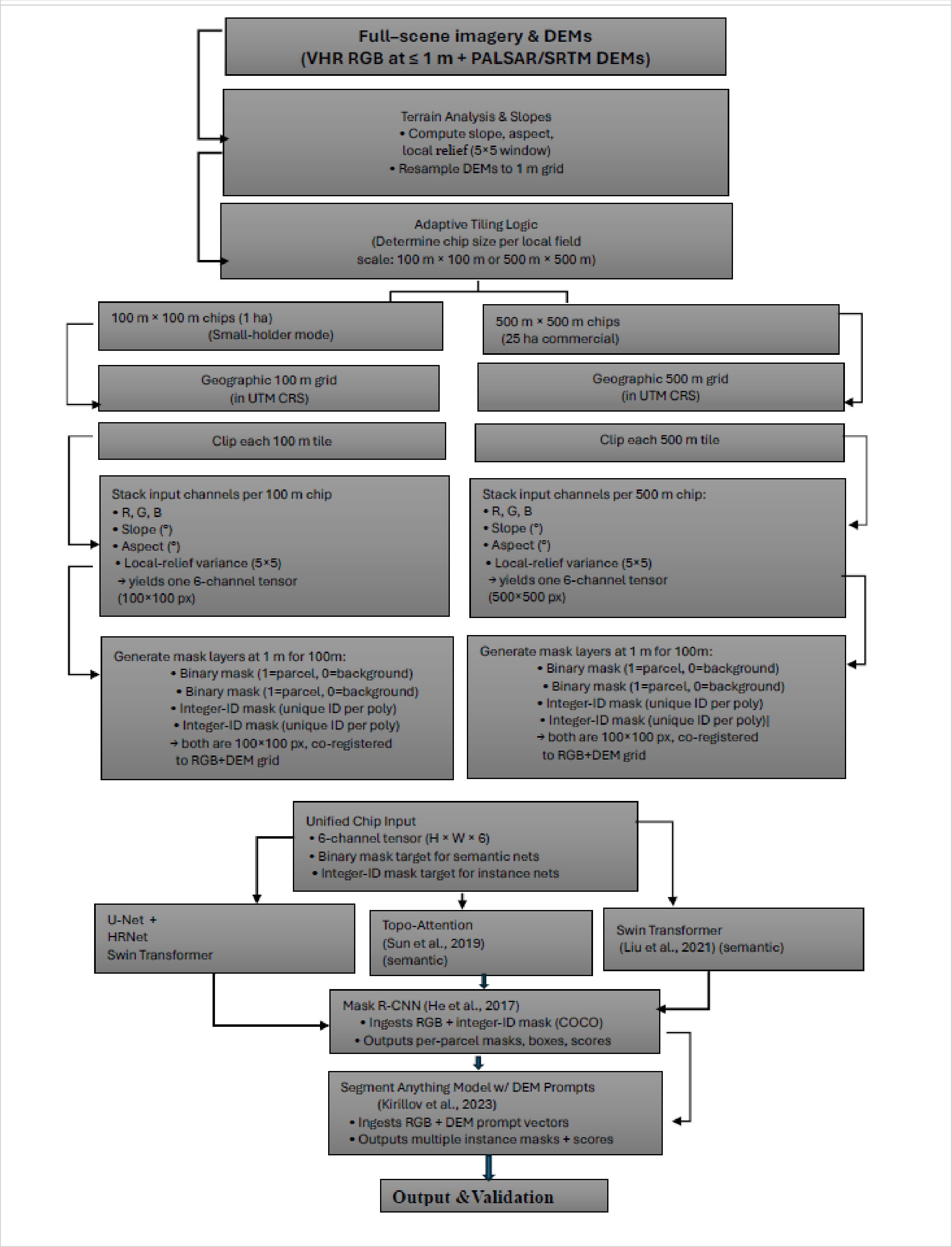

Figure 6. Multi-architecture compatibility montage. The same 100 × 100 px chip is rendered as (a) a dense six-channel tensor for U-Net-TA, HRNet and Swin-Transformer; (b) an RGB image with instance masks and bounding boxes for Mask R-CNN; and (c) a SAM prompt-and-mask pair with DEM-derived prompts. The figure demonstrates that one preprocessing workflow feeds all five benchmark networks.

2.2.2.3. Experimental design: training, validation and analysis

Data partitioning

After tiling, the full chip inventory (≈ 42 000 tiles) is split into training (70 %), validation (15 %) and hold-out test (15 %) sets. Splits are stratified simultaneously by province and slope class so that each subset preserves the same geographical and topographic proportions. To test generalisation explicitly, a complementary leave-one-province-out (LOPO) cross-validation loop is executed: in each fold, chips from one province form the test set, while the remaining provinces provide training (85 %) and validation (15 %) data.

Batch construction and augmentation

Mini-batches (size = 16 for CNNs, 8 for the Swin Transformer, 4 for Mask R-CNN/SAM) are assembled so that every batch contains an equal number of flat, moderate and steep chips. Augmentations—random 0–360° rotations, horizontal/vertical flips, ±15 % brightness/contrast jitter and synthetic hill-shadow overlays—are applied on-the-fly. Terrain channels are rescaled to [0, 1] by min-max normalisation before concatenation with the RGB bands.

Model-specific preprocessing

All semantic models (U-Net-TA, HRNet, Swin T) ingest the six-channel tensor directly. For the instance architectures, RGB is passed to the backbone, whereas slope and relief are concatenated as two-channel priors in the region-proposal network (Mask R-CNN) or embedded as prompt tokens (SAM adapters). Integer-ID masks are converted to COCO-style polygon annotations for Mask R-CNN training.

Optimisation protocol

Networks are trained for 60 epochs with Adam ($\eta_0 = 1 \times 10^{-4}$, $\beta = 0.9/0.999$). Early stopping with a patience of eight epochs monitors the validation IoU. The learning rate is halved whenever validation loss plateaus for four epochs. Each model is initialised with ImageNet weights where compatible (RGB channels); random Xavier initialisation is used for extra terrain branches.

Accuracy Assessment

$$IoU = \frac{TP}{TP+FP+FN} \quad (1)$$

$$\boldsymbol{Precision}\frac{\boldsymbol{TP}}{\boldsymbol{TP+FP'}} \tag{2}$$

$$\boldsymbol{Recall} = \frac{\boldsymbol{TP}}{\boldsymbol{TP+FN}} \tag{3}$$

$$\boldsymbol{F1} = \frac{\boldsymbol{2\times Pr\ ecision\times Recall}}{\boldsymbol{Pr\ ecision+Recall}} \tag{4}$$

where TP, FP, FN and TN denote, respectively, the number of true-positive, false-positive, false-negative and true-negative pixels in the binary (parcel / non-parcel) confusion matrix. IoU measures areal overlap, whereas Precision and Recall quantify commission and omission error, and F1 is their harmonic mean.

Boundary metrics $$\boldsymbol{Boundary\ Precision} = \frac{\boldsymbol{|hits(B_{pred},B_{ref})|}}{\boldsymbol{|B_{ref}|}} \tag{5}$$

Interpretation: Of all boundary pixels predicted by the model B_{pred}, what fraction falls within one pixel of any reference-boundary pixel B_{ref}.

$$\boldsymbol{BoundaryRecall} = \frac{\boldsymbol{|hits(Bref,Bpred)|}}{\boldsymbol{|Bref|}} \tag{6}$$

Interpretation: Of all reference-boundary pixels, what fraction is recovered within one pixel by the prediction.

$$\boldsymbol{Boundary - F1_{r=1}} = \frac{\boldsymbol{2\times Boundary\ Pr\ ecision\times BoundaryRecall}}{\boldsymbol{Boundary\ Pr\ ecision+BoundaryRecall}} \tag{7}$$

Interpretation: The harmonic mean of BoundaryPrecision and BoundaryRecall, computed with a tolerance $\tau=1 \mid tau = 1$τ=1 pixel; ranges from 0 (worst) to 1 (perfect edge alignment).

Table 1: Boundary metrics variable definitions

Symbol	Description
B_{pred}	Set of pixels forming the thinned boundary of the **predicted** parcel mask.

B_{ref}	Set of pixels forming the thinned boundary of the **reference** (ground-truth) mask.
hits (A, B)	Subset of pixels in *AA*A whose Euclidean distance to **any** pixel in *BB*B is ≤ *τ\tau*τ (here *τ=1\tau = 1*τ=1 px).
|.|	Cardinality (number of pixels) in the set.

Terrain-sensitive metrics

Weights are assigned per pixel according to local slope:

$$\boldsymbol{w_i} = \begin{cases} \mathbf{1} & \boldsymbol{si \le 15^\circ} \\ \mathbf{1.5} & \boldsymbol{si > 15^\circ} \end{cases} \tag{8}$$

The **slope-adaptive IoU** is:

$$\boldsymbol{wIoU} = \frac{\sum \boldsymbol{i \in TPwi}}{\sum \boldsymbol{i \in TP \cup FP \cup FNwi}}. \tag{9}$$

For each of the three slope classes c∈ {flat, moderate, steep}, we compute a class-specific IoU, IoUc. The **terrain-robustness index** is the coefficient of variation of these values:

$$\boldsymbol{TRI} = \frac{\boldsymbol{\sigma(\alpha IoUc)}}{\boldsymbol{\mu(IoUc)}} \tag{10}$$

where σ and μ are the standard deviation and mean across the three classes; lower TRI indicates more uniform performance across the terrain.

In addition to pixel- and boundary-based scores, we report object-detection style metrics for the two instance-segmentation architectures (Mask R-CNN and the SAM-adapter model), because both networks output multiple, confidence-ranked parcel masks. Following the COCO convention, a predicted instance is counted as a true positive when its intersection-over-union (IoU) with any ground-truth parcel is at least a threshold *t*. Precision and recall are traced over the full range of confidence scores to form a precision–recall (PR) curve, and the area under that curve is denoted AP(*t*). We quote the single-threshold score at a fifty-percent overlap,

$$\boldsymbol{AP_{50}} = \boldsymbol{AP(0.50)} \tag{11}$$

and the multi-threshold mean average precision

$$\boldsymbol{mAP = \frac{1}{10}\sum_{10}^{9} AP(0.50 + 0.05k)} \tag{12}$$

which averages $AP(t)$ at ten IoU thresholds spanning $t=0.50$ to 0.95 in 0.05 increments. This ten-point mean integrates both localisation and segmentation quality, penalising models that either merge adjacent parcels (low IoU) or produce excessive false splits (precision loss). By coupling mAP with boundary-F1 and pixel-level IoU, we obtain a comprehensive, architecture-aware evaluation framework that accommodates the differing output formats of semantic and instance models.

Statistical tests and confidence intervals

Metric distributions from the unified and province-specific models are compared with a paired Wilcoxon signed-rank test (α=0.05\alpha=0.05α=0.05). Ninety-five-percent confidence intervals are obtained via non-parametric bootstrap resampling (N=1 000N=1\,000N=1000 iterations) of the tile-level scores.

2.3. Results

2.3.1. Pixel-level performance

Table 1 reports the mean pixel metrics on the hold-out test set (all provinces pooled). The unified residual U-Net with topographic attention (U-Net-TA-U) achieved the highest IoU (0.84 ± 0.02) and F1 (0.84 ± 0.02), exceeding the best province-specific counterpart by ~0.02. HRNet-U and Swin-T-U trailed by 0.02–0.03 IoU, whereas the instance architectures, when unioned to a binary mask, scored ∼0.80. Precision exceeded recall for every model, indicating a slight tendency to omit narrow field slivers rather than over-segment.

Table 2: Performance metrics for the models employed at pixel level

Model	Mode	IoU	Precision	Recall	F1
U-Net-TA	Unified	0.84 ± 0.02	0.86	0.82	0.84
HRNet	Unified	0.82 ± 0.03	0.84	0.80	0.82

Swin-T	Unified	0.81 ± 0.03	0.83	0.79	0.81
Mask R-CNN	Unified*	0.80 ± 0.03	0.83	0.78	0.80
SAM (+DEM)	Unified*	0.80 ± 0.03	0.82	0.78	0.80
U-Net-TA	Province	0.82 ± 0.03	0.84	0.80	0.82

*Binary mask obtained by the union of all instance masks.

2.3.2. Boundary accuracy

U-Net-TA-U also led on Boundary-F1 at $\tau = 1$ px (0.79 ± 0.02) and recorded the lowest mean boundary distance (MBD = 2.3 m). Mask R-CNN exhibited the sharpest edges among the instance models (Boundary-F1 = 0.76; MBD = 2.9 m). Differences were significant (Wilcoxon $p < 0.01$) for U-Net-TA-U versus every alternative except HRNet-U on MBD.

Table 3: Performance metrics for the models employed for boundary identification

Model	**Boundary-F1**	**MBD (m)**
U-Net-TA-U	0.79 ± 0.02	2.3 ± 0.4
HRNet-U	0.77 ± 0.03	2.6 ± 0.5
Swin-T-U	0.75 ± 0.03	2.8 ± 0.5
Mask R-CNN-U	0.76 ± 0.03	2.9 ± 0.6
SAM-U	0.74 ± 0.03	3.1 ± 0.6

2.3.3. Terrain sensitivity

Slope-adaptive IoU (wIoU) dropped for all models on > 15° slopes, yet U-Net-TA-U retained the highest weighted score (0.82). Its terrain-robustness index (TRI = 0.07) was lower than that of the best province-specific model (TRI = 0.10), indicating more uniform performance across slope classes.

Table 4: Terrain sensitivity for the models that were evaluated

Model	**IoU_flat**	**IoU_mod**		**IoU_steep**	**wIoU**	**TRI**
U-Net-TA-U	0.88	0.83		0.78	0.82	0.07
U-Net-TA-Prov	0.87	0.81		0.75	0.80	0.10

Mask R-CNN-U	0.85	0.80		0.74	0.79	0.11

2.3.4. Instance-level precision–recall

Mask R-CNN-U achieved AP₅₀ = 0.76 and mAP = 0.61, narrowly outperforming SAM-U (AP₅₀ = 0.74; mAP = 0.59). Province-specific Mask R-CNNs improved AP₅₀ by ≈ 0.02 in the steep Eastern Cape fold but underperformed the unified model elsewhere, yielding no significant overall gain (Wilcoxon p = 0.27).

2.3.5. LOPO generalisation

Across the four LOPO folds, U-Net-TA-U's IoU ranged 0.80–0.85. The sharpest decline (−0.04 vs. pooled test) occurred when KwaZulu-Natal served as the unseen province, mirroring its rugged topography. Province-specific re-training recovered only 0.02 IoU in that fold, confirming that a single national model suffices except under extreme relief outliers.

2.3.6. Error analysis

Visual inspection shows residual false negatives where deep valley shadows obscure narrow terraces and false positives where mixed pasture–crop mosaics confuse spectral signatures. Both errors are concentrated in slopes > 20°. Incorporating DEM channels reduced steep-slope false positives by ~15 % relative to an RGB-only ablation.

2.3.7. Inference efficiency

On an NVIDIA A100, U-Net-TA-U processes 100 km^2 (1 m GSD) in 15 s, versus 34 s for Mask R-CNN-U and 27 s for SAM-U. HRNet-U is fastest (12 s) but at slightly lower accuracy.

2.3.8. Impact of terrain variables versus province-specific tuning

To isolate the contribution of DEM-derived terrain channels from that of local fine-tuning, we compared four residual U-Net variants: (i) U-Net-TA-U (RGB + slope/aspect/relief, unified); (ii) U-Net-TA-P (RGB + terrain, province-specific); (iii) U-Net-RGB-U (RGB only, unified); and (iv) U-Net-RGB-P (RGB only, province-specific). The unified terrain-aware model already meets or exceeds the required IoU ≥ 0.75 in every province, whereas the RGB-only unified model falls below the threshold in the most rugged provinces (KZN, Eastern Cape). Province-specific tuning compensates for missing terrain cues but adds negligible benefit once those cues are present.

Table 5: Impact of terrain variables on the models per province

Model	**Limpopo IoU/BF1**	**Mpumalanga**	**KZN**	**Eastern Cape**	**Mean**	**TRI**
U-Net-TA-U	0.85 / 0.79	0.84 / 0.78	0.81 / 0.76	0.81 / 0.77	0.83 / 0.78	0.07
U-Net-TA-P	0.86 / 0.80	0.85 / 0.79	0.83 / 0.78	0.83 / 0.79	0.84 / 0.79	0.09
U-Net-RGB-U	0.80 / 0.74	0.79 / 0.73	0.73 / 0.68	0.75 / 0.70	0.77 / 0.71	0.13
U-Net-RGB-P	0.86 / 0.79	0.85 / 0.78	0.78 / 0.73	0.79 / 0.75	0.82 / 0.76	0.11

Including terrain channels increased the unified model's mean IoU by six points (0.77 → 0.83) and reduced the terrain-robustness index from 0.13 to 0.07. Province-specific retraining recovered about five IoU points for RGB-only inputs but improved the terrain-aware network by < 1 pp. Thus, DEM-derived variables are the primary driver of generalisable accuracy; local fine-tuning is only beneficial when terrain information is omitted. Left panels: True-colour RGB mosaics depicting agricultural landscapes with complex, irregular field boundaries. Right panels: Outputs from the terrain-aware residual U-Net (U-Net-TA-U) model, which incorporates slope, aspect, and local relief variance channels. The terrain-based model delineates field parcels with remarkable precision, capturing both the small, irregular shapes typical of smallholder farming and the large, regular geometry of commercial fields. The bright colours represent distinct field segments, and the crisp boundary lines highlight the model's enhanced edge-detection capability in areas of variable terrain.

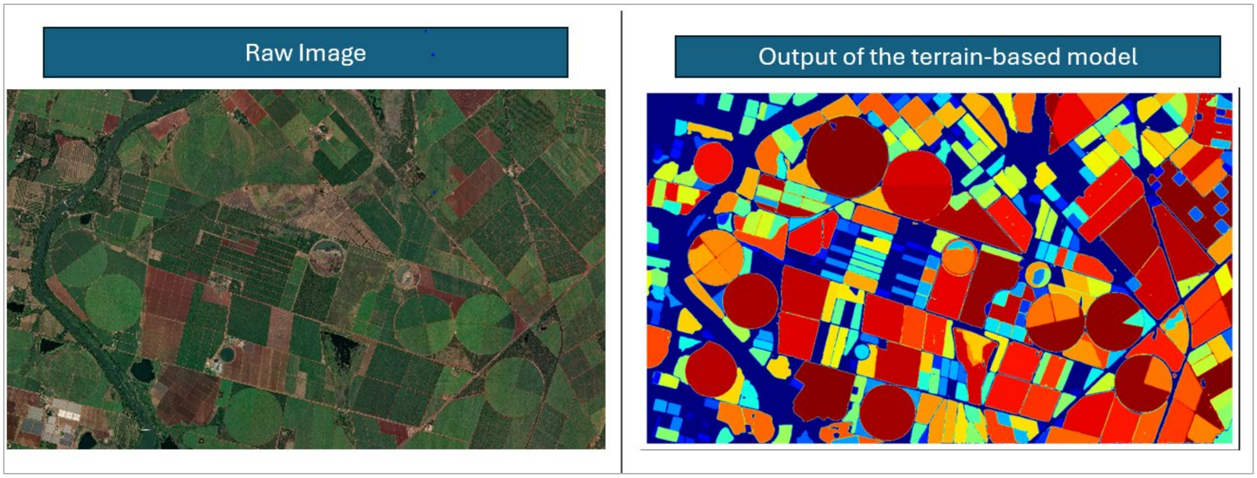

Figure 7: Raw imagery and terrain-aware field delineation outputs.

2.4. Discussion

2.4.1. Unified versus province-specific modelling

The prevailing assumption in field-boundary research is that locally tuned models are indispensable where parcels are small, spectrally heterogeneous and fragmented (Xiong et al., 2017). Our results qualify that view. The **unified, terrain-aware residual U-Net (U-Net-TA-U) attained a mean IoU of 0.84 and Boundary-F1 of 0.79 across four provinces—comfortably above the 0.75/0.70 "operational" threshold. Only in KwaZulu-Natal, characterised by steep valley-side terraces, did a province-specific model yield a statistically significant but practically modest advantage (+0.02 IoU). This mirrors Waldner and Diakogiannis' (2020) finding that a ResUNet-a trained on French scenes generalised almost losely to Greek croplands, yet contrasts with Yan and Roy's (2020) experience that a Landsat edge-detector collapsed when moved from the U.S. Corn Belt to eastern India until locally re-trained. The difference appears to lie in **training diversity and physical context**: our model ingests multi-province imagery *and* explicit terrain cues, enabling it to learn a richer representation of field morphology than purely spectral networks.

From an operational standpoint, the benefits are substantial. Maintaining one checkpoint, rather than five, halves storage and model-management overhead and simplifies cloud deployment—an important practical barrier noted by Fritz et al. (2019). However, our data also confirm that*local fine-tuning remains worthwhile for extreme outliers**: in narrow terraced catchments of KwaZulu-Natal, the terrain-aware national model still under-segmented shadowed field edges. Hence, we advocate a tiered strategy: deploy the national model by default and trigger lightweight local adaptation only where systematic errors exceed tolerance, an approach echoed by the weak-supervision pipeline of Wang et al. (2022).

2.4.2. Influence of DEM-derived channels

Incorporating slope, aspect and local-relief layers increased national IoU by six percentage points (0.77 → 0.83) and halved the terrain-robustness index (0.13 → 0.07). These gains rival the five-point boost reported by Zhang and Roy (2022) when adding DEM derivatives to soil-type classifiers, but they have rarely been quantified for field delineation. Object-based image analysis (OBIA) theory argues that objects are best defined by *both* spectral and contextual attributes (Blaschke, 2010; Blaschke et al., 2014); DEM channels provide precisely the latter, signalling to the CNN where natural breaks in slope coincide with human-made boundaries. Without these cues, the RGB-only unified model systematically missed narrow terraces and mis-labelled shadowed valley bottoms, errors that Persello et al. (2019) also observed in hilly Italian orchards. Province-specific tuning reclaimed \~5 IoU points for RGB-only inputs, consistent with Wang et al.'s (2022) weak-supervision gains, but contributed < 1 pp once terrain variables were present, demonstrating sharply diminishing returns. The implication is clear: **physical context can substitute for large volumes of local labels**, an important consideration in data-scarce regions such as sub-Saharan Africa.

2.4.3. Why multiple metric families are essential

Reliance on a single accuracy metric risks misinterpretation. HRNet-U and Mask R-CNN-U achieved similar IoU (≈ 0.82) yet diverged by three Boundary-F1 points because Mask R-CNN produced crisper edges, a difference invisible to pixel scores alone. Conversely, a model can achieve high Boundary-F1 by tightly tracing an erroneously merged "mega-field", inflating edge agreement while destroying instance fidelity (Lavreniuk et al., 2023). Our triad of **pixel, boundary and terrain-stratified metrics**, therefore, paints a fuller error portrait. Terrain-stratified IoU reveals systematic under-performance on steep slopes, echoing observations by Xiong et al. (2017) that terrain can bias pixel-wise measures by > 10 pp. Furthermore, reporting class-wise IoU permits external benchmarking: the unified U-Net's steep-slope IoU of 0.78 compares favourably with the 0.72 reported for Himalayan terraces by Yan and Roy (2020) and the 0.76 obtained by the DEM-augmented Res-U-Net of Zhang et al. (2020). Such explicit context is indispensable for practitioners deciding whether a given model meets application-specific tolerances, for instance, South Africa's rebate scheme, which flags parcels whose mapped area deviates by >5 % from cadastral records.

2.4.4. Instance-level evaluation for Mask R-CNN and SAM

Because Mask R-CNN and the Segment Anything Model (SAM) output *distinct* parcel instances, instance-level AP is the appropriate yardstick (He et al., 2017; Kirillov et al., 2023). Mask R-CNN reached $AP_{50} = 0.76$ and mAP = 0.61, mirroring the 0.75/0.60 values reported by Wang et al. (2022) on Tanzanian orchards. SAM lagged slightly ($AP_{50} = 0.74$) and, consistent with Watkins et al.'s (2024) findings, tended to over-segment highly irregular fields when only sparse prompts were provided. These AP differences, though modest, translate into practical discrepancies: over-segmentation inflates field counts and complicates parcel-level yield modelling. Hence, *AP metrics are indispensable whenever parcel uniqueness has downstream value*, such as input-credit allocation or individualised advisory systems.

2.4.5. Positioning within the broader literature and implications

Our study extends the literature in three ways. First, we confirm at sub-metre resolution what Waldner and Diakogiannis (2020) found at 10 m: that one well-designed network can cross agro-ecological boundaries, contradicting assertions that smallholder landscapes necessarily require hyper-local models. Second, we quantify, for the first time, the role of DEM derivatives in stabilising field-boundary predictions across relief classes, validating OBIA's call for contextual features in the deep-learning era. Third, we adopt a multi-metric, terrain-stratified evaluation protocol aligning with Lavreniuk et al. (2023)'s recommendations, offering the community a template for fair comparison. Operationally, our unified model processes 100 km^2 tiles in 15 s—more than twice as fast as the ResUNet-a reported by Waldner & Diakogiannis (2020) and an order of magnitude faster than OBIA pipelines catalogued by Fritz et al. (2019). When paired with weak supervision (Wang et al., 2022) and crowdsourced labels (Fritz et al., 2019), such speed enables near-real-time national updates, a prerequisite for climate-smart subsidy schemes that target individual fields. Nevertheless, two limitations must be acknowledged: SAM's prompt sensitivity and residual errors in extreme topography. Future work should explore prompt optimisation and transformer-based instance heads (Lavreniuk et al., 2023) and uncertainty quantification to flag low-confidence boundaries for human review.

Overall, the evidence supports a hybrid strategy: deploy a terrain-aware national backbone, augment it with minimal local fine-tuning where slope exceeds 25°, and evaluate with pixel-, boundary- and instance-level metrics. This approach promises the accuracy of bespoke models with the scalability of a single pipeline, advancing the goal of equitable, data-driven support for the millions of smallholder farmers who cultivate the world's most complex landscapes.

2.5 Conclusion

This study underscores the feasibility and advantage of deploying a unified, terrain-aware field-boundary delineation model across diverse South African agricultural contexts. Despite variations in field size, shape, and topography, the national model attained consistently high segmentation accuracy (mean IoU = 0.84; Boundary-F1 = 0.79), with only marginal local fine-tuning gains in steep, terraced areas. Incorporating DEM-derived channels, slope, aspect, and local relief, was pivotal, boosting performance and stabilising predictions across heterogeneous terrains, thereby validating OBIA principles in a deep-learning framework. Multi-metric evaluation, including instance-level AP for Mask R-CNN and SAM outputs, revealed nuanced differences in edge fidelity and instance counting, underscoring the need for diverse accuracy assessments in operational settings.

Operationally, the single pipeline approaches half-management overhead and accelerates processing by an order of magnitude compared to traditional OBIA pipelines, offering a scalable solution for continuous national updates. Yet, the study also highlights the residual challenges of shadowed edges in steep terrain and the sensitivity of SAM to prompt density.

Overall, the evidence advocates a hybrid approach: adopt the unified, terrain-aware model as the default, with lightweight local adaptation triggered only where performance gaps emerge, and ensure evaluation across pixel, boundary, and instance metrics. This strategy balances the accuracy of bespoke models with the operational simplicity of a single pipeline, supporting equitable, data-driven decision-making for smallholders and commercial farming landscapes alike.

3. Remote sensing-based maize crop evapotranspiration mapping in the Maize Triangle Region

3.1. Introduction

3.1.1. General Overview

Due to its significant role in the characterisation of the climate system and its changes, evapotranspiration (ET) is a key Essential Climate Variable (ECV; https://gcos.wmo.int/site/global-climate-observing-system-gcos/essential-climate-variables). It is a crucial nexus between hydrological, carbon and solar energy cycles within terrestrial systems, with more than half of the solar energy absorbed by land surfaces used for ET, 60% of precipitation being returned into the atmosphere through ET. In vegetation and crop production, ET, particularly transpiration, is essential for facilitating the movement of nutrients from the soil into the plant and in the processes of respiration and photosynthesis. It is a measure of crop water requirements; hence, a vast amount of research has been done to measure and estimate this parameter, including direct measurements and different modelling approaches.

Accurate estimation of ET remains a challenge, due to its high spatiotemporal variability, which is further influenced by associated hydrometeorological processes (Brutsaert, 2023; Ward & Trimble, 2003). Before the emergence of remote sensing, evapotranspiration (ET) was primarily quantified through field measurements and estimated by models using meteorological and ancillary data. The traditional methods/ instrumentation used for ET measurements include lysimetry and porometry (Gebler et al., 2015), moisture depletion measurements like pan measurements (Hillel, 1982), atmospheric measurements, including micrometeorological and energy balance techniques like Bowen Ratio (Bowen, 1926), eddy covariance (EC) flux towers (Leuning et al., 1982; Monteith, John L. & Unsworth, 2013; Stull, 2012), and scintillometry (Liu, Y. Y. et al., 2013; Meijninger et al., 2006). Although they are highly accurate, these methods pose a challenge when it comes to monitoring ET over vast fields, because they only give point measurements, are extremely expensive, and difficult to install and manage in remote regions. They have, however, been used to evaluate the performance of models that have been developed to estimate ET across different landscapes, cropping and natural vegetation systems. The first ET model, developed by Penman (1948a), relied solely on external physical parameters. Monteith later modified it by incorporating physiological characteristics, resulting in the widely used

Penman-Monteith model (Monteith, J. L., 1981). Further modifications led to simplified versions requiring fewer inputs, such as the Stanghellini (Villarreal-Guerrero et al., 2012), Priestley-Taylor (Priestley & Taylor, 1972), and Hargreaves-Samani (Hargreaves & Samani, 1982) models. These models have been extensively evaluated and reviewed across different environmental conditions by numerous authors.

The advancement of remote sensing has further enabled ET assessment at different spatial and temporal scales. Several approaches have been developed and employed for ET estimation, including the energy balance (EB) approaches (Allen et al., 2007), the Penman-Monteith method (Cleugh et al., 2007), the Priestley-Taylor approach (Fisher et al., 2008; Jiang & Islam, 2001; Miralles et al., 2011), the Shuttleworth-Wallace approach (Zheng et al., 2018), the hydrological water balance method (Rodell et al., 2011; Zeng et al., 2012), empirical models (Wang, D. & Cai, 2008), the Soil-Vegetation-Atmosphere Transfer (SVAT) model (Ghilain et al., 2011), statistical models (Alemohammad et al., 2017), and the energy-balance Penman-Monteith method (Mallick et al., 2013). Many of these models have been reviewed and tested in different environments. In the South African context, several researchers have evaluated the Penman-Monteith and SEBS models (Dzikiti et al., 2019; Gibson et al., 2013; Majozi et al., 2017; Ramoelo et al., 2014). These studies highlighted the low accuracy of the models during the dry seasons.

Other studies have applied hybrid models that integrate machine learning with traditional ET models to improve prediction accuracy. For instance, Liu et al. (2024) combined physical constraints and machine learning methods to develop a hybrid ET estimation model based on surface conductance optimisation in HRB, northwestern China. A comparison with Penman–Monteith and Priestley–Taylor, and three pure machine learning algorithms (RFR, XGboost, and KNN), revealed that the hybrid ET model outperformed the others across different time scales, displaying the lowest BIAS, RMSE, and higher KGE. Hu et al. (2021) evaluated the performance of SEBS, DNN, RFR, and symbolic regression (SR), and a hybrid model. Their results showed the hybrid model performed better than the baseline SEBS, although it was worse than the ML models. Zhao et al. (2019) combined ANN algorithms with the Penman-Monteith method to estimate latent heat flux. Similarly, Antonopoulos & Antonopoulos (2017) assessed the performance of ANN alongside empirical equations for ET estimation.

3.1.2. Remote sensing-based evapotranspiration products

Efforts have also been made to improve the accuracy of ET estimation in water-scarce regions. Moreover, some have been applied at a global scale to produce global ET products, like MOD16, GLEAM, and LandSAF ET (Cleugh et al., 2007; Fisher et al., 2008; Miralles et al., 2011; Mu et al., 2011). Other ET products are produced using re-analysis modelling, for example, the ERA5-Land reanalysis ET, GLDAS and NLDAS ET. The challenge with most ET products, including reanalysis ET products, is their coarse spatial resolutions. This makes them unsuitable for application in precision crop water monitoring. We are focusing our review on medium spatial resolution ET products that can be used to assess crop water use in small and medium-scale fields.

3.1.2.1. MOD16 Evapotranspiration product

The MOD16 ET product runs the Penman-Monteith algorithm as modified by Mu et al. (2007), 2011) with MODIS (Moderate resolution Imaging Spectroradiometer) land cover, surface albedo, LAI, Enhanced Vegetation Index (EVI), and a daily meteorological reanalysis data set from NASA's Global Modelling and Assimilation Office (GMAO) as inputs to estimate global ET and potential ET. Initially adapted as a remote sensing-based ET model by Cleugh et al. (2007), the PM model was modified into a multi-source model by Mu et al. (2007, 2011), who split ET into daytime and nighttime estimates, whilst also computing total ET as the sum of evaporation from wet and moist soil, evaporation from wet canopy and plant transpiration through canopy stomata. The product comes at a spatial resolution of 500 m, at an 8-day temporal resolution.

This product has been validated against actual measurements in numerous regions against a network of global flux tower sites and basin-scale water balance calculations (Abid et al., 2024; Aguilar et al., 2018; Chen et al., 2022; Ren et al., 2025; Zhu et al., 2022), including studies in Africa (Cogill et al.; Manyari et al.; Palmer et al., 2023; Zimba et al., 2022). Mu et al. (2011) evaluated the algorithm against evapotranspiration observations from 46 eddy covariance flux towers in the United States and Canada. They reported that the average mean absolute bias values are 24.1% of the evaporation measurements. Kim et al. (2012) went on to validate MOD16 global terrestrial evaporation products at 17 flux tower locations in Asia and found good agreement at only five locations, with R from 0.50 to 0.76, bias -1.42 to 1.99 mm/8 day, RMSE 1.99 to 8.96 mm/8 day. They observed that the best performance of the product was in forested land cover sites.

In another study, Meng et al. (2023) evaluated crop ET from two remote sensing ET products, MOD16 and PML-V2, against EC flux observations from 28 crop sites globally. The results showed that although the overall accuracies of these two products were similar, the MOD16 product underestimated the 8-day ET with a bias of -2.31 mm/8 day, R^2 of 0.452 and RMSE of 8.82 mm/8 day, while the PML-V2 product slightly overestimated the 8-day ET with a bias of 0.51 mm/8 day, R^2 of 0.455 and RMSE of 8.81 mm/8 day. Andrade et al. (2023) assessed the performance of the MOD16 product in a vegetated area in the Amazon of the Jaru Biological Reserve. The authors reported that MOD16 overestimated ET with values ranging from 1.05 W m^{-2} in 2007 to 15.78 W m^{-2} in 2005.

3.1.2.2. WaPOR ET product

WaPOR (Water Productivity through Open access of Remotely sensed derived data) is a FAO portal to monitor agriculture water productivity over Africa and the Near East. The datasets provided on the platform include evapotranspiration and its components, at 300 m global, 100 m national African countries, and 20 m selected pilot project sites. It allows for direct data queries, time series analyses, area statistics and data download of key variables associated with water and land productivity assessments. The ET products are computed using the modified version of the ETLook model (ETLook-WaPOR) described by (Bastiaanssen et al., 2012). The ETLook is based on the Penman-Monteith algorithm, estimating soil and intercepted evaporation, and transpiration separately.

This product has undergone extensive evaluation, also as a tool for monitoring vegetation water use, and for catchment water resource management studies. Blatchford et al. (2020) evaluated the WaPOR ET products against *in situ* data from 14 eddy covariance stations across different climates in Africa. Their results indicate that although WaPOR is performing well, but with some noticeable overestimation in rainfed regions with low ET, and underestimation with high ET. The overall correlation was 0.71, and RMSE was 1.2 mm/ day. At catchment level, Tiruye et al. (2024) assessed the performance of WaPOR and the ERA5-Land reanalysis ET_o in Ethiopia. They reported that based on the RMSE, ERA5-Land performed better than WaPOR at 7 out of 10 weather stations, whereas both datasets demonstrated similar performance in 6 out of 10 weather stations when considering the index of agreement. An evaluation of the WaPOR ET product and the ETLook estimated ET driven by Copernicus data revealed that Copernicus-based

ET reached a correlation of 0.9, a mean bias of 0.3 mm/day, and RMSE of less than 1 mm/day when compared against the field lysimeter and eddy covariance measurements, achieving a better spatial-scale consistency than WaPOR data (R. Guzinski et al., 2021). Fakhar & Kaviani (2024) evaluated the WaPOR ET product and FAO-56 estimated ET across 16 provinces located in four provinces in Iran. They reported that the WaPOR ET product demonstrates the best correlation compared to FAO-56 ET in semi-arid regions, with an R^2 of 0.95 and an RMSE of 0.43.

3.1.2.3. ECOSTRESS ET product

The ECOsystem Spaceborne Thermal Radiometer Experiment on the Space Station (ECOSTRESS) ET products are provided the Jet Propulsion Laboratory. They are derived from the ECOSTRESS data using the Priestley Taylor-Jet Propulsion Laboratory (PT-JPL) and the disaggregation scheme Atmosphere Land Exchange-Jet Propulsion Laboratory (DisALEXI-JPL) algorithms, coming at a spatial resolution of 70 m and temporal resolution of 1-5 days.

These ET products have undergone extensive evaluations using eddy covariance flux data across the world. The initial performance assessment of the products was conducted by Fisher et al. (2020). They evaluated the PT-JPL against 82 eddy covariance sites worldwide, and reported an overall R2 of 0.88, and normalised RMSE of 6%. Liang et al. (2022) evaluated the ECOSTRESS ET products, i.e. ECO3PTJPL and ECO3ETALEXI, using 31 AmeriFlux towers in six regions across the USA. They revealed that both products overestimated ET in most sites, with DisALEXI having stronger correlations than PT-JPL, with R^2 0.45, and 0.23, respectively. In a more focused study, Wu et al. (2022) evaluated the performance of the ECOSTRESS ET products in agroecosystems, i.e. maize, wheat, soybeans, potato, switchgrass and brome grass, and prairie in the USA. Their results showed that DisALEXI performed better than PT-JPL compared with flux tower measurements, with correlation between DisALEXI and measured ET of over 70% of the sites being statistically significant ($p<0.05$). On the other hand, PT-JPL overestimated ET at several sites. ECOSTRESS LST data were used to produce ET products from the SEBS, TSEB, the non-parametric Surface Temperature Initiated Closure (STIC) model, and PT-JPL. These estimates were tested against flux measurements from 19 eddy covariance sites within 6 different biomes in Europe and Africa. They also reported that PT-JPL overestimated ET over savannas and shrublands. Liu et al. (2021) also revealed that the ECOSTRESS PT-JPL product overestimated ET in a temperate montane humid forest.

3.1.3. Maize crop water use estimation

Maize (*Zea mays L.*) is one of the world's staple crops, serving as a primary food, feed, and industrial raw material source. Maize plays a crucial role in global food security, due to its adaptability to diverse agroecological conditions. However, its growth and yield are significantly impacted by various environmental factors, including water availability, soil type, and climate. Water scarcity remains a critical challenge, particularly in dryland regions like Sub-Saharan Africa.

Maize is extremely sensitive to water deficit during key growth periods, like the flowering stage (Figure 8). The key water management periods that impact yield include the period from 20 to 30 days before flowering (8-10 leaf stage) to 10-15 days after, and the grain fill phase.

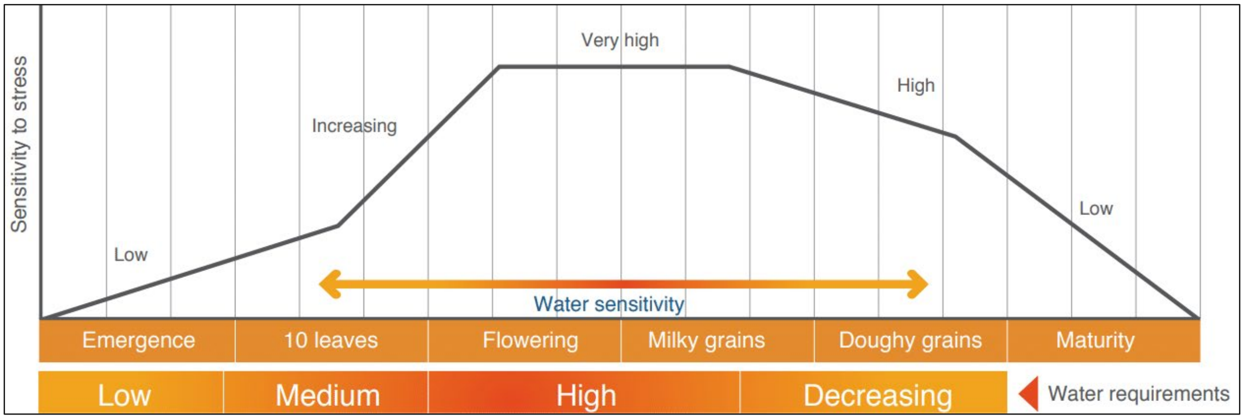

Figure 8: Maize crop sensitivity to water stress throughout its growth phases

Maize crop water use under rainfed conditions has been thoroughly investigated in different climates, even throughout its growth stages. The observed evapotranspiration values during the early stages of maize growth across different regions have been recorded to range between 0.8 and 2.8 mm/day. At peak growth stage, studies report evapotranspiration value ranges between 5.92 and 10.2 mm/day because of the fully developed crop canopies and high evaporative demand. The highest daily water consumption recorded was 7.74 mm/ day. The late development stage usually lasted 10–0 days with an average evapotranspiration of 2.3 mm/day. Seasonally, maize ET ranged between 411 and 530 mm, depending on location and associated climate.

Moreover, remote sensing-driven ET models have also been extensively evaluated to estimate maize crop water use. Costa-Filho et al. (2024) evaluated the performance of the Two-Source

Surface Energy Balance (TSEB) algorithms for the estimation of actual maize evapotranspiration (ET_a) using different multispectral data from Landsat-8, Sentinel-2, Planet CubeSat, multispectral radiometer (MSR) and a small uncrewed aerial system (sUAS) in a semi-arid climate region at Limited Irrigation Research Farm (LIRF), Greeley, USA. They demonstrated that the MSR data estimated ET was most accurate of the datasets, with the poorest performance being from Landsat-8. In a different study, Wang et al. (2023) assessed the performance of the Remote Sensing-based cropland Ecohydrological Model (ReSEM), a combination of the water-carbon coupled Penman-Monteith-Leuning (PML version 2) model and a process-based crop growth module in the computation of ET in maize and wheat fields in the North China Plain (NCP) and Hetao Irrigation District (HID) of China. Their results showed the RMSE of ET and GPP for winter wheat was 0.57 mm/day and 1.65 gC/ m^2day, and for maize were 0.80 mm/ day and 2.92 gC/ m^2day, respectively. Zhang et al. (2023) also evaluated the performance of FAO-56 dual crop coefficient approaches and the CWSI to estimate maize ET in the southwest region of Inner Mongolia, China. Their results showed that the combination of NDVI and CWSI produced the best estimates of maize ET_c, with an R^2 of 0.84 and RMSE of 0.50 mm/day. The DACT-based model also performed well, with an R^2 of 0.77–0.80 and RMSE of 0.53 mm/day.

Recently, machine learning algorithms such as decision trees, support vector machines (SVM), artificial neural networks (ANN), and deep learning techniques have gained traction in ET estimation using remote sensing data. Various studies have evaluated their performance and applications. Shao et al. (2023) developed models for crop coefficients (K_c) estimation using UAV remote sensing and ML techniques, ML algorithms (linear regression, polynomial regression, exponential regression, random forest regression, support vector regression, and deep neural network, for ET estimation in irrigated maize in a semi-arid region in Northwest China. The RFR with the highest accuracy with an R^2 of 0.69 and an RMSE of 0.1019. In another study, Nagy et al. (2024) evaluated linear and power regression models to estimate the crop coefficient (K_c) from Sentinel-2-based NDVI, NDWI, NDRE and LAI, to improve ET determination in crop fields in the Po Valley, Italy. NDWI and NDVI-based ET_c best performed in both the cases of linear (NDWI RMSE: 0.43 ± 0.12; NDVI RMSE: 0.43 ± 0.095) and power (NDWI RMSE: 0.44 ± 0.116; NDVI RMSE: 0.44 ± 0.103) approaches. Sun et al. (2025) investigated the performance of a time series LST-VI space method and ML- gradient boosting decision tree, Random Forest Regression, partial least square regression, K-Nearest Neighbours, backpropagation neural network, and support vector regression, for ET estimation under conditions of limited observed variables in Daxing and Huailai agricultural ecosystems. They compared their results with flux data and MOD16 ET, their results showing that RFR outperformed the rest of the methods tested. Xu et al. (2018) utilised machine learning methods to upscale ET from flux towers to a regional scale. Tang et al. (2018) employed a support vector machine (SVM) and an artificial neural network optimised by a genetic algorithm in modelling ET_a in a rainfed maize field under non-mulching and partial plastic film mulching. Fan et al. (2019) evaluated the ability of different ML algorithms (SVM, RF, extreme gradient boosting algorithm (XGboost)) in estimating ET and found SVM performed the best with satisfactory accuracy and stability.

In essence, ET remains a fundamental variable in climate and agriculture studies, and advancements in remote sensing and machine learning have significantly improved its estimation at various scales. The integration of traditional and modern approaches continues to refine ET modelling, offering more precise and efficient methods for understanding water and energy cycles in terrestrial ecosystems.

This part of the project aimed to evaluate and compare the performance of three remote sensing-based ET estimation approaches (i) a Penman-Monteith (PM) model, (ii) the ECOSTRESS Priestley-Taylor Jet Propulsion Laboratory (PT-JPL) ET product, and (ii) the FAO WaPOR ET product in semi-arid maize croplands of South Africa. Their spatiotemporal behaviour, consistency, and responsiveness to environmental conditions and highlight differences and complementarities among the models, were assessed.

3.2. Materials and methods

3.2.1. Maize production in South Africa

As a staple crop of South Africa and the broader southern African region, maize (*Zea mays* L.) is the most significant agricultural commodity in the region (Mangani et al., 2019; Nagy et al., 2024). It is the region's most extensively cultivated field crop, with South Africa being the leading maize producer on the African continent. Most of the production is concentrated in the Free State (FS), North West (NW), the Mpumalanga Highveld (MP), Gauteng (GP), and the KwaZulu-Natal Midlands (KZN), a region commonly referred to as the 'maize triangle' (Figures 9 and 10) (Walker & Schulze, 2008).

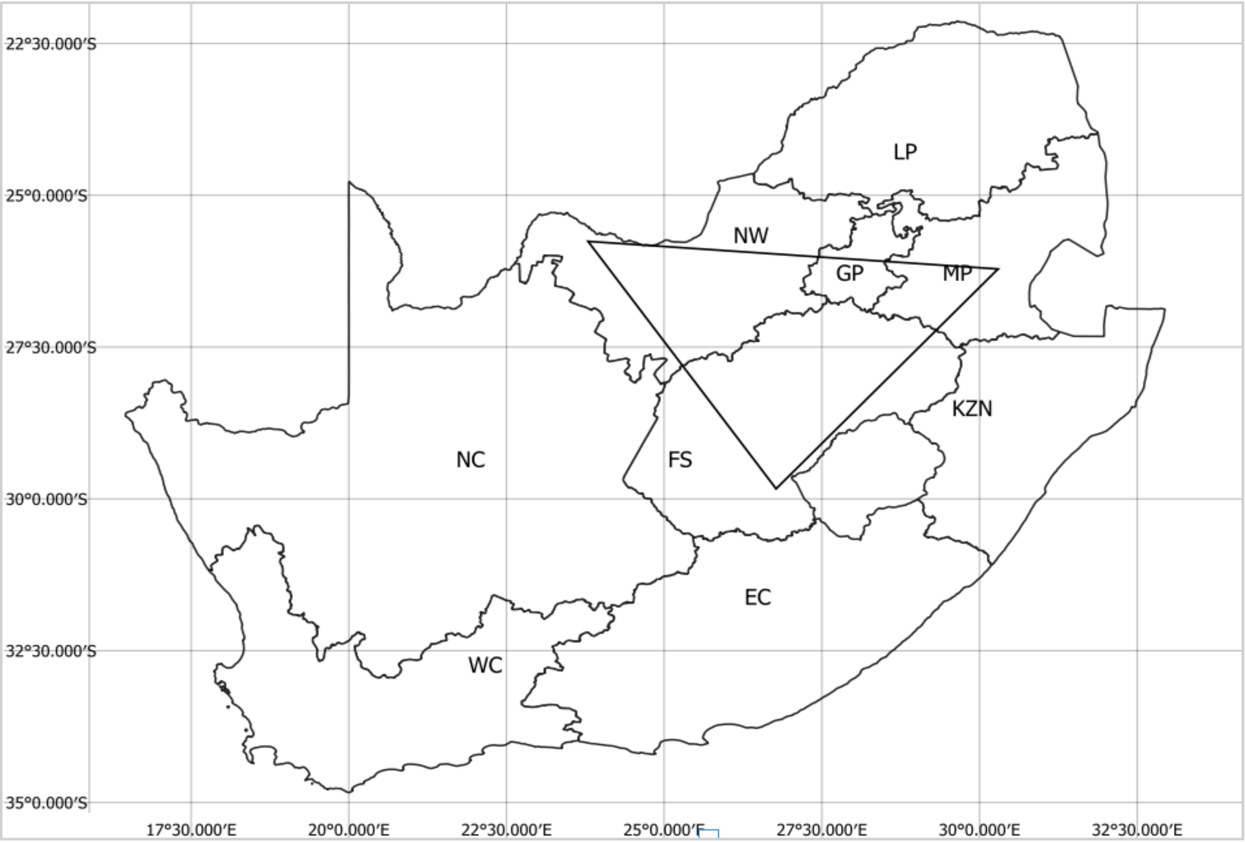

Figure 9: Map demonstrating the maize triangle in the Highland region of South Africa

The main crop season in South Africa extends from November to April of the following year. Maize is, thus, sown between October and December, once sufficient rainfall has provided the necessary moisture for seed germination. Planting times vary between the eastern and western production regions due to differences in temperature, rainfall patterns, and the length of the growing season. Depending on the variety and climatic conditions, maize requires between 90 and 120 days to reach maturity.

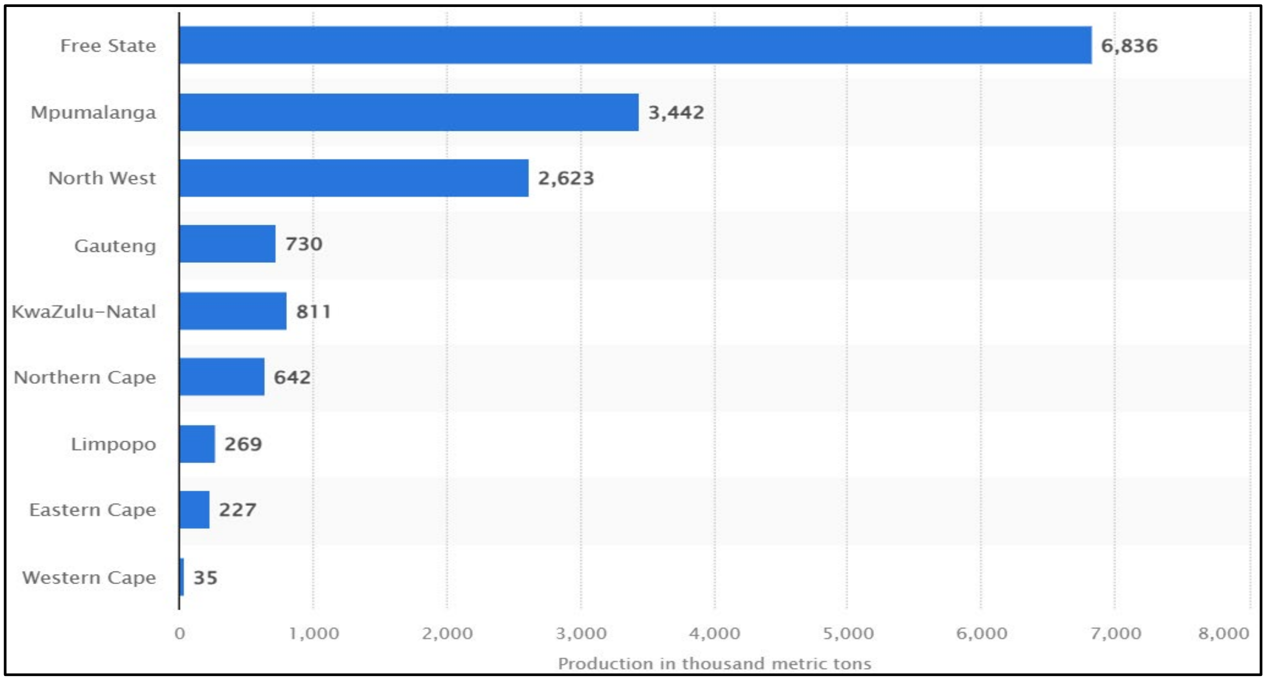

Figure 10: Maize production by province in South Africa for the 2022/23 season (in 1000 tons) (Source: https://www.statista.com/statistics/1135488/maize-production-in-south-africa-by-province/)

In South Africa, maize yield has fluctuated over the years. During the 2022/2023 season, maize production was approximately 15.6 million tons, marking a 2% increase compared to the previous season. Earlier, a significant drop of about 8.2 million tons was recorded in the 2015/2016 season, primarily due to the El Niño phenomenon between 2015 and 2017. However, despite these fluctuations, the overall trend from 2000 to 2022 indicates a growth of approximately 96.3%. Therefore, enhancing maize production, particularly among small- and medium-scale farmers, is crucial to meeting the demands of a growing population and ensuring food security in the region.

3.2.2. Research site selection

The research was conducted on the peripheries of Gauteng Province (Figure 11), within South Africa's maize triangle. Medium-scale farms owned by emerging farmers were selected at three locations: Vereeniging (27.70695 E, -26.51581 S), south of Johannesburg, Magaliesburg (27.454093° E, -26.072572° S) on the boarder of Gauteng and North West, and Bronkhorstspruit (28.83328 E, -25.55871 S), east of Pretoria on the border of Mpumalanga and Gauteng provinces.

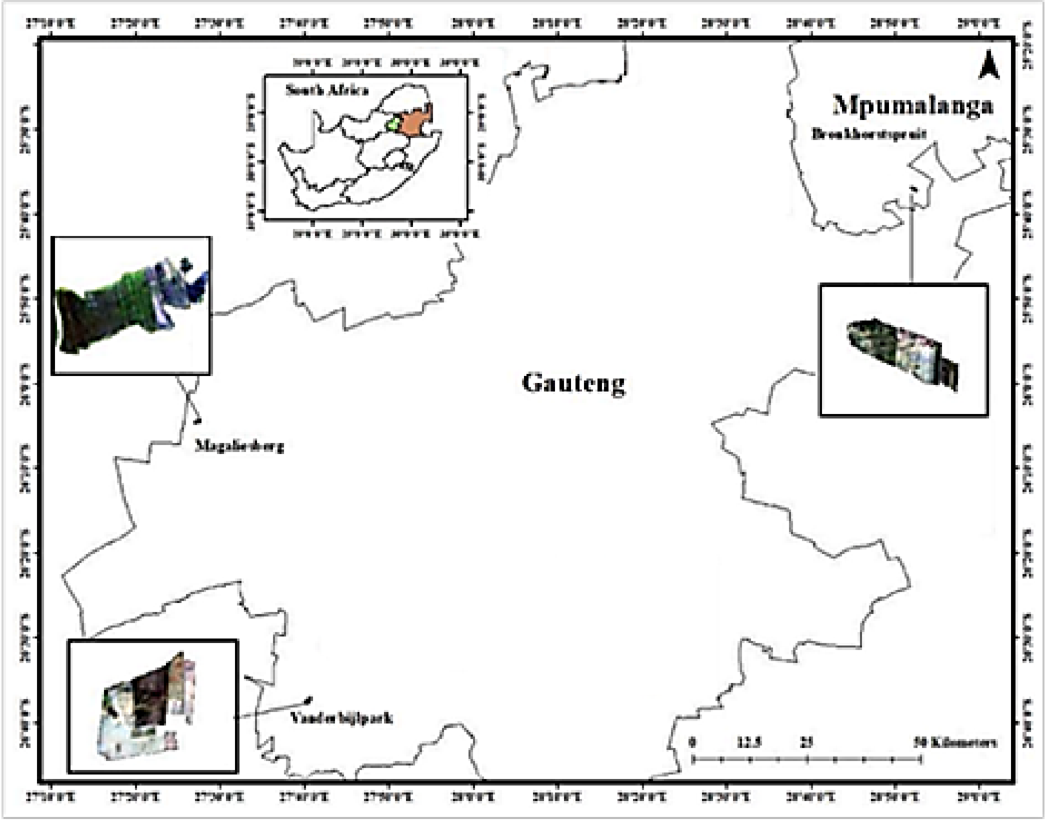

Figure 11: Location of the selected study sites on the peripheries of Gauteng province

Vereeniging lies within the Sedibeng District Municipality, near the confluence of the Vaal and Klip Rivers. It is a major manufacturing hub in South Africa (Nomad Consulting, 2018), with key economic activities including coal mining, steel, glass, brick, and iron manufacturing, alongside maize farming in the surrounding agricultural areas. The region, part of South Africa's Highveld, experiences warm summers (October to March) with an average high temperature of 26°C, while winter months (May to August) have an average high temperature of 20°C (https://weatherspark.com, accessed on 10/02/2025). The wet season runs from September to May, with peak rainfall in December and January, averaging approximately 89 mm.

Bronkhorstspruit, located within the Tshwane Metropolitan Municipality about 50 km east of Pretoria, is recognised for its fertile farmland and high agricultural productivity, as noted by the Tshwane Economic Agency. The area has a temperate highland tropical climate, characterised by warm, dry winters and long, hot, wet summers. The annual mean temperature is 22.05ºC, slightly above the national average by 0.83%. The region receives an average annual rainfall of 625 mm, with the highest precipitation occurring between October and March, while the driest months are from June to August.

3.2.3. Model description

In this study, the Penman-Monteith model, which has been redefined as a multi-source model, was used to model maize crop evapotranspiration. Developed and modified by Penman (1948b) and Monteith (1965), this model was adopted to spatially estimate ET using MODIS data (Cleugh et al., 2007). Mu et al. (2011) then modified the model by adding vapour pressure deficit and minimum temperature to constrain stomatal conductance, using enhanced vegetation index instead of NDVI to calculate vegetation cover fraction and included the separate calculation of soil evaporation. Further improvements were made to the algorithm, including calculating ET as a sum of the day- and night-time ET, adding soil heat flux calculation, separating dry and wet canopy surfaces and soil surface into saturated wet and moist surface, and improving stomatal conductance, aerodynamic resistance and boundary layer resistance estimates (Mu et al., 2011). Considering that relative humidity and, by extension, vapour pressure deficit, were soil moisture stress proxies in Mu et al. (2007), 2011), Sun et al. (2013) used the soil moisture index estimated from the Ts-VI method to constrain soil evaporation.

This model has been evaluated under natural systems in South Africa, with results indicating higher accuracy during periods of higher ET, and worse performance under dry conditions (Dzikiti et al., 2019; Majozi et al., 2017). Hence, the study to explore it in agricultural ecosystems. The Penman-Monteith equation is as below:

$$\lambda E = \frac{s*A+\rho+C_p*VPD/r_a}{s+\gamma*\left(1+\frac{r_s}{r_a}\right)} \tag{13}$$

where λE is the latent heat flux (Wm^{-2}) and λ is the heat of vaporisation (Jkg^{-1}), s is the slope of the curve relating saturated vapour pressure to temperature (PaK^{-1}), A is available energy (Wm^{-2}), ρ is the air density (kg/m^3), Cp is the specific heat capacity of air (J/kg/K), γ (Pa/K) is the psychrometric constant, e_{sat} is the saturation vapour pressure (Pa), e is the actual vapour pressure (Pa), where vapour pressure deficit (VPD), r_a (s/m) is the aerodynamic resistance, and r_s (s/m) is the canopy resistance, which is the reciprocal of canopy conductance gc ($gc={}^{1}/_{rc}$).

As a multi-source model, the model is split into:

i. Soil evaporation, which is a combination of wet soil evaporation, and potential soil evaporation and a soil moisture constraint function described in the Fisher et al. (2008) ET model.

$$\lambda E_S = \frac{\left(s * A_{soil} + \rho + C_p * VPD * \frac{(1-F_c)}{r_{as}}\right) * F_{wet}}{s + \gamma * \left(1 + \frac{r_{tot}}{r_{as}}\right)} + \left(\frac{\left(s * A_{soil} + \rho + C_p * VPD * \frac{(1-F_c)}{r_{as}}\right) * 1 - F_{wet}}{s + \gamma * \left(1 + \frac{r_{tot}}{r_{as}}\right)} * \left(\frac{RH}{100}\right)^{VPD/\beta}\right) \quad (14)$$

where β was set as 200 in the improved algorithm.

ii. Transpiration

$$\lambda E_T = \frac{\left(s * A_c * F_c + \rho + C_p * VPD * \frac{(F_c)}{r_a}\right) * 1 - F_{wet}}{s + \gamma * \left(1 + \frac{r_s}{r_a}\right)} \quad (15)$$

iii. Interception evaporation

$$\lambda E_I = \frac{\left(s * A_c * F_c + \rho + C_p * VPD * {}^{F_c}/_{r_{hcrc}}\right) * F_{wet}}{s + \gamma * \left(\frac{P_a * C_p * rvc}{\lambda * \varepsilon * rhrc}\right)} \quad (16)$$

where the resistance to latent heat transfer (rvc) is the sum of aerodynamic resistance (rhrc) and surface resistance (rs)

Total evapotranspiration was then calculated as the sum of the three components:

$$\lambda E_{TOT} = \lambda E_S + \lambda E_T + \lambda E_I \quad (9)$$

Modelling ET for the maize fields followed the steps presented in Figure 12.

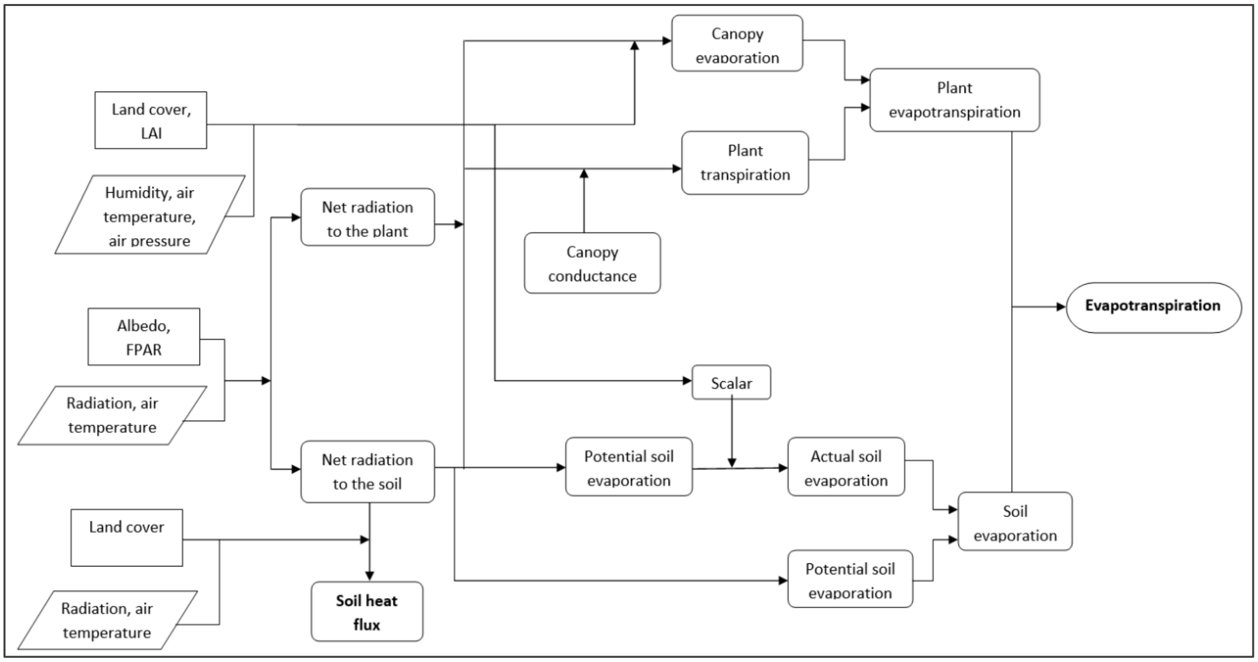

Figure 12: Flow diagram for ET modelling

3.2.4. Datasets

Meteorological data

For modelling evapotranspiration in the fields, hourly meteorological data, i.e. air temperature, relative humidity, wind speed, and atmospheric pressure, from the automatic weather stations that were nearest to the Vereeniging (27.70695 E, -26.51581 S), and Bronkhorstspruit (28.83328 E, -25.55871 S) farms were acquired from the South African Weather Station (SAWS). Data were acquired for a period from November 2021 to May 2022, which aligned with the summer maize growing season within the Maize Triangle.

Remote sensing datasets

Different remote sensing datasets were utilised for this study:

i. Harmonised Landsat Sentinel-2 product: https://appeears.earthdatacloud.nasa.gov/- 30 m spatial resolution, improved temporal resolution. Vegetation indices and surface albedo were derived from this dataset.
ii. ECOSTRESS: downloaded from https://appeears.earthdatacloud.nasa.gov/. This dataset provides land surface temperature (LST) and surface emissivity (Es) data inputs.

ECOSTRESS also presents evapotranspiration products derived using the JPL PT and DisALEXI algorithms, at 70 m. It should be noted that this is an experimental mission set to provide data for a short period of time; hence, it cannot be planned as an input into the development of any operational product.

iii. Harmonised Sentinel-2 product: downloaded from https://appeears.earthdatacloud.nasa.gov/. Available at 30 m spatial resolution, the dataset has improved temporal resolution.

The modelled ET results were then evaluated against existing ET products, such as the ECOSTRESS, WaPOR.

Table 6: Evapotranspiration products overview- algorithms used, input datasets and outputs

	WaPOR ET	**ECOSTRESS PT-JPL ET**
Algorithm applied/ used	Penman-Monteith (PM) based ETLook model described in Bastiaanssen et al. (2012)	PT-JPL algorithm based ECO3ETPTJPL as described by Fisher et al. (2008)
Input datasets	Meteorological data (solar radiation, air temperature, vapour pressure and wind speed)- MERRA/GEOS-5	Meteorological data (solar radiation, air temperature, vapour pressure and wind speed)- GMAO/MERRA
	Precipitation- CHIRPS v2, CHIRP Surface albedo- MOD09GA, MOD09GQ NDVI- MOD09GQ Soil moisture stress- MOD11A1, MYD11A1 (LST) Solar radiation- SRTM (DEM), MSG-transmissivity Land Cover- WaPOR LCC product	NDVI, SAVI, and albedo- Landsat atmospheric properties- MODIS surface emissivity and LST- ECOSTRESS Landcover
Outputs	Evaporation, transpiration, interception and ETa- decadal, monthly, annual, (national at 100m)	ETdaily, ETcanopy, ETsoil, ETinterception, instantaneous ET at 70m

3.3. Results and discussion

3.3.1. Temperature and rainfall statistics

Evapotranspiration is a result of a myriad of factors, including meteorological- air temperature, solar radiation, wind, atmospheric pressure and rainfall, vegetation type, and crop growth stage. Figure 13 shows air temperature and rainfall records for two study regions, Vereeniging and Bronkhorstspruit, during the 2021-2022 summer maize growing season, i.e. from November to May. The mean monthly temperatures ranged between 13 °C in May and 28. °C in January (Vereeniging), and 7.7 °C in November and 23.6 °C in February (Bronkhorstspruit).

Moreover, records indicate that rainfall was consistent throughout the season. Vereeniging received 641.2 mm of rainfall during the same period. This amount was 16.6% less than the rainfall recorded in Bronkhorstspruit.

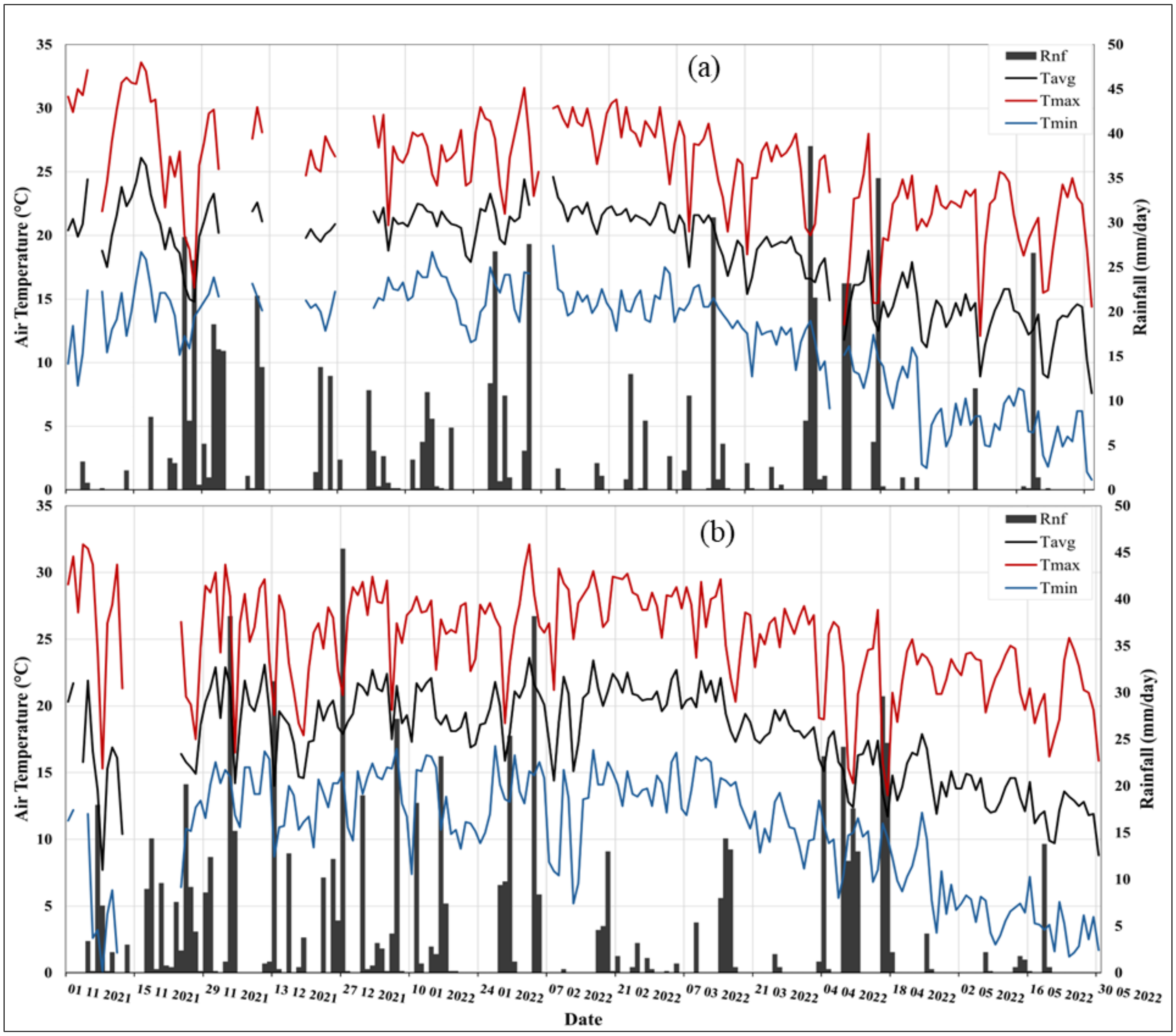

Figure 13: Recorded rainfall and air temperature for the crop growing season 2021-2022 in (a) Vereeniging and (b) Bronkhorstspruit

3.3.2. Maize crop growth monitoring

Remote sensing-based crop growth parameters, like NDVI, were used to assess the growth of the crop during the 2021-2022 growing season.

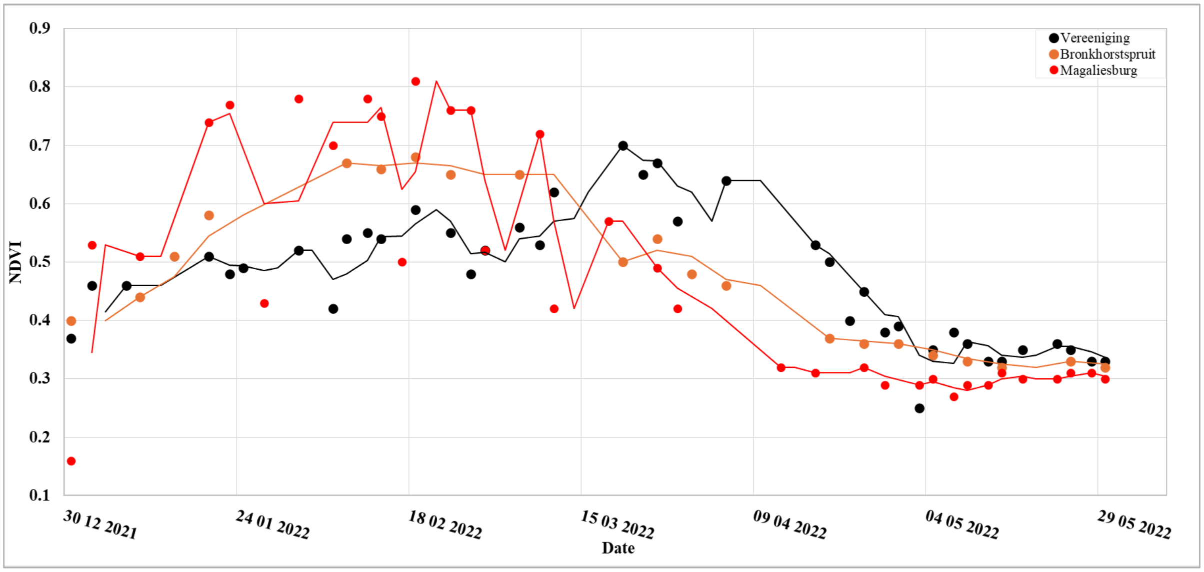

Figure 14: NDVI time series for the three maize fields in Vereeniging, Bronkhorstspruit and Magaliesburg

3.3.3. Evapotranspiration estimates for maize

In this study, daily and monthly analyses of ET were conducted to better understand the temporal dynamics of ET during different crop growth stages for the 2021/2022 maize growing season. The

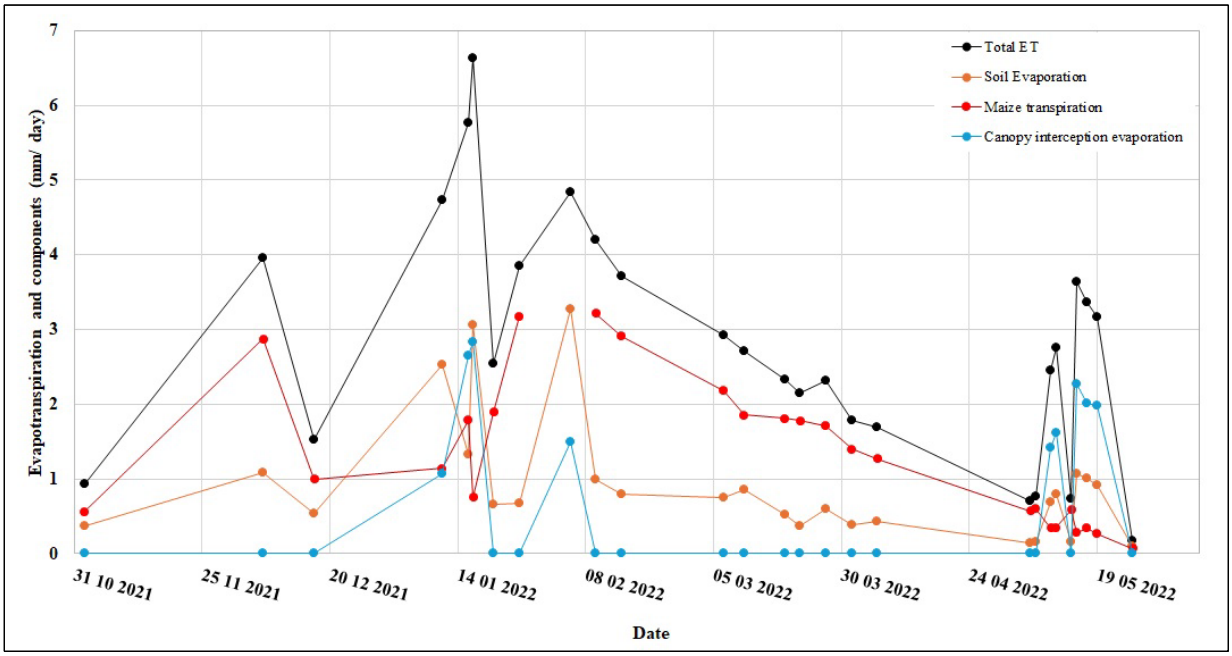

Figure 15: Results of Penman Monteith modelled maize crop ET for the 2021-2022 season

Penman-Monteith model was used to estimate maize evapotranspiration across the growing season, i.e. from November 2021 to May 2022.

The different ET components were estimated separately and combined to obtain the total value of maize field ET (Figure 15). Soil evaporation ranged between 0.1 mm/day at the beginning of the season and 3.28 mm/ day as the season wound down in May. This averaged 0.90 mm/day for the duration of the season. Meanwhile, transpiration showed a steady increase from the beginning of the season at 0.56 mm/ day, peaking at 3.22 mm/day, an amount that aligns with the period of maximum crop growth. Canopy interception evaporation estimations associate directly with rainfall events, ranging between 0.8 mm/ day on tilled fields and 5.2 mm/ day at peak maize growth (NDVImax – Figure 15). Lastly, total ET ranged between 0.17 mm/ day on tilled fields and 6.63 mm/ day at peak maize growth (NDVImax – Figure 15).

Figure 16 shows the spatiotemporal variation of evapotranspiration progression as the maize grew into maturity for the Vereeniging maize field.

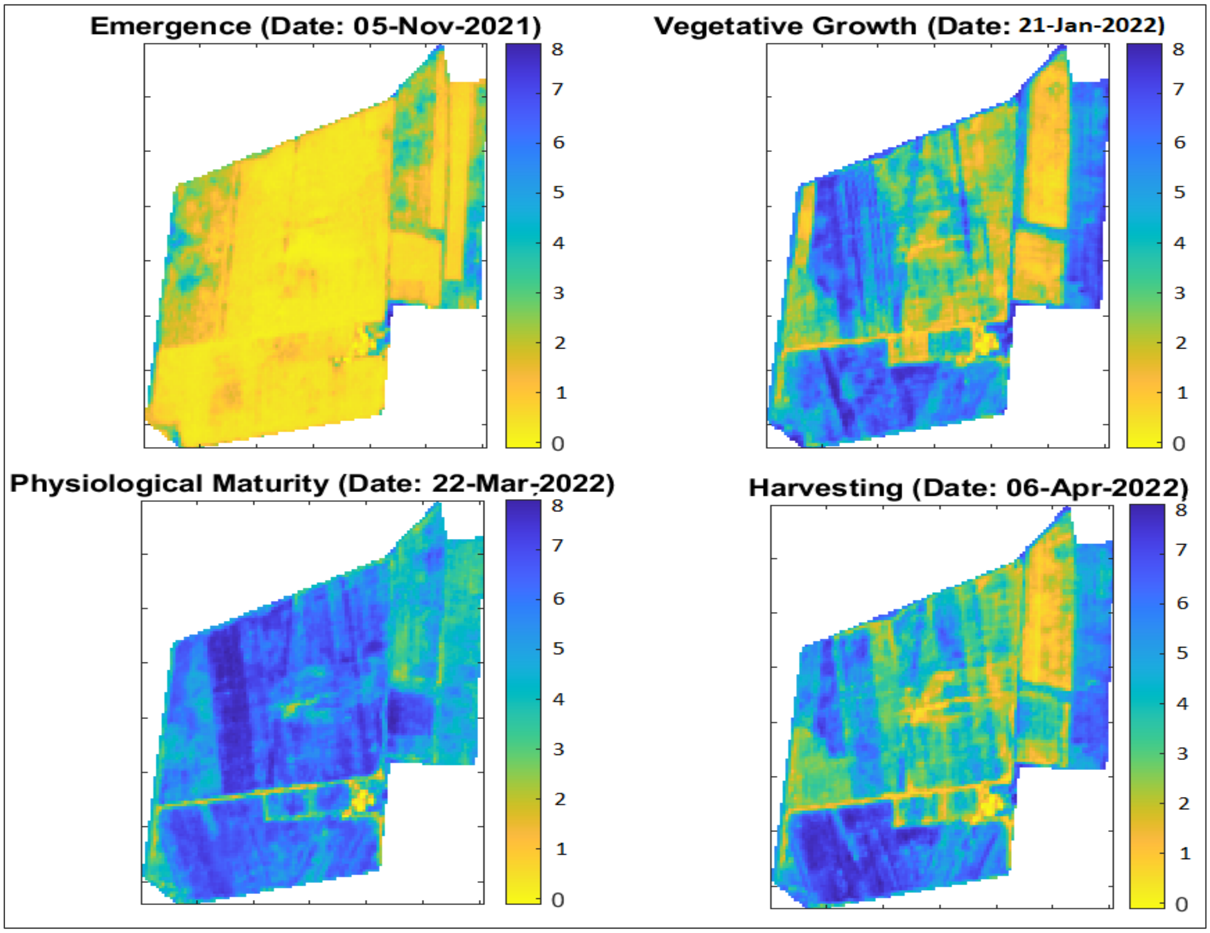

Figure 16: Spatiotemporal variation of ET throughout maize growth

3.3.4. Comparison of maize evapotranspiration estimates

The modelled ET was compared with WaPOR and ECOSTRESS ET products as shown in Figure 17. While daily ET are essential for understanding short-term fluctuations of ET, they are also valuable to assess the sensitivity of different ET models to respond to short-term variations in environmental conditions (particularly changes in temperature, rainfall, soil moisture, etc). In addition, daily ET trends are essential to reveal the impact of temporal resolution on the type of trend that can be achieved with each model (i.e. a smoother trend may be observed where temporal resolution is low). On the other hand, monthly ET trends are essential for revealing an overall seasonal pattern, providing insights into stages where ET reaches its highest levels. The values of the ECOSTRESS ET ranged from 1.03 mm/ day at the end of the growing season to 6.22 mm/ day at peak growth in mid-March. While all models seem to align on the timing of peak daily ET observed, the magnitude varies, and the PM modelled ET and PT-JPL generally estimate higher peaks than WaPOR, which are relatively conserved. We conclude that variations in ET magnitude could be because of differences in model structures, input and underlying theories; however, there is a need to further investigate how each of these factors influences model predictions.

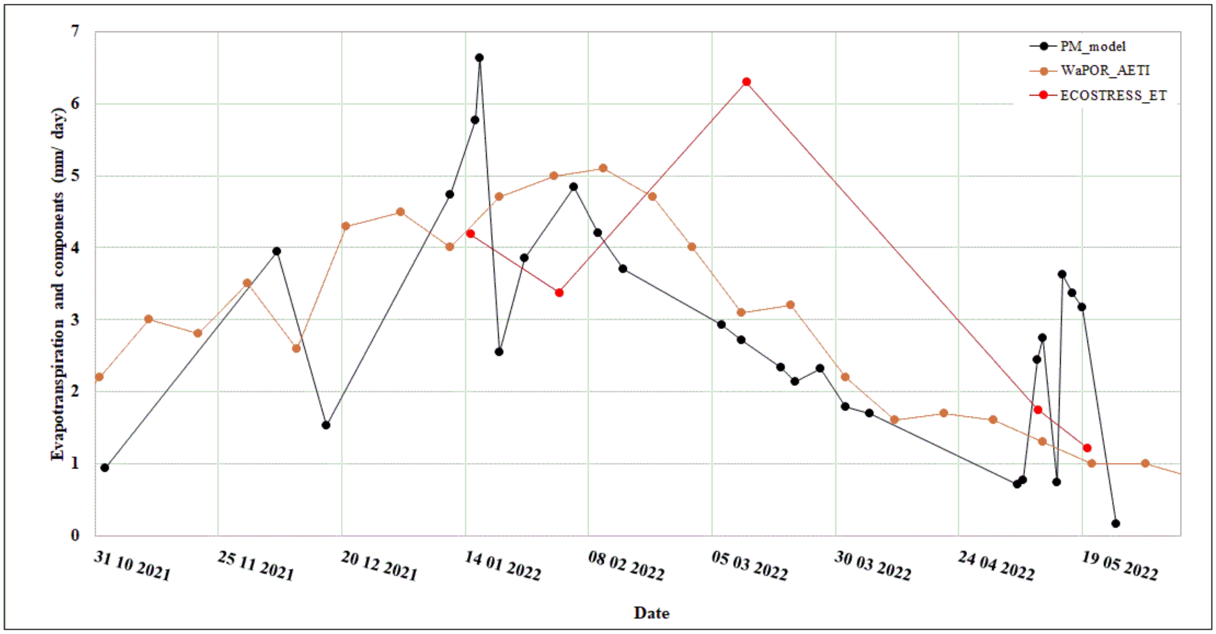

Figure 17: Time series of daily ET estimates (PM modelled, PT-JPL, and WaPOR**)**

Results of our simulation are comparable to other studies- Maize daily actual evapotranspiration (ETa) varied from 0.23 to 10.2 mm, and the seasonal ETa varied with year and ranged from 634.2 to 697.7 mm, averaging 665.3 mm in a study by Djaman et al. (2018). The APSIM model was used to estimate ET in a maize field in Aowa, giving values ranging from 0.2 to 6.35 mm/ day. Dayoub et al. (2024) investigated the effect of biochar on a maize ET_a, reporting that ET_a for 400 kg ha^{-1} biochar ranged from 1 to 5.6 mm/day, and from 0.9 to 5.6 mm/day.

3.2. Spatial variations of maize Evapotranspiration

While temporal variation of ET is valuable for monitoring seasonal crop water use scheduling by identifying periods of peak water demand throughout the day, understanding spatial variation is equally critical, as it highlights specific zones within a field that experience higher ET, in comparison to those with low ET.

The spatial variation of maize evapotranspiration (ET) estimated using the PM model, PT-JPL, and WaPOR products is illustrated for four key phenological stages: emergence, vegetative growth, tasselling and silking, and grain filling. Each model reveals distinct spatial patterns, with notable differences in heterogeneity, magnitude, and hotspot locations.

For PM ET, the spatial distribution during the emergence and vegetative stages appeared relatively uniform, with minimal heterogeneity across the study area. However, during the tasselling and grain filling stages, substantial spatial variation emerged. Notably, ET exceeded 6 mm/day in the far southern, eastern, and western zones, as well as in some parts of the central region, indicating increased water demand during the peak reproductive phases. The PT-JPL model, although less spatially smoothed, still captured discernible patterns of ET variation. Spatial differences began to emerge at the vegetative stage and became more pronounced during tasselling and grain filling. High ET values were concentrated in the north-western, north-eastern, and eastern parts of the study area in stage 3, and during grain filling, these high-value zones extended further south. WaPOR-derived ET maps exhibited a blockier appearance, likely due to pixel resolution, yet still reflected meaningful spatial differences. From the emergence stage, elevated ET values were observed in the western part of the study area. These values progressively increased over the subsequent stages, culminating in stage 4 with noticeable ET peaks in both the southern and north-western zones.

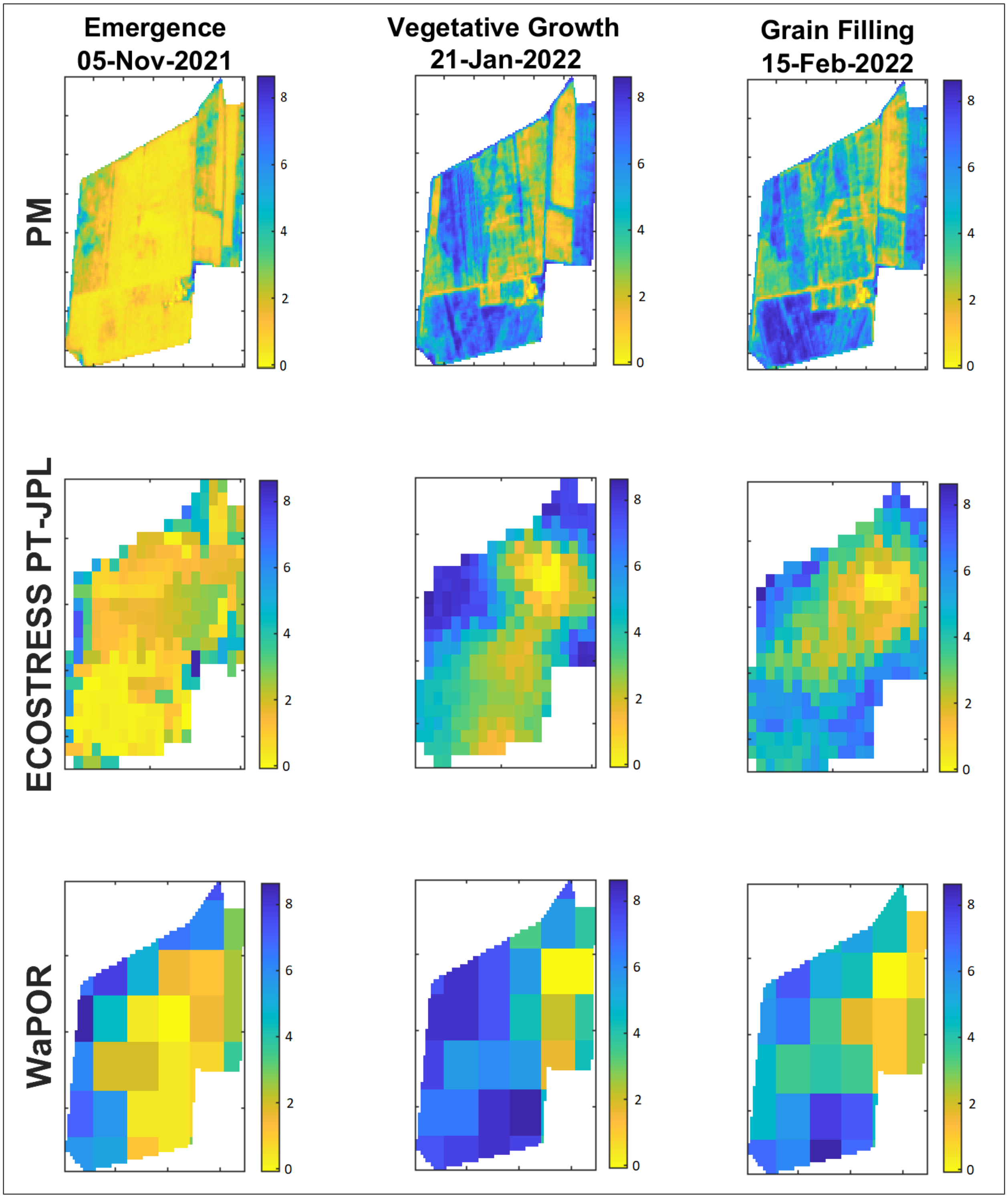

Figure 18: Visualisation of ET maps of three different products

It is important to note that while ECOSTRESS PT-JPL ET estimates are intended to provide relatively high temporal resolution estimates (3 to 5 days), our study area had limited data available, which resulted in coarser actual temporal resolution as seen in Figure 17. As such, it is crucial to consider data availability for the area of interest before adopting estimates from any products that may generally be of high temporal resolution, but due to limited data for the area of interest, result in low actual temporal resolution. Some studies have shown that temporal resolution can significantly affect the performance of ET models, while high temporal resolution data allows models to better capture detailed and peak changes in ET, whereas low temporal resolution data often smooths out peaks and can lead to underestimation. As such, the choice of temporal resolution should align with the specific requirements and objectives of the study. As expected, the results in this study confirms that utilising lower temporal resolution data (i.e. PT-JPL) results in a smoother daily trend, whereas higher temporal resolution data (i.e., PM-ET) shows a more variable daily trend capturing finer fluctuations over time (Figure 17).

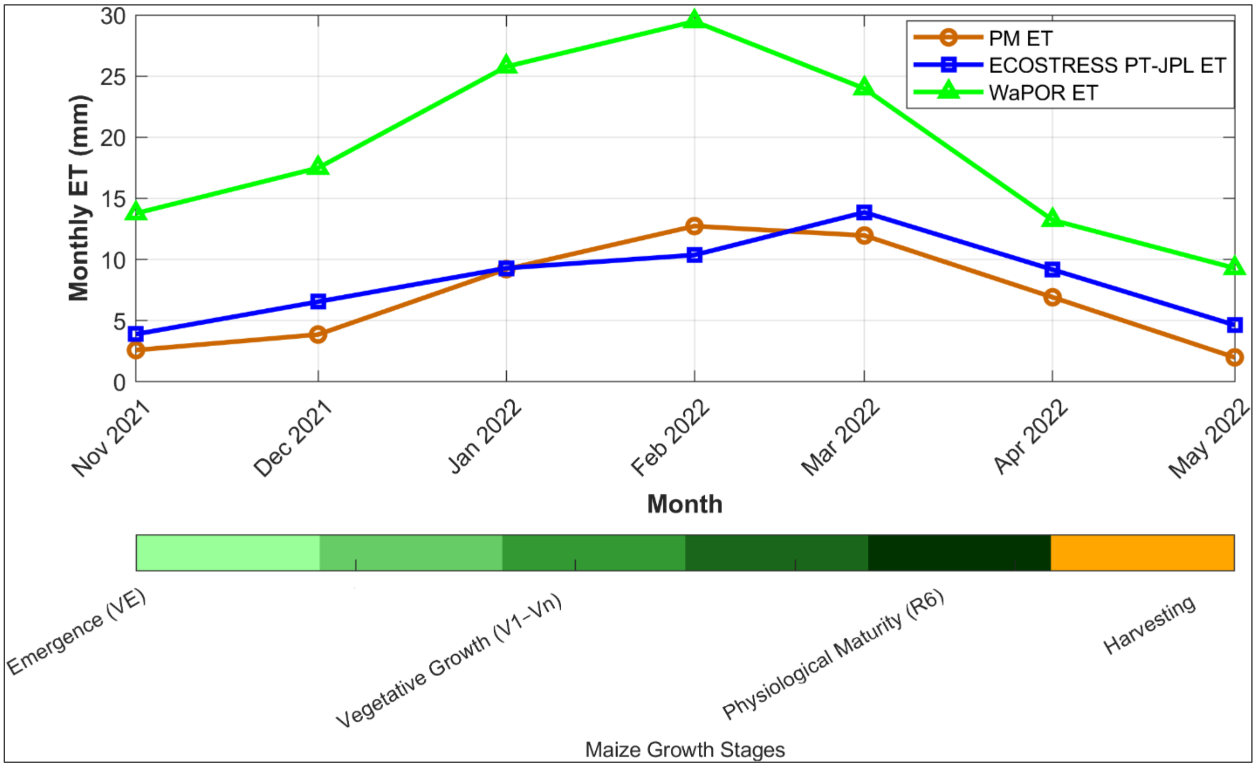

Figure 19: Monthly ET trend for maize with Phenological Stage Indicators at the bottom

To provide insights on how seasonal ET patterns align with crop development, the monthly ET trend was overlaid with maize phenological stages (Figure 19). All three models capture seasonal ET patterns depicted by a unimodal distribution (Figure 19) which aligns with maize growth stages. During the early growth stage (VE-Vn) when the canopy is still developing, low monthly

ET are observed across all models (i.e. below 5 mm/day with PM & PT-JPL) and these align with low water use during this period. During the grain filling stage, a pronounced peak in monthly ET is observed across all models. This is due to the crop reaching its maximum LAI and heightened photosynthetic activity, leading to increased transpiration and overall evapotranspiration (ET). These results correspond well with FAO crop water requirements during the growth period, which shows that mid-season is the period where crop water needs reach their highest (and that includes the grain filling stage). A gradual decline in ET estimates is observed across all models from the month of March to April during the grain filling, physiological maturity and harvesting stages due to reduced transpiration as maize reaches maturity and senesces. Despite capturing the overall seasonal pattern as expected, variations in ET magnitude among models reflect distinct sensitivities of models to input parameters and underlying parameterisations for energy balance calculations.

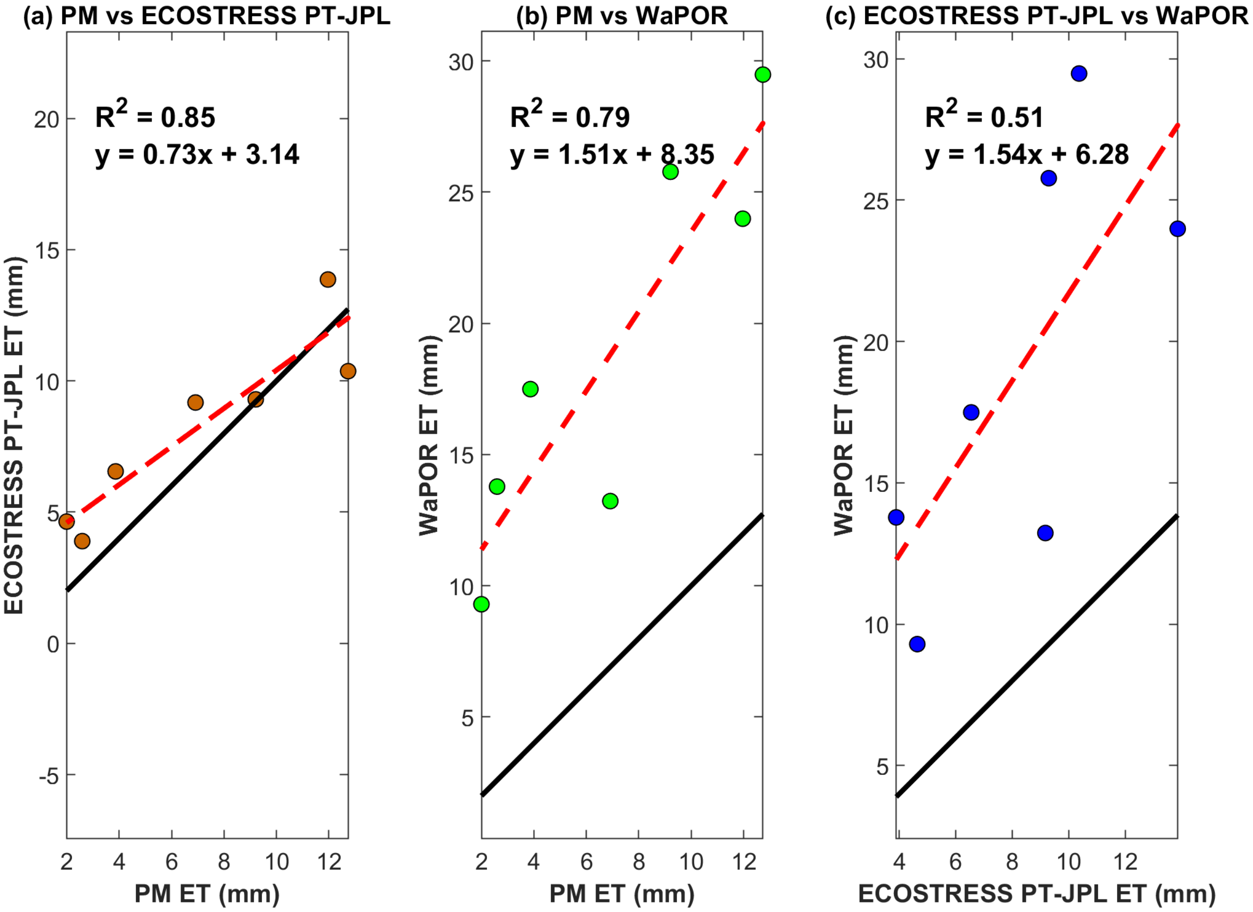

Figure 20: Intercomparison of PM modelled ET against ECOSTRESS and WaPOR

4. Yield prediction using remote sensing

4.1. General overview

Agriculture plays a significant role in the economic development of the country, contributing directly to household food security. It is reported that about 9% of agricultural output is produced by previously disadvantaged farmers, particularly for small- and medium-scale (emerging) farmers, implying a growing in the sector is growing. Despite facing challenges like a lack of inputs and equipment resources, poor infrastructure, unsustainable farming practices, and climate change, small-scale farmers hold tremendous potential to contribute to the country's economy.

Together with wheat and rice, maize is one of the top three world food crops. Of the total African production where it is a staple, South Africa accounts for 30.4%. The consensus is the need to improve productivity, especially in rainfed systems in small and medium-scale crop production. This entails maximising yield to a fine scale. This can be achieved by good knowledge and understanding of the within-field yield variation and its causes are essential. Meanwhile, accurate, early crop yield forecasting is needed by different stakeholders, like farmers, input manufacturers, insurance companies, commodity brokers, governments, national and international organisations, as well as humanitarian organisations (Wang, A. X. et al., 2018; You et al., 2017). It helps farmers in their planning activities related to crop harvest, storage, and distribution, while also improving the efficiency of government resource allocation while also improving the decision-making process concerning the import and export of agricultural produce. In their review, Chivasa et al. (2017) allude that the dearth of information on the application of remote sensing in maize yield estimates in Africa is a catastrophe to food security monitoring and early warning systems in a continent burdened with chronic food shortages.

Several methods of predicting yield are being applied from the field to the regional scale. Field survey methods are expected to give reliable, baseline estimates, but they are costly in terms of labour and time. These methods, unfortunately, cannot be upscaled to large areas. Another method used for yield estimation is the use of crop growth models that integrate eco-physiological processes to simulate crop growth, development and yield based on soil characteristics, meteorological data and agricultural practices. However, there is a challenge in areas with scarce information on these parameters, especially in developing countries.

Remote sensing, on the other hand, has become valuable in providing data for yield prediction, especially with the high correlations between vegetation indices and green biomass

(Babar et al., 2006; Jian-qiang et al., 2009), leaf area index (LAI) (Gaso et al., 2019; Peng et al., 2019) or chlorophyll content (Guo et al., 2020; Serrano et al., 2000). Because of its quasilinear relation to the fraction of absorbed photosynthetically active radiation (APAR), NDVI is an indirect measure of above-ground biomass (Prince, 1991).

Many studies have focused on crop yield prediction using remote sensing data, like a single vegetation index (Basso et al., 2001; Kastens et al., 2005; Lai et al., 2018) and multiple vegetation indices (Bai et al., 2019; Jurečka et al., 2018; Mokhtari et al., 2018; Sulik & Long, 2016). Other studies have used satellite data from around the time of the vegetation index peak (Bai et al., 2019), with results showing high accuracy in yield prediction. The multiple linear regression (MLR) method is used to predict the yield because its variability is determined by many independent variables (Jurečka et al., 2018).

Furthermore, machine and deep learning techniques, including artificial neural networks (ANN), decision trees (DT), support vector machines (SVM), random forest (RF), Bayesian and regression, have also been applied to remote sensing data to estimate crop yield (Chlingaryan et al., 2018; Khalil & Abdullaev, 2021). Qiao et al. (2021) proposed a Spatial-Spectral-Temporal Neural Network (SSTNN), a deep learning architecture for maize and wheat crop yield prediction in China, by combining 3D convolutional and recurrent neural networks to exploit their complementarity. Specifically, the SSTNN incorporates a spatial-spectral learning module and a temporal dependency capturing module into a unified convolutional network to recognise the joint spatial-spectral-temporal representation. This architecture was compared with DT, RFR, SVM, LSTM and 2D CNN. SSTNN outperformed the other ML algorithms in predicting maize and wheat yields. Shuai & Basso (2022) developed an ML approach to forecast seasonal crop yield across fields in different US states using Landsat and high-resolution DEM data. They reported that the results were improved when they introduced the cumulative crop drought index (CDI). Khaki et al. (2021) employed YieldNet, a deep neural network technique on remote sensing data, to simultaneously predict corn and soyabean yields in the USA counties. Their results demonstrated that the proposed method accurately predicted corn and soybean yields up to four months before the harvest, with an MAE of 8.74% and 8.70% of the average yield, respectively. In another study, Mateo-Sanchis et al. (2019) combined optical vegetation indices and microwave vegetation optical depth data to estimate soyabean and corn yields, using regularised linear regression (RLR) and a nonlinear (kernel-based) regression method called kernel ridge regression

(KRR), in the Corn Belt of Midwestern United States. Schwalbert et al. (2020) also applied machine learning algorithms, multivariate OLS linear regression, Long-Short Term Memory (LSTM), Neural Networks, and random forest to estimate soyabean yield in the Rio Grande do Sul (RS) state, Brazil.

4.2. Materials and methods

The study explored the prediction of maize crop yield using mid-season and seasonal NDVI, an existing maize yield model, together with regional yield data. A healthy crop NDVI profile moves upward as crop cover increases, levels off as the crop reaches maximum biomass accumulation and begins to decline with the onset of senescence. This profile relates closely to the photosynthetic activity of a crop and is expected to relate to crop yield (Mkhabela et al. 2011). In this study, we used cumulative NDVI for up to peak growth and for the full season as predictor variables to build a regression model. The study collected NDVI data from eight farms in the 2018/2019 growing season and 13 farms in the 2019/2020 growing season, where yield data were available. The study also explored existing models based on green NDVI and LAI for the regional estimation of maize yield. In this experiment, the model is applied to simulated green NDVI data to predict maize LAI and the predicted LAI is then used as a predictor variable for maize yield estimation. The maize yield prediction model coefficients were adjusted iteratively to establish the correct parameters for the most accurate model, and its predictions were validated against provincial yield records.

5. Geospatial system development for agricultural crop water use monitoring

5.1. Introduction

5.1.1. General overview

Agriculture plays a significant role in the economic development of the country, contributing directly to household food security. It is reported that about 9% of agricultural output is produced by previously disadvantaged farmers, particularly for small- and medium-scale (emerging) farmers. Despite facing challenges like a lack of inputs and equipment resources, poor infrastructure, unsustainable farming practices, and climate change, small- and medium-scale farmers hold tremendous potential to contribute to a country's economy. Meanwhile, in Africa, demand for water, energy and food is set to increase by 40, 50 and 35% by 2030. Moreover, the agriculture sector, particularly crop production, is the largest water consumer in the world, accounting for approximately 72% of water abstractions. Simultaneously, water, a crucial finite natural resource, is facing growing strain globally because of numerous factors. These include a rising population, compounded by increased human food consumption and industrialisation, as well as the impacts of climate change. In rainfed agriculture, the impacts of climate change and water are exacerbated, imposing greater challenges to any plans to increase agricultural productivity and maintain food security (Jhariya et al, 2013). This highlights the need for a multi-disciplinary approach, involving all stakeholders, applying all available knowledge and technologies to ensure sustainable natural resource utilisation. Furthermore, small- and medium-scale farmers need to improve their productivity and contribute to improved food security through increased land and water use efficiency. Geospatial technologies have proven to offer a promising avenue for achieving this goal.

Geospatial technologies, including Geo-information science (GIS), remote sensing technologies like satellite and drone imagery, Internet of Things (IoT), together with advances in computing power, high-speed internet, machine/ deep learning (ML/ DL), and artificial intelligence (AI), make it capable of delivering value to agricultural production. Remote sensing technologies continue to evolve, providing higher spatiotemporal resolution data, producing large volumes of 'Big Data'. Remote sensing facilitates the continuous collection of spatiotemporal data regarding crop health, water requirements, and environmental conditions, which are crucial for making informed decisions in agricultural production. Geospatial platforms for crop water use have become increasingly vital in modern agriculture, particularly for optimising irrigation, assessing water conservation techniques, and enhancing water management strategies. Developed through the integration of advanced technologies such as remote sensing, geographic information systems (GIS), and machine learning, the geospatial platforms have significantly advanced the ability to monitor and manage crop water use effectively, to enhance sustainable water resource utilisation and management. One key advantage of geospatial platforms is their ability to utilise high-resolution remote sensing data to estimate evapotranspiration, which is critical for understanding crop water consumption and crop yield prediction. The integration of medium and high-resolution satellite imagery allows for precise mapping of crops and their water needs, enabling farmers to make informed decisions in irrigation and/ or applying water conservation techniques in dryland crop production (Al-Bakri et al., 2016; Calera et al., 2017).

The operational use of time series of multispectral imagery has proven effective in monitoring crop biophysical parameters throughout the growing season, thus providing accurate predictions of crop water requirements (Calera et al., 2017). For instance, platforms like WaterSmart-GIS have been developed to provide near-real-time information on soil moisture, evapotranspiration, and precipitation, which are vital for effective irrigation 2 scheduling (Zhao et al., 2022). Ramírez-Cuesta et al. (2018) introduced an ArcGIS toolbox that integrates the dual crop coefficient approach with multi-satellite imagery, allowing for more accurate irrigation scheduling and water demand estimation. The application of machine learning techniques further enhances the functionality of geospatial platforms. For example, the Hyperfidelis toolkit integrates machine learning with geospatial data to model key agricultural traits, including water use efficiency (Sagan, 2024). Furthermore, the use of Unmanned Aerial Vehicles (UAVs) in precision agriculture allows for targeted water application, thereby minimising waste and maximising crop yield (Srivastava et al., 2020).

In conclusion, the integration of remote sensing and GIS technologies into geospatial platforms has revolutionised crop water management. These platforms not only facilitate the precise estimation of crop water needs but also enable real-time monitoring of agricultural conditions, ultimately leading to improved water use efficiency and sustainability in agricultural practices.

5.1.2. Cloud computing platforms

Cloud computing platforms provide on-demand access to computing resources, such as servers, storage, databases, networking, software, and analytics, over the internet. Instead of buying, owning, and maintaining physical data centres and servers, organisations can access technology services, such as computing power, storage, and databases, on a need basis from a cloud services provider. This eliminates the need for organisations and individuals to invest in and maintain physical infrastructure, offering scalability, flexibility, and cost efficiency for a wide range of applications. For geospatial applications, cloud platforms provide powerful tools and infrastructure to store, analyse, and visualise large volumes of spatial data efficiently, while offering scalability. They are essential for working with remote sensing data, Earth observation, GIS analysis, and environmental monitoring.

Cloud computing services have several advantages and disadvantages, as described in Table 7.

Table 7: Advantages and disadvantages of cloud computing services for geospatial applications

Advantages	**Disadvantages**
Users have access to huge volumes of data without the need for obtaining and maintaining physical infrastructure, for downloading and storing them on their local systems	Geospatial datasets, including remote sensing data, may contain proprietary and sensitive information. This poses risks of data breaches and/ unauthorised access
High performance in geospatial data processing, as it allows for parallel processing and distributed computing, enabling real-time mapping	Working with datasets used, like high resolution and time series remote sensing imagery, requires reliable internet connectivity, which remains a challenge in remote regions
Vast amounts of data and processing tools have been made accessible from anywhere in the world through web interfaces or APIs	Cloud service providers charge for storage, computation and processing, and downloading of data to local systems, which usually escalates the envisaged costs

Integrates different components-remote sensing, GIS, machine learning/ deep learning and big data analytics	Most cloud platforms use proprietary APIs, formats, or data formats (e.g., Google Earth Engine, Azure Maps), making Migrating data and workflows from one provider to another can be difficult and costly, limiting flexibility and long-term control
Enables collaboration across teams and institutions through the sharing of data, models and results	The user has limited control over the processing environment, without access to root-level access
	Setting up scalable cloud platforms for geospatial applications requires knowledge of cloud infrastructure, geospatial libraries, and data pipelines, which presents a high-level technical expertise

As noted above, one of the biggest challenges of cloud computing services is the hidden costs for data storage and processing. Most of the service providers have come up with measures to manage costs. For instance, the AWS Cost Explorer and Azure Cost Management, and frameworks like FinOps have emerged to standardise financial operations in the cloud.

Cloud computing platforms that have been employed in geospatial applications are further summarised in Table 8.

Table 8: Overview of different cloud computing platforms used in geospatial applications

Platform	Remote Sensing Data Access	Scripting/API	ML/AI Support	Visualisation and Mapping	Web App Integration	Most suitable for	Cost Structure
Google Earth Engine (GEE)	Extensive built-in archive of satellite datasets (Landsat, MODIS, Sentinel, etc.)	JavaScript and Python APIs	Basic ML tools, more in ArcGIS Pro	Strong JS-based map UI; Earth Engine Apps	Limited native UI, but exportable to web apps via GCP or Firebase	Fast prototyping, planetary-scale analysis	Free for research and education
Amazon Web Services (AWS)	Open data via the AWS Open Data Registry (Landsat, Sentinel, NAIP, etc.)	REST APIs, Python, CLI	Full AI/ML via SageMaker, EC2 GPUs	Custom mapping (e.g., via Mapbox, Leaflet)	Highly flexible via EC2, Lambda, S3, etc.	Scalable processing pipelines, custom ML	Pay-as-you-go
Microsoft Planetary Computer	STAC-enabled Landsat, Sentinel, DEM, and biodiversity data	Python and STAC APIs	Azure ML, JupyterHub support	No native viewer, but works with external tools	RESTful STAC API for web apps	Open data science, biodiversity, and Python-based analysis	Free tier, pay for Azure compute
Esri ArcGIS Online	ArcGIS Living Atlas, custom imagery services	REST API, JS API, Python (ArcPy)	Basic ML tools, more in ArcGIS Pro	Strong cartography and app-building tools	ArcGIS Experience Builder, Web AppBuilder	Enterprise GIS, field apps, dashboards	Subscription-based (credits)

Sentinel Hub	Real-time Sentinel, Landsat, MODIS, PlanetScope via tile APIs	Evalscript API, WMS/ REST	Basic ML via custom evalscripts; external ML needed	EO Browser, true colour/ NDVI etc.	Supports WMS/WMTS in Leaflet/OpenLayers	Near real-time EO apps, satellite viewers	Subscription plans + free tier
Open Data Cube (ODC)	Requires setup, but works with Landsat, Sentinel, etc.	Python (xarray, dask, geopandas)	Python ML workflows	Custom front ends required	Custom integration only	National EO platforms, time-series analysis	Self-hosted or cloud-hosted
Mapbox + Cloud Backend	No built-in EO data	JavaScript, REST, Tilesets API	Via backend (AWS, GCP, etc.)	Modern, smooth vector mapping	Highly customizable UI (Mapbox GL JS)	Stylish, interactive consumer-grade apps	Free tier + usage pricing
IBM PAIRS Geoscope	Integrated spatiotemporal data fusion	REST API, web portal	AI/ML-ready via Watson	Limited public tools	Enterprise integration	Business analytics, enterprise geospatial intelligence	Enterprise pricing

5.1.3. Geospatial systems for crop (water use) monitoring

Several international, governmental, non-governmental and private initiatives are focused on addressing different aspects of crop growth monitoring and crop water use. These include:

- GEOGLAM – Crop monitoring system. It is an initiative of the Group on Earth Observation (hosted by the World Meteorological Organisation in Geneva, Switzerland), a partnership of international organisations and governments, of which South Africa is a partner. The CSIR, Agricultural Research Council (ARC) and the South African Space Agency are collaborators on the GEOGLAM crop monitoring initiative. The crop monitor is an early warning system that provides global crop (maize, wheat, rice and soybeans) condition assessments in support of Agricultural Market Information System (AIMS) monitoring activities. GEOGLAM provides coarse resolution (>500m) and regional information on the optimal crop growing conditions. Moreover, the information is compiled quarterly.
- SEN2-AGRI SYSTEM © 2018 Sen2-Agri Consortium (ESA, UCL, CESBIO, GISAT, CS)- an operational, standalone processing system that generates agricultural products from freely available satellite data (Sentinel-2 and Landsat 8) throughout the growing season. The products include monthly crop masks, cultivated crop type maps for main crops (delivered twice along the agricultural growing seasons) and weekly vegetation status products of NDVI and leaf area index (LAI), which describe the vegetation development. The system is free and open source. The system is computationally intensive, requires large amounts of training data (for crop type mapping) and generally has a coarser, regional-scale value for the products it produces. The monthly data (low temporal resolution) is not adequate for crop monitoring during the critical period of crop growth.

Moreover, a variety of platforms and systems that provide information on crop water use and yield prediction are highlighted in Table 9.

Table 9: Overview of platforms and systems for crop water use and yield prediction

Platform	Description
AquaCrop	Crop water productivity model developed by the Food and Agriculture Organisation (FAO)

	Based on a soil-plant-atmosphere continuum, it is used to assess the effects of water stress on crop yield and crop water efficiency
Dynamic Water Resources Assessment Tool (DWAT)	designed to assess land-use changes and their impact on water resources
	Uses a distributed conceptual scheme for water cycle analysis and contains sub-algorithms, such as evapotranspiration, infiltration, watershed runoff, groundwater movement, and channel routing.
ETWatch	a cloud platform that integrates surface energy balance models to estimate surface fluxes
	integrates multiple parameters and makes full use of multisource RS data to reflect the spatial and temporal characteristics of land surfaces and water-heat fluxes in the main energy balance involved in ET estimation
R Evapotranspiration package	a package that estimates actual, potential and reference ET using 17 well-known models
OpenET	developed to provide field-scale daily, monthly and annual ET, weather and vegetation conditions
	Applies ET different models to remote sensing data, and provides an ensemble ET product on Google Earth Engine.
Sen-ET	Platform that exploits machine learning techniques to combine Sentinel-2 and Sentinel-3 data for a 20m daily evapotranspiration monitoring in agricultural fields
Sen2Agri	System that generates products of cropland masks, crop type, and vegetation growth status, for agricultural monitoring based on Sentinel-2 and Landsat-8 datasets
WaPOR	Platform that uses geospatial technologies to produce, monitor and report on agricultural water productivity, efficiency and measured evapotranspiration rates over Africa and the Near East to help farmers achieve reliable agricultural yields and optimise farming irrigation systems

	Uses Google Earth computing capabilities to sift through satellite data and generate maps that indicate biomass and yield production per cubic meter of water consumed, at 30 to 250 m resolution, at 10-day intervals: Gross Biomass Water Productivity; Net Biomass Water Productivity; Actual Evapotranspiration; Above Ground Biomass Production; Transpiration; Net Primary Production; Precipitation.
eLeaf	Platform offering information on crop status throughout the crop growth stage, irrigation planning, and yield prognosis.
CapeFarmMapper	Geospatial platform that provides satellite-based information on crop type, weather patterns, and crop water use per farm, for crop monitoring and environmental management
GeoTerra Image GeoFarmer	Platform that provides monitoring of the within-field variation of crop development, crop water use

Findings from these platforms are summarised below:

- Some of them are not available in South Africa, for example, OpenET is currently available for farmers in the Western United States of America (USA), and the WaPOR 30 m products are only available to a few countries, including in East Africa (Ethiopia, Kenya, Sudan, Rwanda) and Asia (Yemen, Sri Lanka). Some products are too coarse to be able to identify in-field variability of crop water use, crop growth, and yield estimates
- Commercial platforms, like eLeaf/ FruitLook, are not available for the whole country, and they are mainly used for the vine and apple orchards.
- Some are not based on remote sensing data but utilise climate and vegetation data to estimate the crop water use and yield
- A few platforms offer the consolidation of the infield variation of crop water use and crop yield, to be able to identify gaps in productivity within crop fields.

The steps for transferring the models into the GEE are described in APPENDIX I.

6. Synthesis

6.1. Project objectives overview

The purpose of the project sought to address multi-component objectives within the agricultural and geospatial domains of South Africa:

1. Delineation of smallholder agricultural field boundaries across diverse topographies and agroecological zones;
2. Mapping of maize crop evapotranspiration (ET) using remote sensing and meteorological data for selected sites in the peripheries of Gauteng Province; and
3. Development of a geospatial tool for field-scale crop water use monitoring on a cloud computing platform.

The project began with a comprehensive literature review to assess the state of knowledge and existing methodologies related to field boundary mapping, remote sensing-based ET estimation, and geospatial tool development. The synthesis below integrates findings from all components, providing a holistic view of the technical achievements, methodological innovations, challenges encountered, and recommendations for future work.

There is a gap in the availability of digitised small crop fields, especially in Sub-Saharan Africa, where subsistence small-scale farming is prevalent. Delineating the boundaries of smallholder agricultural parcels presents inherent challenges due to the characteristics of these fields. Typically spanning only a few hectares or less, smallholder plots are often irregular in shape and lack uniformity. They usually feature mixed-cropping or intercropping systems, where multiple crop types or planting arrangements coexist within a single parcel simultaneously. In some instances, field boundaries are indistinct and may not be marked by clear physical demarcations. In South Africa, the challenges of delineating small field parcels are compounded by the diverse agricultural landscape. The commercial farms come in large, geometric fields, whereas the smallholder and subsistence farms in communal lands are characterised by very small, irregular plots. Another issue of contention when digitising smallholder fields in South Africa is the complex topography and climate. The South-West region of South Africa has a Mediterranean climate, receiving winter rainfalls, whereas the rest of the country is characterised by summer rains. This means that cropping cycles in these regions are reversed. Meanwhile, the Eastern Cape and KwaZulu-Natal are characterised by rolling hills and steep valleys, where fields often appear as patchworks on slopes. Terrain shadows and orthographic distortions can, thus, obscure field edges in these regions, unlike the flat plains of the Free State. Therefore, the techniques applied to delineate smallholder parcels across all provinces must contend with this variability, so that they are accurate in KwaZulu-Natal's fragmented, hilly mosaics of homestead fields as well as the expansive, mechanised farms of the Highveld.

The second phase of the project focused on assessing maize crop evapotranspiration (ET) in the Gauteng region. A comprehensive review of remote sensing-based ET estimation techniques was undertaken, with particular attention given to studies employing machine learning (ML) algorithms, including hybrid approaches that combine ML with conventional ET models to enhance predictive accuracy. The review examined medium spatial resolution global ET products, such as WaPOR and ECOSTRESS, with an emphasis on their applicability for monitoring maize ET. Although it has a coarser spatial resolution, the MOD16 ET product was also included in the review, as the study utilised the Penman-Monteith (PM) model, which underpins MOD16, to estimate maize water use. ET estimates were derived using meteorological data obtained from the nearest automatic weather stations operated by the South African Weather Services, in conjunction with remote sensing datasets. Additionally, ET values for the study sites were extracted from WaPOR and ECOSTRESS and compared against the modelled ET. However, the ECOSTRESS dataset contained limited observations for the study period, as documented in the findings. Despite this limitation, the comparison provided valuable insights into the discrepancies in ET magnitude across different models and products. The other part of the project involved predicting maize crop yield from remote sensing data. Literature assessment of maize yield forecasting showcased different models and their downsides. For instance, crop growth models that integrate eco-physiological processes to simulate crop growth require too many datasets for parameterisation, which is a challenge for data-scarce regions. The study then employed the relationship between NDVI and yield information acquired from farmers.

The final objective was to detail the procedure of how the models and products were transferred into a selected cloud computing platform and used to develop a geospatial tool. Available geospatial tools for monitoring crop growth and water use were appraised, including the different cloud computing platforms. Google Earth Engine (GEE) was then selected to develop the geospatial tool.

6.2. Main findings

One of the main findings of this project is that there is a need for a comprehensive method to delineate our small-scale fields, considering the complexity of the South African climate and topography. Results indicate that the unified model, particularly the residual U-Net with topographic attention, maintains high delineation accuracy across all provinces (mean IoU ≈ 0.81; boundary-F1 ≈ 0.78), outperforming or equalling province-specific counterparts except in areas of extreme relief (> 25° slope), where local fine-tuning still yields measurable gains. Failure-mode analysis attributes residual errors to persistent hill-shadow artefacts and intra-field spectral heterogeneity on steep slopes. The study concludes that a single national model, augmented with lightweight terrain-specific adapters, can satisfy operational accuracy thresholds while simplifying maintenance workflows; full retraining is warranted only in topographic outliers. The proposed methodology provides a transferable blueprint for automated smallholder-parcel mapping in other data-scarce regions characterised by sharp relief and fragmented agriculture.

The Penman-Monteith model applied in this research was extensively evaluated in different natural ecosystems in South Africa, hence, the research assessed it in maize crop water use estimation. This study reported that the total maize ET ranged minimum of 0.17 mm/ day maximum of 6.63 mm/ day at peak maize growth. This is validated through the spatiotemporal maps showing ET variation with the field, with areas with low water loss also identified. In comparison, ECOSTRESS ET ranged from 1.03 mm/ day at the end of the growing season to 6.22 mm/ day at peak growth in mid-March. It was observed that ECOSTRESS ET values were very few during the study. This was attributed to the fact that this is a proof-of-concept product for future satellite developments. WaPOR-derived ET had a low of 0.5 mm/ day, reaching a high of 5.5 mm/ day at peak maize growth. The modelled ET was very sensitive to meteorological conditions, whereas WaPOR showed a smooth trend of ET estimates, following the phenological stages of the crop. The spatial comparison of the estimated ET throughout the maize growth phases was quite similar. However, the issue of spatial resolution of the different products was highlighted. The PM modelled ET maps reveal more precisely the variation of ET within the field. For precise crop water monitoring, it is important to produce high resolution maps of crop water use.

The study finally transferred the evapotranspiration model to a cloud computing platform, Google Earth Engine, in a bid to develop a geospatial tool for monitoring crop water use. The platform's capabilities in handling large volumes of data and applying advanced analytical techniques make it an invaluable resource for enhancing agricultural water management practices. The process of developing this tool highlighted the need to develop strong capabilities in geospatial data processing. As the tool is being developed, it is valuable to consider its scalability to support larger areas and more crops. Furthermore, the tool must not be developed using the top-down approach, i.e., it must align with the needs of the end-users- farmers, researchers, or policy-makers.

6.3. Project limitations and proposals for future research

A key limitation of the project was the overly ambitious scope, which encompassed multiple distinct and technically demanding components: delineation of smallholder field boundaries, estimation and spatial mapping of maize crop water use, crop yield prediction, and the development of an integrated geospatial decision-support tool. The inclusion of these heterogeneous objectives introduced significant complexity and hindered the ability to conduct in-depth analysis within each domain. Consequently, the work remained exploratory rather than comprehensive, limiting the robustness of individual components. For instance, while the development of a regional-scale evapotranspiration monitoring framework is relatively tractable using standard remote sensing and modelling approaches, the creation of a dynamic, farm-level interactive platform capable of delivering parcel-specific information necessitates advanced geospatial programming and interface development; requirements that extend beyond routine script-based workflows.

Based on the above challenges and findings of this project, we recommend to the WRC that:

1. The developed methodology for digitising smallholder fields should be tested across a wider range of agroecological zones and farming systems in South Africa. This will help to assess its adaptability and accuracy under varying field shapes, cropping patterns, and topographic conditions.
2. Given the scarcity of long-term, in-situ evapotranspiration measurements in agricultural regions, there is a critical need to establish a network of ET monitoring stations. These stations should provide publicly accessible data to support the calibration and validation of remote sensing-based ET models and products.
3. While most research on crop ET focuses on irrigated systems due to their role in irrigation scheduling, it is equally important to understand ET dynamics in rainfed cropping systems.

Improved insights into water use under rainfed conditions can inform strategies for enhancing water productivity, especially in semi-arid areas.

4. The foundational framework for a geospatial tool to monitor field-scale crop water use has been established. The next phase should focus on integrating individual field data and ensuring the tool meets the needs of its intended users—whether farmers, researchers, or policymakers—through co-design and iterative feedback.
5. Many global ET products are not suitable for smallholder fields due to coarse spatial resolution. Efforts should be made to secure access to higher-resolution ET data—either through new satellite missions, partnerships, or expanded availability of pilot products such as WaPOR 20 m ET—to enable more accurate monitoring and decision-making at the field level.

References

Abid, N., Ben Jaafar, A., Bargaoui, Z., & Mannaerts, C. M. (2024). Assessment of long-term MOD16 and LSA SAF actual evapotranspiration using Budyko curve. *Remote Sensing Applications: Society and Environment, 34*, 101166. 10.1016/j.rsase.2024.101166

Aguilar, A. L., Flores, H., Crespo, G., Marín, M. I., Campos, I., & Calera, A. (2018). Performance Assessment of MOD16 in Evapotranspiration Evaluation in Northwestern Mexico. *Water, 10*(7)10.3390/w10070901

Alemohammad, S. H., Fang, B., Konings, A. G., Aires, F., Green, J. K., Kolassa, J., Miralles, D., Prigent, C., & Gentine, P. (2017). Water, Energy, and Carbon with Artificial Neural Networks (WECANN): a statistically based estimate of global surface turbulent fluxes and gross primary productivity using solar-induced fluorescence. *Biogeosciences, 14*(18), 4101–4124.

Ali, S. M., & Acquaye, A. (2024). An examination of Water-Energy-Food nexus: From theory to application. *Renewable and Sustainable Energy Reviews, 202*, 114669.

Allen, R. G., Tasumi, M., Morse, A., Trezza, R., Wright, J. L., Bastiaanssen, W., Kramber, W., Lorite, I., & Robison, C. W. (2007). Satellite-based energy balance for mapping evapotranspiration with internalised calibration (METRIC)—Applications. *Journal of Irrigation and Drainage Engineering, 133*(4), 395–406.

Ambrosio, L., Iglesias, L., Marín, C., & Deffense, N. (2023). Integration of remote sensing data into national statistical office sampling designs for agriculture. *Statistical Journal of the IAOS, 39*(2), 473–489.

Andrade, N., Sandwiches, L., Zeilhofer, P., João, G., Gutieres, C. B., & Carlo, R. D. (2023). Different spatial and temporal arrangements for validating the latent heat flux obtained using the MOD16 product in a forest in the Western Amazon. *Int.J.Hydro, 7*, 18–25.

Antonopoulos, V. Z., & Antonopoulos, A. V. (2017). Daily reference evapotranspiration estimates by artificial neural networks technique and empirical equations using limited input climate variables. *Computers and Electronics in Agriculture, 132*, 86–96.

AR, I. W. (2014). Climate change 2014 impacts, adaptation, and vulnerability. *Contribution of Working Group II to the Fifth Assessment Report of the Intergovernmental Panel on Climate Change,* Babar, M. A., Van Ginkel, M., Klatt, A. R., Prasad, B., & Reynolds, M. P. (2006). The potential of using spectral reflectance indices to estimate yield in wheat grown under reduced irrigation. *Euphytica, 150*, 155–172.

Bai, T., Zhang, N., Mercatoris, B., & Chen, Y. (2019). Jujube yield prediction method combining Landsat 8 Vegetation Index and the phenological length. *Computers and Electronics in Agriculture, 162*, 1011–1027.

Basso, B., Ritchie, J. T., Pierce, F. J., Braga, R. P., & Jones, J. W. (2001). Spatial validation of crop models for precision agriculture. *Agricultural Systems, 68*(2), 97–112.

Bastiaanssen, W., Cheema, M., Immerzeel, W. W., Miltenburg, I. J., & Pelgrum, H. (2012). Surface energy balance and actual evapotranspiration of the transboundary Indus Basin estimated from satellite measurements and the ETLook model. *Water Resources Research, 48*(11)

Blaschke, T., Feizizadeh, B., & Hölbling, D. (2014a). Object-based image analysis and digital terrain analysis for locating landslides in the Urmia Lake Basin, Iran. *IEEE Journal of Selected Topics in Applied Earth Observations and Remote Sensing, 7*(12), 4806–4817.

Blaschke, T., Hay, G. J., Kelly, M., Lang, S., Hofmann, P., Addink, E., Feitosa, R. Q., Van der Meer, F., Van der Werff, H., & Van Coillie, F. (2014b). Geographic object-based image analysis–towards a new paradigm. *ISPRS Journal of Photogrammetry and Remote Sensing, 87*, 180–191.

Blatchford, M. L., Mannaerts, C. M., Njuki, S. M., Nouri, H., Zeng, Y., Pelgrum, H., Wonink, S., & Karimi, P. (2020). Evaluation of WaPOR V2 evapotranspiration products across Africa. *Hydrological Processes, 34*(15), 3200–3221.

Born, L., Chirinda, N., Mabaya, E., Afun-Ogidan, O. D., Girvetz, E. H., Jarvis, A., & Kropff, W. (2021). Digital Agriculture Profile: South Africa.

Bosch, J., Olsson, H. H., & Crnkovic, I. (2021). Engineering ai systems: A research agenda. *Artificial Intelligence Paradigms for Smart Cyber-Physical Systems*, 1–19.

Bowen, I. S. (1926). The ratio of heat losses by conduction and by evaporation from any water surface. *Physical Review, 27*(6), 779.

Brutsaert, W. (2023). *Hydrology*. Cambridge University Press.

Cai, X., Molden, D., Mainuddin, M., Sharma, B., Ahmad, M., & Karimi, P. (2011). Producing more food with less water in a changing world: assessment of water productivity in 10 major river basins. *Water International, 36*(1), 42–62.

Chen, X., Yu, L., Cui, N., Cai, H., Jiang, X., Liu, C., Shu, Z., & Wu, Z. (2022). Modeling maize evapotranspiration using three types of canopy resistance models coupled with single-source and dual-source hypotheses—A comparative study in a semi-humid and drought-prone region. *Journal of Hydrology, 614*, 128638. 10.1016/j.jhydrol.2022.128638

Chivasa, W., Mutanga, O., & Biradar, C. (2017). Application of remote sensing in estimating maize grain yield in heterogeneous African agricultural landscapes: a review. *International Journal of Remote Sensing, 38*(23), 6816–6845.

Chlingaryan, A., Sukkarieh, S., & Whelan, B. (2018). Machine learning approaches for crop yield prediction and nitrogen status estimation in precision agriculture: A review. *Computers and Electronics in Agriculture, 151*, 61–69.

Cleugh, H. A., Leuning, R., Mu, Q., & Running, S. W. (2007). Regional evaporation estimates from flux tower and MODIS satellite data. *Remote Sensing of Environment, 106*(3), 285–304.

Cogill, L. S., Toucher, M., Wolski, P., Esler, K. J., & Rebelo, A. J.Evaluating the Performance of Satellite-Derived Evapotranspiration Products Across Varying Bioclimates. *Available at SSRN 5100352,*

Costa-Filho, E., Chávez, J. L., & Zhang, H. (2024). Mapping Maize Evapotranspiration with Two-Source Land Surface Energy Balance Approaches and Multiscale Remote Sensing Imagery Pixel Sizes: Accuracy Determination toward a Sustainable Irrigated Agriculture. *Sustainability, 16*(11)10.3390/su16114850

Dayoub, E. B., Tóth, Z., & Anda, A. (2024). A preliminary observation in evaluating maize evapotranspiration and plant features under meteorological variables and biochar effect. *Archives of Agronomy and Soil Science, 70*(1), 1–18. 10.1080/03650340.2024.2398039

Djaman, K., O'Neill, M., Owen, C. K., Smeal, D., Koudahe, K., West, M., Allen, S., Lombard, K., & Irmak, S. (2018). Crop Evapotranspiration, Irrigation Water Requirement and Water Productivity of Maize from Meteorological Data under Semiarid Climate. *Water, 10*(4)10.3390/w10040405

Dzikiti, S., Jovanovic, N. Z., Bugan, R. D., Ramoelo, A., Majozi, N. P., Nickless, A., Cho, M. A., Le Maitre, D. C., Ntshidi, Z., & Pienaar, H. H. (2019). Comparison of two remote sensing models for estimating evapotranspiration: algorithm evaluation and application in seasonally arid ecosystems in South Africa. *Journal of Arid Land, 11*(4), 495–512.

Fakhar, M. S., & Kaviani, A. (2024). Estimation of water consumption volume and water efficiency in irrigated and rainfed agriculture based on the WaPOR database in Iran. *Journal of Water and Climate Change, 15*(6), 2731–2752. 10.2166/wcc.2024.655

Fan, J., Ma, X., Wu, L., Zhang, F., Yu, X., & Zeng, W. (2019). Light Gradient Boosting Machine: An efficient soft computing model for estimating daily reference evapotranspiration with local and external meteorological data. *Agricultural Water Management, 225*, 105758.

Ferroukhi, R., Nagpal, D., López-Peña, Á, Hodges, T., Mohtar, R., Daher, B., Mohtar, S., & Keulertz, M. (2015). *Renewable Energy in the Water, Energy & Food Nexus*

Field, C. B., & Barros, V. R. (2014). *Climate change 2014–Impacts, adaptation and vulnerability: Regional aspects*. Cambridge University Press.

Fisher, J. B., Lee, B., Purdy, A. J., Halverson, G. H., Dohlen, M. B., Cawse-Nicholson, K., Wang, A., Anderson, R. G., Aragon, B., & Arain, M. A. (2020). ECOSTRESS: NASA's next generation mission to measure evapotranspiration from the international space station. *Water Resources Research, 56*(4), e2019WR026058.

Fisher, J. B., Tu, K. P., & Baldocchi, D. (2008). Global estimates of the land–atmosphere water flux based on monthly AVHRR and ISLSCP-II data, validated at 16 FLUXNET sites. *Remote Sensing of Environment, 112*(3), 901–919.

Fritz, S., See, L., Bayas, J. C. L., Waldner, F., Jacques, D., Becker-Reshef, I., Whitcraft, A., Baruth, B., Bonifacio, R., Crutchfield, J., Rembold, F., Rojas, O., Schucknecht, A., Van der Velde, M., Verdin, J., Wu, B., Yan, N., You, L., Gilliams, S., . . . McCallum, I. (2019). A comparison of global agricultural monitoring systems and current gaps. *Agricultural Systems, 168*, 258–272. 10.1016/j.agsy.2018.05.010

Gaso, D. V., Berger, A. G., & Ciganda, V. S. (2019). Predicting wheat grain yield and spatial variability at field scale using a simple regression or a crop model in conjunction with Landsat images. *Computers and Electronics in Agriculture, 159*, 75–83.

Gebler, S., Hendricks Franssen, H., Pütz, T., Post, H., Schmidt, M., & Vereecken, H. (2015). Actual evapotranspiration and precipitation measured by lysimeters: a comparison with eddy covariance and tipping bucket. *Hydrology and Earth System Sciences, 19*(5), 2145–2161.

Ghilain, N., Arboleda, A., & Gellens-Meulenberghs, F. (2011). Evapotranspiration modelling at large scale using near-real time MSG SEVIRI derived data. *Hydrology and Earth System Sciences, 15*, 771–786.

Ghorbanzadeh, O., Crivellari, A., Ghamisi, P., Shahabi, H., & Blaschke, T. (2021). A comprehensive transferability evaluation of U-Net and ResU-Net for landslide detection from Sentinel-2 data (case study areas from Taiwan, China, and Japan). *Scientific Reports, 11*(1), 14629.

Gibson, L. A., Jarmain, C., Su, Z., & Eckardt, F. E. (2013). Review: Estimating evapotranspiration using remote sensing and the Surface Energy Balance System–A South African perspective. *Water SA, 39*(4), 477–484.

Guo, Y., Wang, H., Wu, Z., Wang, S., Sun, H., Senthilnath, J., Wang, J., Robin Bryant, C., & Fu, Y. (2020). Modified red blue vegetation index for chlorophyll estimation and yield prediction of maize from visible images captured by UAV. *Sensors, 20*(18), 5055.

Hargreaves, G. H., & Samani, Z. A. (1982). Estimating potential evapotranspiration. *Journal of the Irrigation and Drainage Division, 108*(3), 225–230.

He, K., Gkioxari, G., Dollár, P., & Girshick, R. (2017). Mask r-cnn. Paper presented at the *Proceedings of the IEEE International Conference on Computer Vision,* 2961–2969.

Hillel, D. (1982). *Introduction to soil physics*. Academic press New York.

Hu, X., Shi, L., Lin, G., & Lin, L. (2021). Comparison of physical-based, data-driven and hybrid modeling approaches for evapotranspiration estimation. *Journal of Hydrology, 601*, 126592. 10.1016/j.jhydrol.2021.126592

Huntington, H. P., Schmidt, J. I., Loring, P. A., Whitney, E., Aggarwal, S., Byrd, A. G., Dev, S., Dotson, A. D., Huang, D., & Johnson, B. (2021). Applying the food–energy–water nexus concept at the local scale. *Nature Sustainability, 4*(8), 672–679.

Jiang, L., & Islam, S. (2001). Estimation of surface evaporation map over southern Great Plains using remote sensing data. *Water Resources Research, 37*(2), 329–340.

Jian-qiang, R., Xing-ren, L., Zhong-xin, C., Qing-bo, Z., & Hua-jun, T. (2009). Prediction of winter wheat yield based on crop biomass estimation at regional scale. *Yingyong Shengtai Xuebao, 20*(4)

Jurečka, F., Lukas, V., Hlavinka, P., Semerádová, D., Žalud, Z., & Trnka, M. (2018). Estimating crop yields at the field level using Landsat and MODIS products. *Acta Universitatis Agriculturae Et Silviculturae Mendelianae Brunensis, 66*(5)

Kastens, J. H., Kastens, T. L., Kastens, D. L., Price, K. P., Martinko, E. A., & Lee, R. (2005). Image masking for crop yield forecasting using AVHRR NDVI time series imagery. *Remote Sensing of Environment, 99*(3), 341–356.

Khaki, S., Pham, H., & Wang, L. (2021). Simultaneous corn and soybean yield prediction from remote sensing data using deep transfer learning. *Scientific Reports, 11*(1), 11132. 10.1038/s41598-021-89779-z

Khalil, Z. H., & Abdullaev, S. M. (2021). Neural network for grain yield predicting based multispectral satellite imagery: comparative study. *Procedia Computer Science, 186*, 269–278.

Kim, H. W., Hwang, K., Mu, Q., Lee, S. O., & Choi, M. (2012). Validation of MODIS 16 global terrestrial evapotranspiration products in various climates and land cover types in Asia. *KSCE Journal of Civil Engineering, 16*(2), 229–238.

Kirillov, A., Mintun, E., Ravi, N., Mao, H., Rolland, C., Gustafson, L., Xiao, T., Whitehead, S., Berg, A. C., & Lo, W. (2023). Segment anything. Paper presented at the *Proceedings of the IEEE/CVF International Conference on Computer Vision,* 4015–4026.

Lai, Y., Pringle, M. J., Kopittke, P. M., Menzies, N. W., Orton, T. G., & Dang, Y. P. (2018). An empirical model for prediction of wheat yield, using time-integrated Landsat NDVI. *International Journal of Applied Earth Observation and Geoinformation, 72*, 99–108.

Leuning, R., Denmead, O. T., Lang, A., & Ohtaki, E. (1982). Effects of heat and water vapor transport on eddy covariance measurement of CO 2 fluxes. *Boundary-Layer Meteorology, 23*(2), 209–222.

Liang, L., Feng, Y., Wu, J., He, X., Liang, S., Jiang, X., de Oliveira, G., Qiu, J., & Zeng, Z. (2022). Evaluation of ECOSTRESS evapotranspiration estimates over heterogeneous landscapes in the continental US. *Journal of Hydrology, 613*, 128470. 10.1016/j.jhydrol.2022.128470

Liu, N., Oishi, A. C., Miniat, C. F., & Bolstad, P. (2021). An evaluation of ECOSTRESS products of a temperate montane humid forest in a complex terrain environment. *Remote Sensing of Environment, 265*, 112662.

Liu, Y. Y., van Dijk, A. I. J. M., McCabe, M. F., Evans, J. P., & de Jeu, R. A. M. (2013). Global vegetation biomass change (1988-2008) and attribution to environmental and human drivers. *Global Ecology and Biogeography, 22*(6), 692–705. 10.1111/geb.12024

Liu, Y., Wang, A., Li, B., Šimůnek, J., & Liao, R. (2024). Combining mathematical models and machine learning algorithms to predict the future regional-scale actual transpiration by maize. *Agricultural Water Management, 303*, 109056. 10.1016/j.agwat.2024.109056

Liu, Z., Tan, Y., He, Q., & Xiao, Y. (2021). SwinNet: Swin transformer drives edge-aware RGB-D and RGB-T salient object detection. *IEEE Transactions on Circuits and Systems for Video Technology, 32*(7), 4486–4497.

M. Lavreniuk, L. Shumilo, & A. Lavreniuk. (2023). Generative Adversarial Networks for the Satellite Data Super Resolution Based on the Transformers with Attention. Paper presented at the *IGARSS 2023 - 2023 IEEE International Geoscience and Remote Sensing Symposium,* 6294–6297. 10.1109/IGARSS52108.2023.10281826

Ma, L., Yan, Z., Li, M., Liu, T., Tan, L., Wang, X., He, W., Wang, R., He, G., & Lu, H. (2024). Deep Learning Meets OBIA: Tasks, Challenges, Strategies, and Perspectives. *arXiv Preprint arXiv:2408.01607,*

Majozi, N. P., Mannaerts, C. M., Ramoelo, A., Mathieu, R., Mudau, A. E., & Verhoef, W. (2017). An intercomparison of satellite-based daily evapotranspiration estimates under different eco-climatic regions in South Africa. *Remote Sensing, 9*(4), 307.

Mallick, K., Jarvis, A., Fisher, J. B., Tu, K. P., Boegh, E., & Niyogi, D. (2013). Latent Heat Flux and Canopy Conductance Based on Penman–Monteith, Priestley–Taylor Equation, and Bouchet's Complementary Hypothesis. *Journal of Hydrometeorology, 14*(2), 419–442. 10.1175/JHM-D-12-0117.1

Mangani, R., Tesfamariam, E. H., Engelbrecht, C. J., Bellocchi, G., Hassen, A., & Mangani, T. (2019). Potential impacts of extreme weather events in main maize (Zea mays L.) producing areas of South Africa under rainfed conditions. *Regional Environmental Change, 19*, 1441–1452.

Manyari, Y., Kharrou, M. H., Simonneaux, V., Khabba, S., Jarlan, L., Ezzahar, J., & Er-Raki, S.Accuracy Assessment of Remote Sensing-Derived Evapotranspiration Products Against Eddy Covariance Measurements in Tensift Al-Haouz Semi-Arid Region, Morocco.

Mateo-Sanchis, A., Piles, M., Muñoz-Marí, J., Adsuara, J. E., Pérez-Suay, A., & Camps-Valls, G. (2019). Synergistic integration of optical and microwave satellite data for crop yield estimation. *Remote Sensing of Environment, 234*, 111460. 10.1016/j.rse.2019.111460

Meijninger, W., Beyrich, F., Lüdi, A., Kohsiek, W., & Bruin, H. D. (2006). Scintillometer-based turbulent fluxes of sensible and latent heat over a heterogeneous land surface–a contribution to LITFASS-2003. *Boundary-Layer Meteorology, 121*(1), 89–110.

Meng, L., Zhong, P., Lingxiao, H., Zhaoliang, L. I., Sibo, D., & Ronglin, T. (2023). Validation of crop evapotranspiration products based on eddy-covariance flux observations. *National Remote Sensing Bulletin, 27*(5), 1238–1253.

Miralles, D. G., De Jeu, R., Gash, J. H., Holmes, T., & Dolman, A. J. (2011). An application of GLEAM to estimating global evaporation. *Hydrology and Earth System Sciences Discussions, 8*(1), 1–27.

Mokhtari, A., Noory, H., & Vazifedoust, M. (2018). Improving crop yield estimation by assimilating LAI and inputting satellite-based surface incoming solar radiation into SWAP model. *Agricultural and Forest Meteorology, 250*, 159–170.

Monteith, J. L. (1965). Evaporation and environment. Paper presented at the *Symp. Soc. Exp. Biol, , 19*(205-23) 4.

Monteith, J. L. (1981). Evaporation and surface temperature. *Quarterly Journal of the Royal Meteorological Society, 107*(451), 1–27.

Monteith, J. L., & Unsworth, M. H. (2013). In Monteith J. L., Unsworth M. H.(Eds.), *Chapter 16 - Micrometeorology: (i) Turbulent Transfer, Profiles, and Fluxes*. Academic Press. 10.1016/B978-0-12-386910-4.00016-0

Mperejekumana, P., Shen, L., Zhong, S., Gaballah, M. S., & Muhirwa, F. (2024). Exploring the potential of decentralized renewable energy conversion systems on water, energy, and food security in africa. *Energy Conversion and Management, 315*, 118757. 10.1016/j.enconman.2024.118757

Mu, Q., Heinsch, F. A., Zhao, M., & Running, S. W. (2007). Development of a global evapotranspiration algorithm based on MODIS and global meteorology data. *Remote Sensing of Environment, 111*(4), 519–536.

Mu, Q., Zhao, M., & Running, S. W. (2011). Improvements to a MODIS global terrestrial evapotranspiration algorithm. *Remote Sensing of Environment, 115*(8), 1781–1800.

Munyati, C., Balzter, H., & Economon, E. (2020). Correlating Sentinel-2 MSI-derived vegetation indices with in-situ reflectance and tissue macronutrients in savannah grass. *International Journal of Remote Sensing, 41*(10), 3820–3844.

Nagy, A., Kiss, N. É, Buday-Bódi, E., Magyar, T., Cavazza, F., Gentile, S. L., Abdullah, H., Tamás, J., & Fehér, Z. Z. (2024). Precision Estimation of Crop Coefficient for Maize Cultivation Using High-Resolution Satellite Imagery to Enhance Evapotranspiration Assessment in Agriculture. *Plants, 13*(9), 1212.

Nhamo, L., Mabhaudhi, T., & Modi, A. T. (2019). Preparedness or repeated short-term relief aid? Building drought resilience through early warning in southern Africa. *Water Sa, 45*(1), 75–85.

Nhamo, L., Mabhaudhi, T., Mpandeli, S., Dickens, C., Nhemachena, C., Senzanje, A., Naidoo, D., Liphadzi, S., & Modi, A. T. (2020). An integrative analytical model for the water-energy-food nexus: South Africa case study. *Environmental Science & Policy, 109*, 15–24.

Palmer, A., Weideman, C., Hawkins, H., Rajah, P., Marandure, T., Mapiye, C., Wu, L., Gwate, O., & Bennett, J. (2023). An evaluation of three evapotranspiration models to determine water fluxes over hillslopes encroached by invasive alien plants in Eastern Cape Province, South Africa. *Water SA, 49*(3), 211–219.

Peng, Y., Zhu, T., Li, Y., Dai, C., Fang, S., Gong, Y., Wu, X., Zhu, R., & Liu, K. (2019). Remote prediction of yield based on LAI estimation in oilseed rape under different planting methods and nitrogen fertilizer applications. *Agricultural and Forest Meteorology, 271*, 116–125.

Penman, H. L. (1948a). Natural evaporation from open water, bare soil and grass. *Proceedings of the Royal Society of London.Series A.Mathematical and Physical Sciences, 193*(1032), 120–145.

Penman, H. L. (1948b). Natural evaporation from open water, bare soil and grass. *Proceedings of the Royal Society of London.Series A.Mathematical and Physical Sciences, 193*(1032), 120–145.

Persello, C., Tolpekin, V. A., Bergado, J. R., & De By, R. A. (2019). Delineation of agricultural fields in smallholder farms from satellite images using fully convolutional networks and combinatorial grouping. *Remote Sensing of Environment, 231*, 111253.

Priestley, C. H. B., & Taylor, R. J. (1972). On the Assessment of Surface Heat Flux and Evaporation Using Large-Scale Parameters. *Monthly Weather Review, 100*(2), 81–92. 10.1175/1520-0493(1972)100

Prince, S. D. (1991). A model of regional primary production for use with coarse resolution satellite data. *International Journal of Remote Sensing, 12*(6), 1313–1330.

Qiao, M., He, X., Cheng, X., Li, P., Luo, H., Zhang, L., & Tian, Z. (2021). Crop yield prediction from multi-spectral, multi-temporal remotely sensed imagery using recurrent 3D convolutional neural networks. *International Journal of Applied Earth Observation and Geoinformation, 102*, 102436. 10.1016/j.jag.2021.102436

R. Guzinski, H. Nieto, J. M. Sánchez, R. López-Urrea, D. M. Boujnah, & G. Boulet. (2021). Utility of Copernicus-Based Inputs for Actual Evapotranspiration Modeling in Support of Sustainable Water Use in Agriculture. *IEEE Journal of Selected Topics in Applied Earth Observations and Remote Sensing, 14*, 11466–11484. 10.1109/JSTARS.2021.3122573

Ramoelo, A., Majozi, N., Mathieu, R., Jovanovic, N., Nickless, A., & Dzikiti, S. (2014). Validation of global evapotranspiration product (MOD16) using flux tower data in the African savanna, South Africa. *Remote Sensing, 6*(8), 7406–7423.

Ren, Z., Che, T., Xu, F., Zhang, Y., Tan, J., Wang, J., & Wang, W. (2025). Validation of Remotely Sensed Evapotranspiration Products Using Optical-Microwave Scintillometer Flux Measurements Over the Heterogeneous Surfaces. *IEEE Journal of Selected Topics in Applied Earth Observations and Remote Sensing,*

Rodell, M., McWilliams, E. B., Famiglietti, J. S., Beaudoing, H. K., & Nigro, J. (2011). Estimating evapotranspiration using an observation based terrestrial water budget. *Hydrological Processes, 25*(26), 4082–4092.

Ronneberger, O., Fischer, P., & Brox, T. (2015). U-net: Convolutional networks for biomedical image segmentation. Paper presented at the *Medical Image Computing and Computer-Assisted intervention–MICCAI 2015: 18th International Conference, Munich, Germany, October 5-9, 2015, Proceedings, Part III 18,* 234–241.

Schwalbert, R. A., Amado, T., Corassa, G., Pott, L. P., Prasad, P. V., & Ciampitti, I. A. (2020). Satellite-based soybean yield forecast: Integrating machine learning and weather data for improving crop yield prediction in southern Brazil. *Agricultural and Forest Meteorology, 284*, 107886.

Serrano, L., Gamon, J. A., & Peñuelas, J. (2000). Estimation of canopy photosynthetic and nonphotosynthetic components from spectral transmittance. *Ecology, 81*(11), 3149–3162.

Shackleton, C. M., Blair, A., De Lacy, P., Kaoma, H., Mugwagwa, N., Dalu, M. T., & Walton, W. (2018). How important is green infrastructure in small and medium-sized towns? Lessons from South Africa. *Landscape and Urban Planning, 180*, 273–281. 10.1016/j.landurbplan.2016.12.007

Shao, G., Han, W., Zhang, H., Zhang, L., Wang, Y., & Zhang, Y. (2023). Prediction of maize crop coefficient from UAV multisensor remote sensing using machine learning methods. *Agricultural Water Management, 276*, 108064. 10.1016/j.agwat.2022.108064

Shuai, G., & Basso, B. (2022). Subfield maize yield prediction improves when in-season crop water deficit is included in remote sensing imagery-based models. *Remote Sensing of Environment, 272*, 112938. 10.1016/j.rse.2022.112938

Stull, R. B. (2012). *An introduction to boundary layer meteorology*. Springer Science & Business Media.

Sulik, J. J., & Long, D. S. (2016). Spectral considerations for modeling yield of canola. *Remote Sensing of Environment, 184*, 161–174.

Sun, D., Zhang, H., Qi, Y., Ren, Y., Zhang, Z., Li, X., Lv, Y., & Cheng, M. (2025). A Comparative Analysis of Different Algorithms for Estimating Evapotranspiration with Limited Observation Variables: A Case Study in Beijing, China. *Remote Sensing, 17*(4)10.3390/rs17040636

Sun, K., Zhao, Y., Jiang, B., Cheng, T., Xiao, B., Liu, D., Mu, Y., Wang, X., Liu, W., & Wang, J. (2019). High-resolution representations for labeling pixels and regions. *arXiv Preprint arXiv:1904.04514,*

Sun, L., Liang, S., Yuan, W., & Chen, Z. (2013). Improving a Penman–Monteith evapotranspiration model by incorporating soil moisture control on soil evaporation in semiarid areas. *International Journal of Digital Earth,* (ahead-of-print), 1–23.

Tang, D., Feng, Y., Gong, D., Hao, W., & Cui, N. (2018). Evaluation of artificial intelligence models for actual crop evapotranspiration modeling in mulched and non-mulched maize croplands. *Computers and Electronics in Agriculture, 152*, 375–384.

Tariq, A., Yan, J., Gagnon, A. S., Riaz Khan, M., & Mumtaz, F. (2023). Mapping of cropland, cropping patterns and crop types by combining optical remote sensing images with decision tree classifier and random forest. *Geo-Spatial Information Science, 26*(3), 302–320.

Tiruye, A., Ditthakit, P., Linh, N. T. T., Wipulanusat, W., Weesakul, U., & Thongkao, S. (2024). Comparing WaPOR and ERA5-Land: Innovative Estimations of Precipitation and Evapotranspiration in the Tana Basin, Ethiopia. *Earth Systems and Environment, 8*(4), 1225–1246.

Villarreal-Guerrero, F., Kacira, M., Fitz-Rodríguez, E., Kubota, C., Giacomelli, G. A., Linker, R., & Arbel, A. (2012). *Comparison of three evapotranspiration models for a greenhouse cooling strategy with natural ventilation and variable high pressure fogging*10.1016/j.scienta.2011.10.016

Waldner, F., & Diakogiannis, F. I. (2020). Deep learning on edge: Extracting field boundaries from satellite images with a convolutional neural network. *Remote Sensing of Environment, 245*, 111741. 10.1016/j.rse.2020.111741

Walker, N. J., & Schulze, R. E. (2008). Climate change impacts on agro-ecosystem sustainability across three climate regions in the maize belt of South Africa. *Agriculture, Ecosystems & Environment, 124*(1-2), 114–124.

Wang, A. X., Tran, C., Desai, N., Lobell, D., & Ermon, S. (2018). Deep transfer learning for crop yield prediction with remote sensing data. Paper presented at the *Proceedings of the 1st ACM SIGCAS Conference on Computing and Sustainable Societies,* 1–5.

Wang, D., & Cai, X. (2008). Robust data assimilation in hydrological modeling – A comparison of Kalman and H-infinity filters. *Advances in Water Resources, 31*(3), 455–472. 10.1016/j.advwatres.2007.10.001

Wang, S., Waldner, F., & Lobell, D. B. (2022). Unlocking Large-Scale Crop Field Delineation in Smallholder Farming Systems with Transfer Learning and Weak Supervision. *Remote Sensing, 14*(22)10.3390/rs14225738

Wang, X., Lei, H., Li, J., Huo, Z., Zhang, Y., & Qu, Y. (2023). Estimating evapotranspiration and yield of wheat and maize croplands through a remote sensing-based model. *Agricultural Water Management, 282*, 108294. 10.1016/j.agwat.2023.108294

Ward, A. D., & Trimble, S. W. (2003). *Environmental hydrology*. Crc Press.

Watkins, B., & Van Niekerk, A. (2019). Automating field boundary delineation with multi-temporal Sentinel-2 imagery. *Computers and Electronics in Agriculture, 167*, 105078.

Wu, J., Feng, Y., Liang, L., He, X., & Zeng, Z. (2022). Assessing evapotranspiration observed from ECOSTRESS using flux measurements in agroecosystems. *Agricultural Water Management, 269*, 107706. 10.1016/j.agwat.2022.107706

Xiong, J., Thenkabail, P. S., Tilton, J. C., Gumma, M. K., Teluguntla, P., Oliphant, A., Congalton, R. G., Yadav, K., & Gorelick, N. (2017). Nominal 30-m cropland extent map of continental Africa by integrating pixel-based and object-based algorithms using Sentinel-2 and Landsat-8 data on Google Earth Engine. *Remote Sensing, 9*(10), 1065.

Xu, T., Guo, Z., Liu, S., He, X., Meng, Y., Xu, Z., Xia, Y., Xiao, J., Zhang, Y., & Ma, Y. (2018). Evaluating different machine learning methods for upscaling evapotranspiration from flux towers to the regional scale. *Journal of Geophysical Research: Atmospheres, 123*(16), 8674–8690.

Yan, L., & Roy, D. P. (2016). Conterminous United States crop field size quantification from multi-temporal Landsat data. *Remote Sensing of Environment, 172*, 67–86.

Yan, L., & Roy, D. P. (2020). Spatially and temporally complete Landsat reflectance time series modelling: The fill-and-fit approach. *Remote Sensing of Environment, 241*, 111718. 10.1016/j.rse.2020.111718

You, J., Li, X., Low, M., Lobell, D., & Ermon, S. (2017). Deep gaussian process for crop yield prediction based on remote sensing data. Paper presented at the *Proceedings of the AAAI Conference on Artificial Intelligence, , 31*(1)

Zeng, Z., Piao, S., Lin, X., Yin, G., Peng, S., Ciais, P., & Myneni, R. B. (2012). Global evapotranspiration over the past three decades: estimation based on the water balance equation combined with empirical models. *Environmental Research Letters, 7*(1), 014026.

Zhang, H., Liu, M., Wang, Y., Shang, J., Liu, X., Li, B., Song, A., & Li, Q. (2021). Automated delineation of agricultural field boundaries from Sentinel-2 images using recurrent residual U-Net. *International Journal of Applied Earth Observation and Geoinformation, 105*, 102557.

Zhang, Y., Han, W., Zhang, H., Niu, X., & Shao, G. (2023). Evaluating maize evapotranspiration using high-resolution UAV-based imagery and FAO-56 dual crop coefficient approach. *Agricultural Water Management, 275*, 108004. 10.1016/j.agwat.2022.108004

Zhao, W. L., Xiong, Y. J., Paw, U., Tha, K., Gentine, P., Chen, B., & Qiu, G. Y. (2019). Uncertainty caused by resistances in evapotranspiration. *Hydrology and Earth System Sciences Discussions,* , 1–41.

Zheng, H., Bian, Q., Yin, Y., Ying, H., Yang, Q., & Cui, Z. (2018). Closing water productivity gaps to achieve food and water security for a global maize supply. *Scientific Reports, 8*(1), 14762.

Zhu, W., Tian, S., Wei, J., Jia, S., & Song, Z. (2022). Multi-scale evaluation of global evapotranspiration products derived from remote sensing images: Accuracy and uncertainty. *Journal of Hydrology, 611*, 127982. 10.1016/j.jhydrol.2022.127982

Zimba, H., Coenders-Gerrits, M., Banda, K., Hulsman, P., van de Giesen, N., Nyambe, I., & Savenije, H. (2022). On the importance of phenology in the Miombo ecosystem: Evaluation of open-source satellite evaporation models. *Hydrology and Earth System Sciences Discussions, 2022*, 1–42.

APPENDIX I: GEOSPATIAL TOOL DEVELOPMENT

This section of the report will outline the procedure of how the geospatial tool was developed on the Google Earth Engine (GEE) cloud processing platform to reduce the costs of data storage, processing, and analysis. Google Earth Engine Code Editor JavaScript API was used for this project. It was accessed using the link: code.earthengine.google.com. Code Editor is used for interactive algorithm development with instant access to petabytes of data. It is used for writing and running scripts, with features designed to make developing complex geospatial workflows fast and easy. To begin writing and consolidating the scripts, a new Code Editor was opened under the specified Cloud Project.

Google Earth Engine (GEE) is a cloud-based platform designed for planetary-scale environmental data analysis. It provides access to a vast repository of satellite imagery and geospatial datasets, enabling researchers and practitioners to conduct complex analyses without the need for extensive local computational resources. The scripts can be written using either Python or JavaScript programming languages. For this project, coding was done using the JavaScript programming language in the Earth Engine Code Editor.

1. Before using GEE, a user is required to have a gmail email account, which they will need to use to register their GEE account. To register, access the GEE through its link: https://code.earthengine.google.com/register

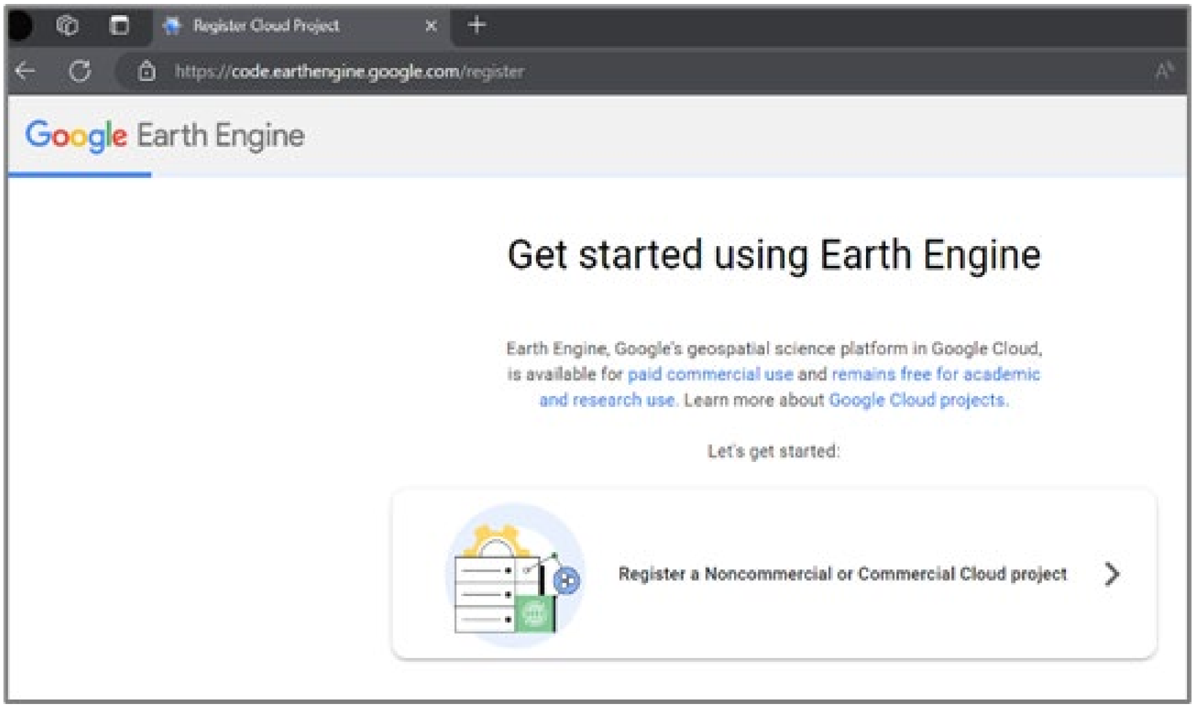

Get started using Earth Engine

Earth Engine, Google's geospatial science platform in Google Cloud, is available for paid commercial use and remains free for academic and research use. Learn more about Google Cloud projects.

Let's get started:

Register a Noncommercial or Commercial Cloud project

2. Click on Register a Noncommercial or Commercial Cloud Project, where you will be directed to a page where you select how you intend to use EE. We selected Government-Research, certain agencies.

   Click next.

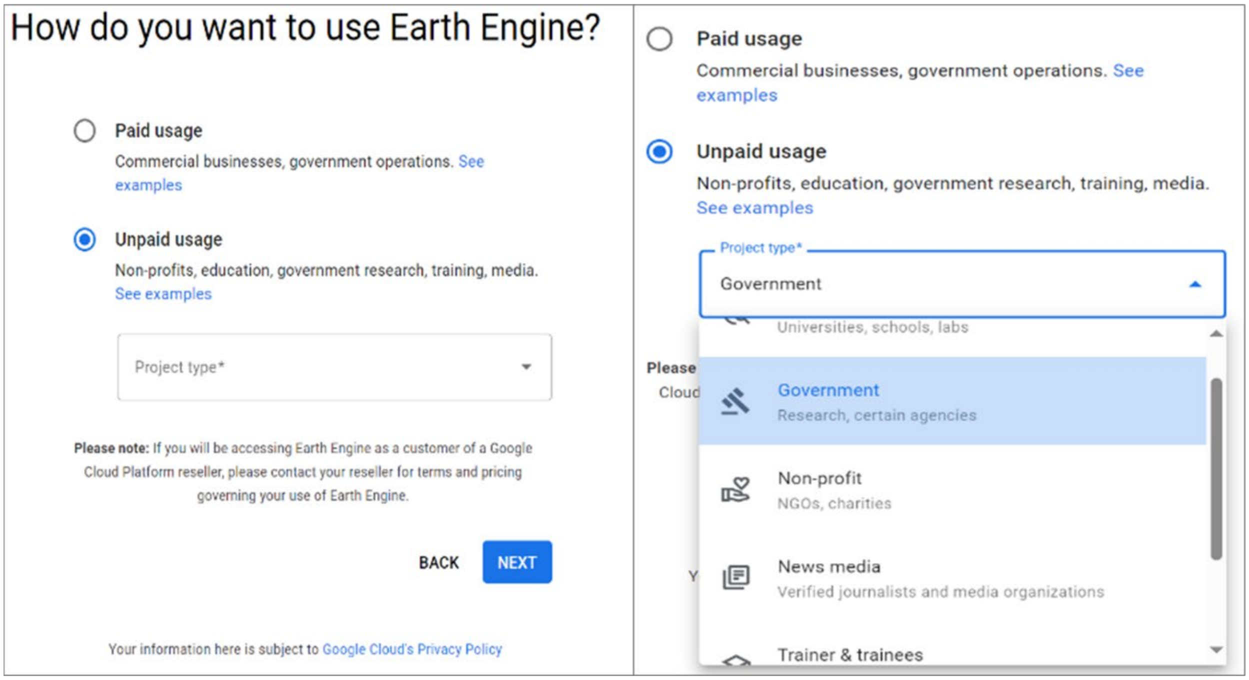

How do you want to use Earth Engine?

○ **Paid usage**
Commercial businesses, government operations. See examples

● **Unpaid usage**
Non-profits, education, government research, training, media.
See examples

Project type*

Please note: If you will be accessing Earth Engine as a customer of a Google Cloud Platform reseller, please contact your reseller for terms and pricing governing your use of Earth Engine.

Your information here is subject to Google Cloud's Privacy Policy

○ **Paid usage**
Commercial businesses, government operations. See examples

● **Unpaid usage**
Non-profits, education, government research, training, media.
See examples

Project type*: Government

3. The next page is where you define or create a new project or choose an existing Google Cloud Project. When you select- Create a new Google Cloud Project, the default Project ID will be in the form of ee-your gmail username. At this point, you may change your Project ID to a different name.

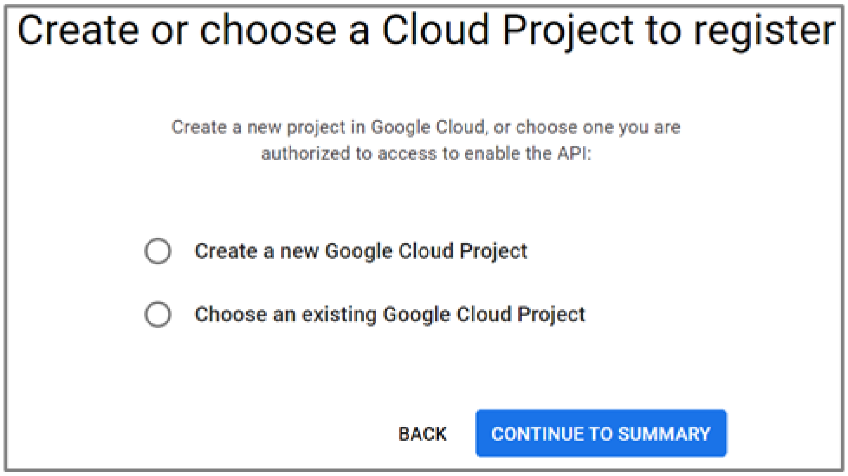

Create or choose a Cloud Project to register

Create a new project in Google Cloud, or choose one you are authorized to access to enable the API:

○ Create a new Google Cloud Project

○ Choose an existing Google Cloud Project

4. Click – Continue to summary, where you will be directed to click and read the Cloud Terms and Conditions.

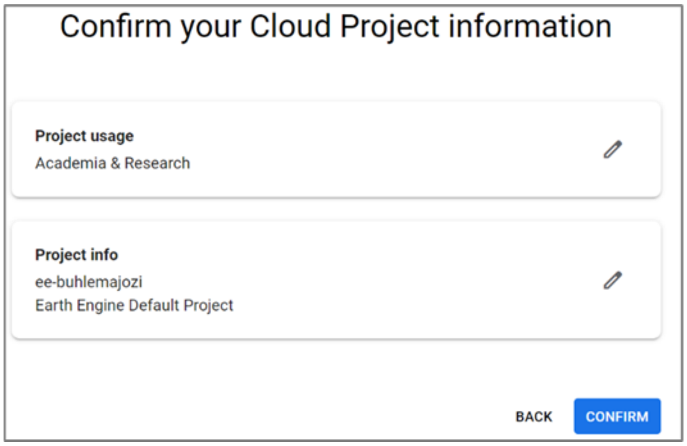

Confirm your Cloud Project information

Project usage
Academia & Research

Project info
ee-buhlemajozi
Earth Engine Default Project

5. Click confirm to complete your registration. You will be redirected to the Code Editor.

Next, we need to set up a service account for the project we are working on.

6. Under the Assets tab and the Cloud Assets, click on the project ID you intend to work on to access the Cloud Project home page for further setup.

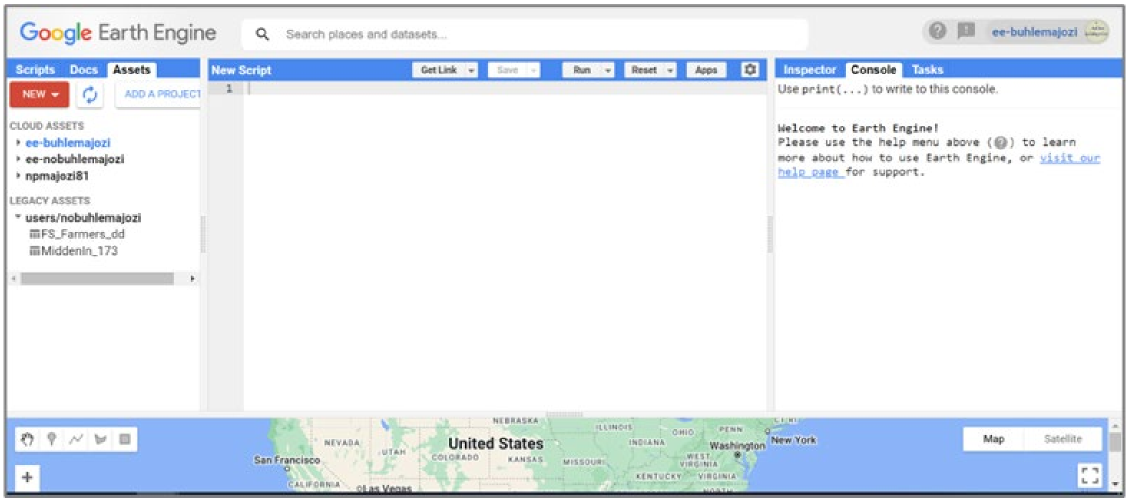

Use print(...) to write to this console.

```
Welcome to Earth Engine!
Please use the help menu above (?) to learn
more about how to use Earth Engine, or visit our
help page for support.
```

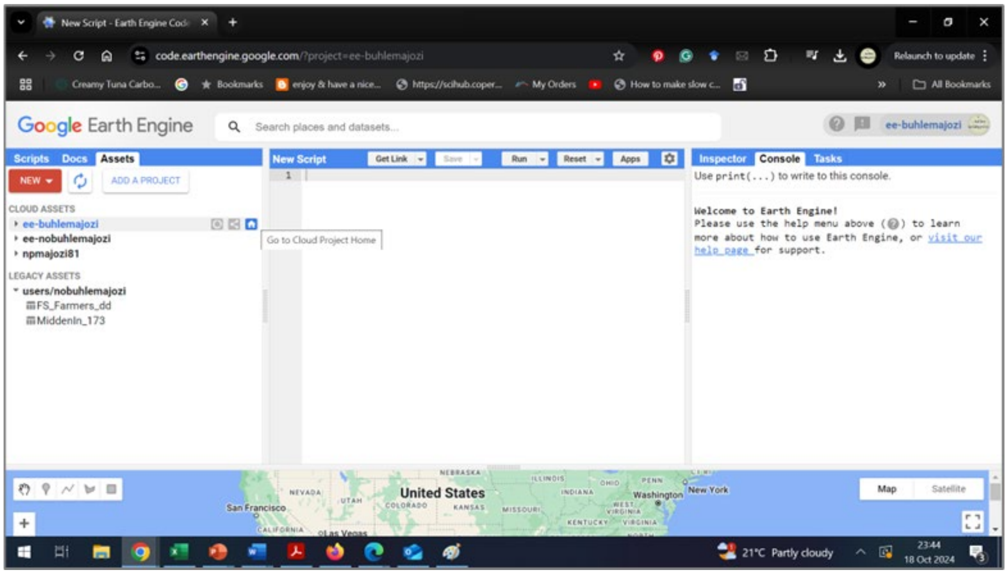

Use print(...) to write to this console.

Welcome to Earth Engine!
Please use the help menu above (?) to learn more about how to use Earth Engine, or visit our help page for support.

7. On the Cloud console, https://console.cloud.google.com/home/, select the project you are working on. Under its Project info, click on the Go to Project tab.

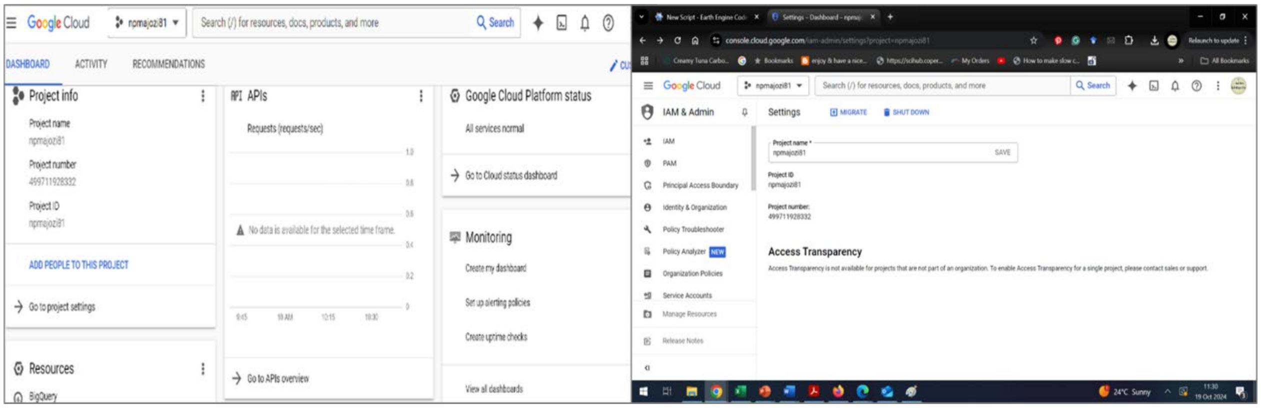

Project name
npmajozi81

Project number
499711928332

Project ID
npmajozi81

Requests (requests/sec)

No data is available for the selected time frame.

All services normal

8. Under the IAM & Admin menu, select Service Accounts.

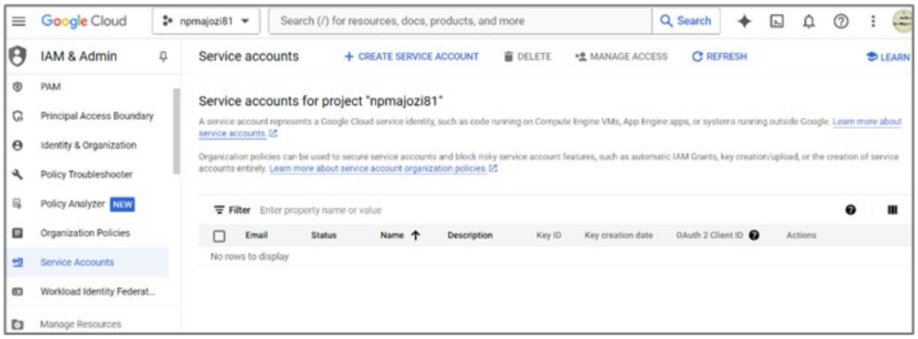

Service accounts for project "npmajozi81"

A service account represents a Google Cloud service identity, such as code running on Compute Engine VMs, App Engine apps, or systems running outside Google. Learn more about service accounts.

Organization policies can be used to secure service accounts and block risky service account features, such as automatic IAM Grants, key creation/upload, or the creation of service accounts entirely. Learn more about service account organization policies.

Filter Enter property name or value

☐	Email	Status	Name ↑	Description	Key ID	Key creation date	OAuth 2 Client ID	Actions

No rows to display

9. Click on the + Create Service Account link. You will be directed to the service account details. Type in the details as required, including a brief description of the project.

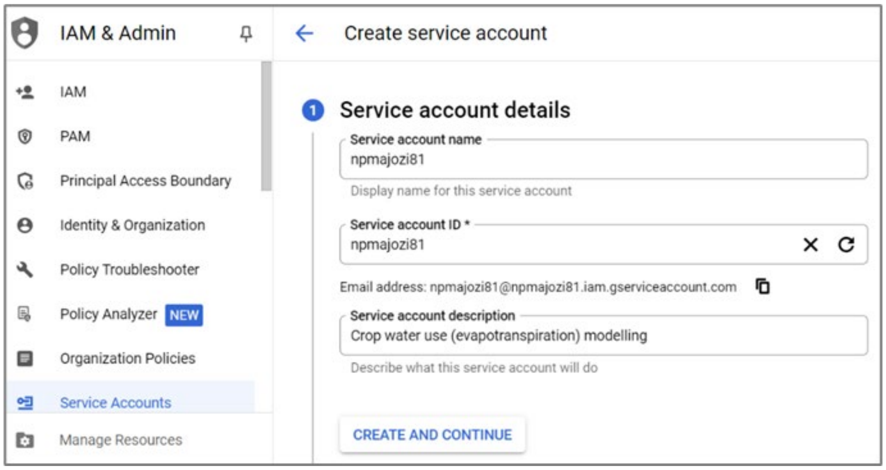

Service account details

Service account name: npmajozi81

Display name for this service account

Service account ID *: npmajozi81

Email address: npmajozi81@npmajozi81.iam.gserviceaccount.com

Service account description: Crop water use (evapotranspiration) modelling

Describe what this service account will do

10. Click the Create and Continue button.
11. On number 2-Grant this service account access to the project, Role dropdown menu, select Currently used- Owner. Click continue.

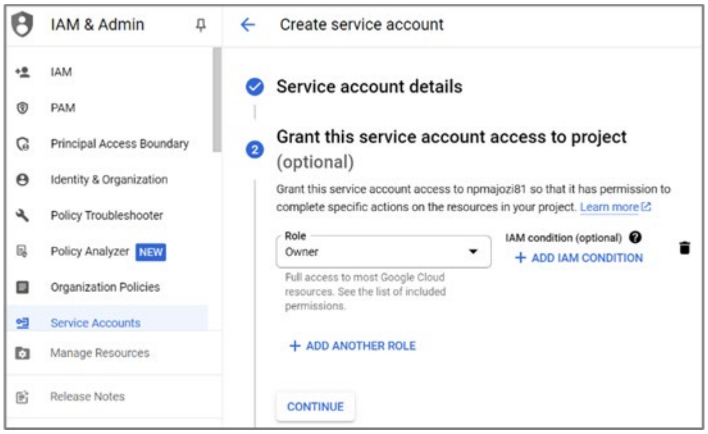

Grant this service account access to project (optional)

Grant this service account access to npmajozi81 so that it has permission to complete specific actions on the resources in your project. Learn more

Role: Owner

Full access to most Google Cloud resources. See the list of included permissions.

IAM condition (optional)

12. On number 3 of the menu, click done. This will translate to your service account looking as follows:

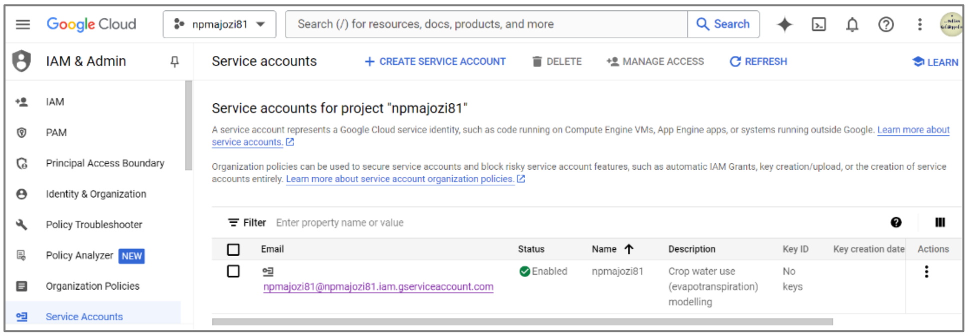

Service accounts for project "npmajozi81"

A service account represents a Google Cloud service identity, such as code running on Compute Engine VMs, App Engine apps, or systems running outside Google. Learn more about service accounts.

Organization policies can be used to secure service accounts and block risky service account features, such as automatic IAM Grants, key creation/upload, or the creation of service accounts entirely. Learn more about service account organization policies.

☐	Email	Status	Name ↑	Description	Key ID	Key creation date	Actions
☐	npmajozi81@npmajozi81.iam.gserviceaccount.com	✓ Enabled	npmajozi81	Crop water use (evapotranspiration) modelling	No keys		⋮

13. Click the three dots under Actions and select Manage Keys.

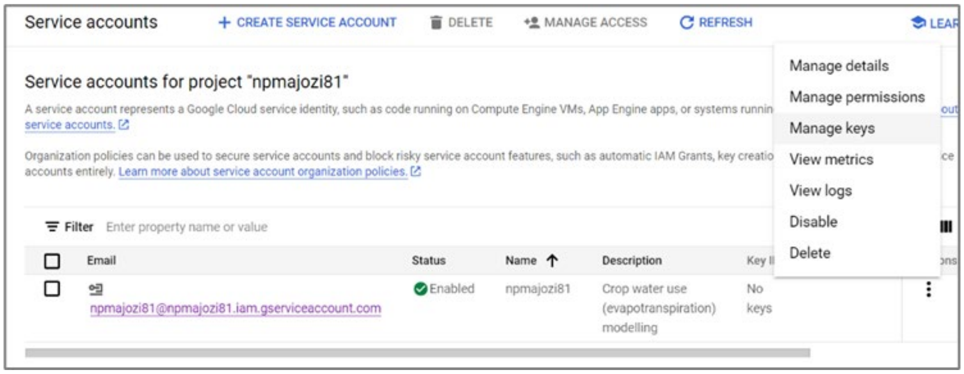

Service accounts for project "npmajozi81"

A service account represents a Google Cloud service identity, such as code running on Compute Engine VMs, App Engine apps, or systems runnin service accounts.

Organization policies can be used to secure service accounts and block risky service account features, such as automatic IAM Grants, key creatio accounts entirely. Learn more about service account organization policies.

Email	Status	Name	Description	Key I
npmajozi81@npmajozi81.iam.gserviceaccount.com	Enabled	npmajozi81	Crop water use (evapotranspiration) modelling	No keys

14. Click the ADD KEY button and choose to Create a new Key

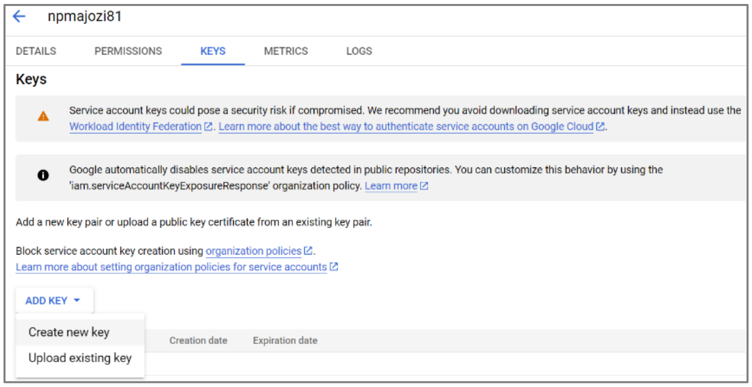

Keys

Service account keys could pose a security risk if compromised. We recommend you avoid downloading service account keys and instead use the Workload Identity Federation. Learn more about the best way to authenticate service accounts on Google Cloud.

Google automatically disables service account keys detected in public repositories. You can customize this behavior by using the 'iam.serviceAccountKeyExposureResponse' organization policy. Learn more

Add a new key pair or upload a public key certificate from an existing key pair.

Block service account key creation using organization policies.
Learn more about setting organization policies for service accounts

15. Select the default JSON setting. Click Create.

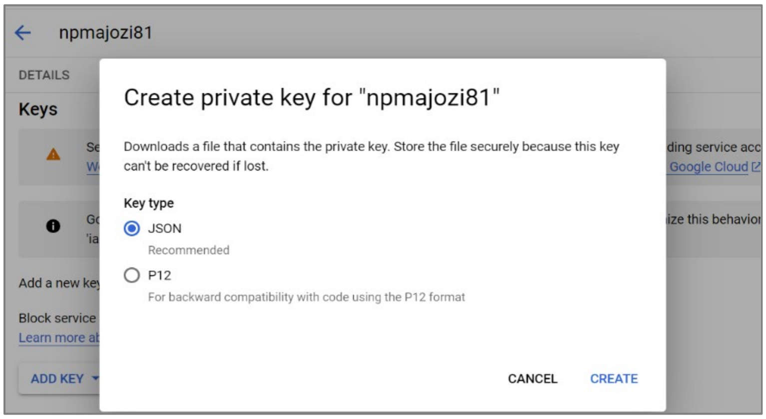

Create private key for "npmajozi81"

Downloads a file that contains the private key. Store the file securely because this key can't be recovered if lost.

Key type

● JSON
Recommended

○ P12
For backward compatibility with code using the P12 format

16. A pop-up message will confirm the key was created and has been saved in the local computer download folder. Click close.

17. Back on the Cloud Project Home, select Go to APIs overview, which will take you to API’s & Services

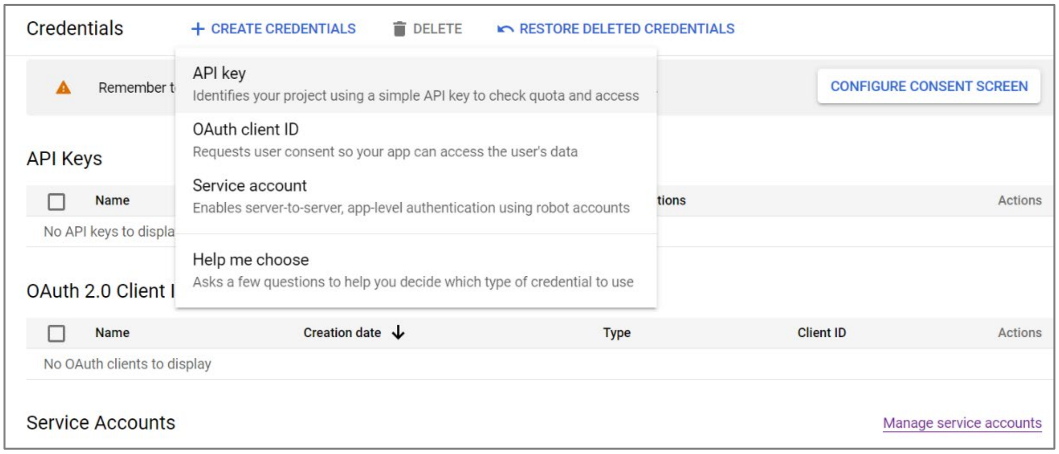

18. On the API’s & Services menu, select + Create Credentials, and on the dropdown menu, select API key

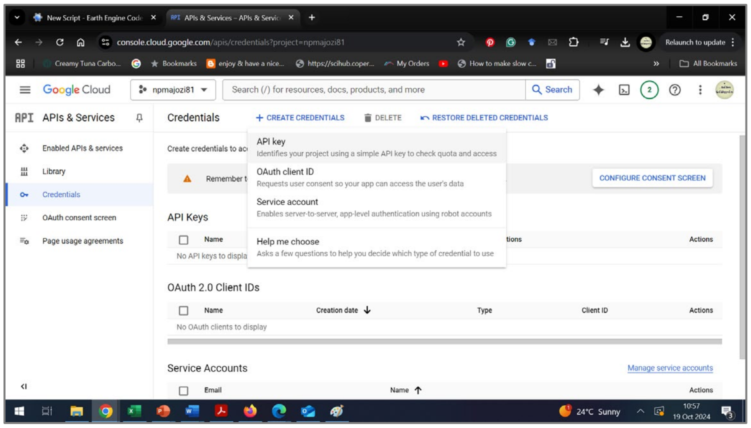

19. If the API key was successfully created, you will see a pop-up window as shown below:

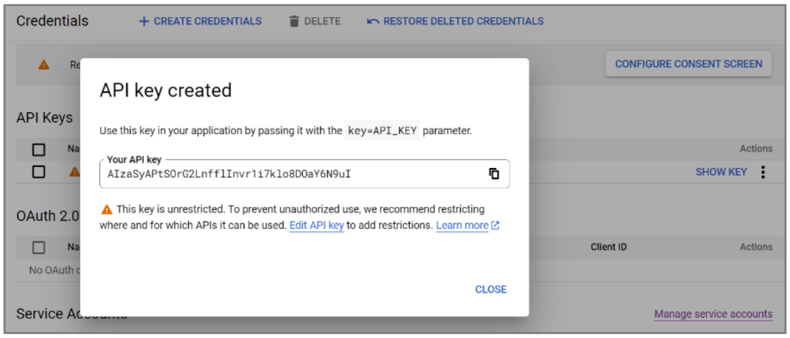

API key created

Use this key in your application by passing it with the `key=API_KEY` parameter.

Your API key: AIzaSyAPtSOrG2LnfflInvr1i7klo8DOaY6N9uI

This key is unrestricted. To prevent unauthorized use, we recommend restricting where and for which APIs it can be used. Edit API key to add restrictions. Learn more

20. Click Close. The API key will be displayed under API Keys on the Credentials screen.

21. The next step is to permit the roles that grant access for the project. Return to the Cloud Console Dashboard and navigate to the IAM & Admin pane. Click Roles

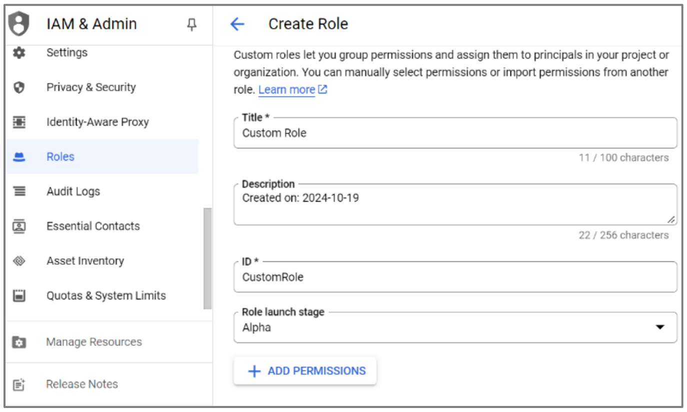

Create Role

Custom roles let you group permissions and assign them to principals in your project or organization. You can manually select permissions or import permissions from another role. Learn more

Title *
Custom Role
11 / 100 characters

Description
Created on: 2024-10-19
22 / 256 characters

ID *
CustomRole

Role launch stage
Alpha

22. Click the +ADD PERMISSIONS button. Select all *access approval* options. Click the Add button. Click CREATE.

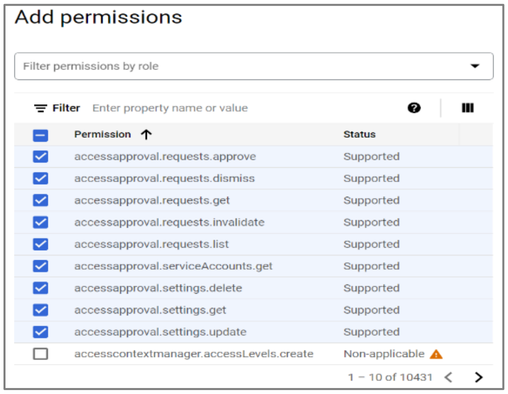

Add permissions

	Permission ↑	Status
☑	accessapproval.requests.approve	Supported
☑	accessapproval.requests.dismiss	Supported
☑	accessapproval.requests.get	Supported
☑	accessapproval.requests.invalidate	Supported
☑	accessapproval.requests.list	Supported
☑	accessapproval.serviceAccounts.get	Supported
☑	accessapproval.settings.delete	Supported
☑	accessapproval.settings.get	Supported
☑	accessapproval.settings.update	Supported
☐	accesscontextmanager.accessLevels.create	Non-applicable ⚠

1 – 10 of 10431

After the approval of the service account, it can be used for GEE applications.

Geospatial tool development

Google Earth Engine Code Editor JavaScript API was used for this project. It was accessed using the link: code.earthengine.google.com. Code Editor is used for interactive algorithm development with instant access to petabytes of data. It is used for writing and running scripts, with features designed to make developing complex geospatial workflows fast and easy.

To begin writing and consolidating the scripts, a new Code Editor was opened under the specified Cloud Project.

Data Acquisition

GEE hosts a huge repository of geospatial datasets, including satellite imagery, climate and vector data. These can be accessed through the GEE Data Catalogue, https://developers.google.com/earth-engine/datasets/.

For this purpose, multiple datasets were used to extract the inputs for modelling evapotranspiration:

Dataset	Input
Sentinel 2	NDVI/ EVI, surface albedo
MODIS	land surface temperature, surface emissivity
ECMWF	air temperature, wind speed, and atmospheric pressure
STRM	DEM- Elevation

For datasets that are available in the Data Catalogue, they are searched as shown:

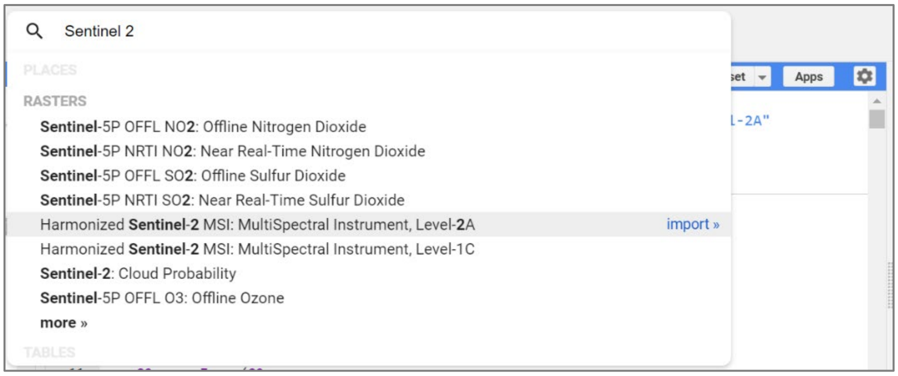

Sentinel 2

- **Sentinel**-5P OFFL NO**2**: Offline Nitrogen Dioxide
- **Sentinel**-5P NRTI NO**2**: Near Real-Time Nitrogen Dioxide
- **Sentinel**-5P OFFL SO**2**: Offline Sulfur Dioxide
- **Sentinel**-5P NRTI SO**2**: Near Real-Time Sulfur Dioxide
- Harmonized **Sentinel-2** MSI: MultiSpectral Instrument, Level-**2**A
- Harmonized **Sentinel-2** MSI: MultiSpectral Instrument, Level-1C
- **Sentinel-2**: Cloud Probability
- **Sentinel**-5P OFFL O3: Offline Ozone

Select the version you want to import to the Code Editor and click import. In this case, we imported Harmonised Sentinel-2 MSI: MultiSpectral Instrument, Level 2A, to compute surface albedo, and vegetation indices to derive leaf area index, fraction of vegetation cover. Other satellite data products that were imported are MOD11A1.061 Terra Land Surface Temperature and Emissivity Daily Global 1km, to extract land surface temperature and surface emissivity. For the meteorological data inputs, air temperature, wind speed and atmospheric pressure, we imported ERA5-Land Daily Aggregated - ECMWF Climate Reanalysis from the European Centre for Medium-Range Weather Forecasts (ECMWF).

Other geospatial datasets from the user were imported, for example, the region of interest- i.e. the farms that are being used for piloting the study. This is accomplished by navigating to the

"Assets" tab in Code Editor, clicking on New, and select the file type you intend to import. The next step is to select the source files to navigate to where the files are saved.

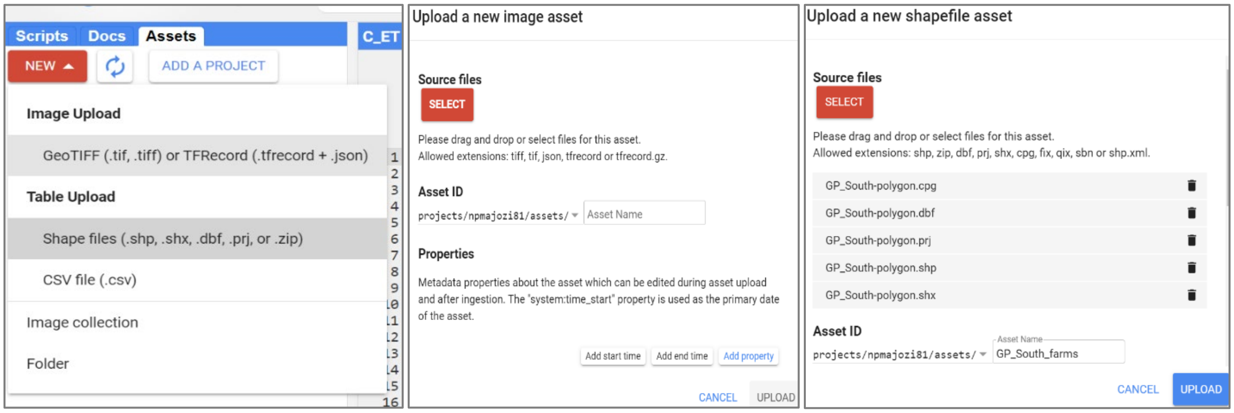

Please drag and drop or select files for this asset.
Allowed extensions: tiff, tif, json, tfrecord or tfrecord.gz.

Asset ID: projects/npmajozi81/assets/

Metadata properties about the asset which can be edited during asset upload and after ingestion. The "system:time_start" property is used as the primary date of the asset.

Please drag and drop or select files for this asset.
Allowed extensions: shp, zip, dbf, prj, shx, cpg, fix, qix, sbn or shp.xml.

GP_South-polygon.cpg
GP_South-polygon.dbf
GP_South-polygon.prj
GP_South-polygon.shp
GP_South-polygon.shx

Asset ID: projects/npmajozi81/assets/ GP_South_farms

Data preprocessing

Before modelling can be done, the region of interest (ROI), together with the period of modelling, must be defined. The region of interest in this case was defined using the farms' boundaries that were imported.

The modelling, particularly for crop water use, was focused on the summer maize crop growing season, since the study is for rainfed agriculture. We set the modelling season start time to December and the season end to April.

```
// Beginning and end of season
var seasonStart = 12;                    //month in numerical value
var seasonEnd = 4;
var LTstart = '2023-12-01';
var LTend = '2024-04-30';
```

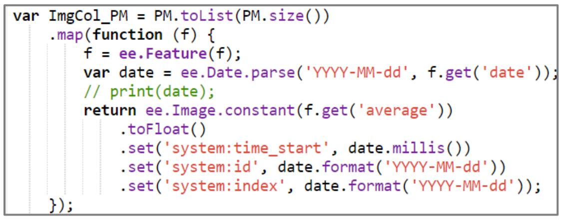

```
var ImgCol_PM = PM.toList(PM.size())
    .map(function (f) {
        f = ee.Feature(f);
        var date = ee.Date.parse('YYYY-MM-dd', f.get('date'));
        // print(date);
        return ee.Image.constant(f.get('average'))
            .toFloat()
            .set('system:time_start', date.millis())
            .set('system:id', date.format('YYYY-MM-dd'))
            .set('system:index', date.format('YYYY-MM-dd'));
    });
```

This is followed by preprocessing satellite imagery and extracting the required input variables. This included:

- Cloud masking
- Temporal filtering- this was done to extract data for mapping crop water use during the growing season only
- Selecting the bands that would be used for further analysis.

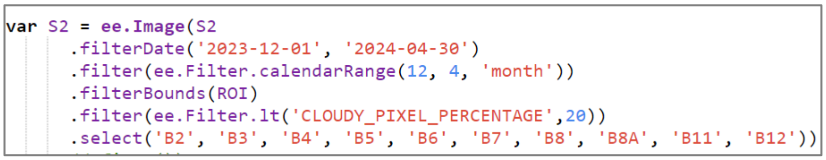

```
var S2 = ee.Image(S2
        .filterDate('2023-12-01', '2024-04-30')
        .filter(ee.Filter.calendarRange(12, 4, 'month'))
        .filterBounds(ROI)
        .filter(ee.Filter.lt('CLOUDY_PIXEL_PERCENTAGE',20))
        .select('B2', 'B3', 'B4', 'B5', 'B6', 'B7', 'B8', 'B8A', 'B11', 'B12'))
```

Other input variables, like the vegetation indices, need to be computed from the satellite imagery. This was done as the next step.

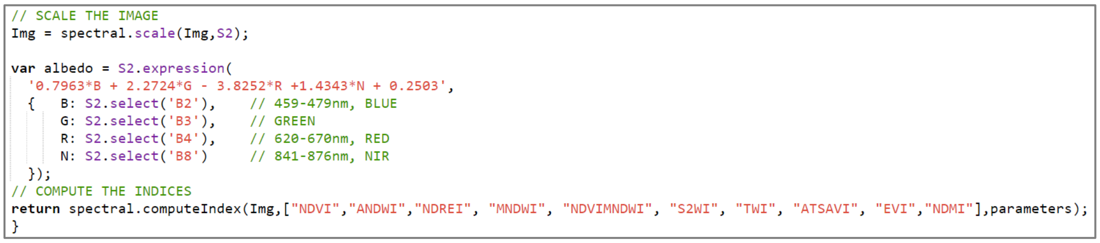

```
// SCALE THE IMAGE
Img = spectral.scale(Img,S2);

var albedo = S2.expression(
  '0.7963*B + 2.2724*G - 3.8252*R +1.4343*N + 0.2503',
  {   B: S2.select('B2'),    // 459-479nm, BLUE
      G: S2.select('B3'),    // GREEN
      R: S2.select('B4'),    // 620-670nm, RED
      N: S2.select('B8')     // 841-876nm, NIR
  });
// COMPUTE THE INDICES
return spectral.computeIndex(Img,["NDVI","ANDWI","NDREI", "MNDWI", "NDVIMNDWI", "S2WI", "TWI", "ATSAVI", "EVI","NDMI"],parameters);
}
```

Model integration into GEE

Delineated fields

After data preparation and preprocessing, crop field delineation was done within the study area in Vereeniging. Deep learning techniques, i.e. Convolutional Neural Networks, were employed to delineate the different crop fields based on the spectral characteristics derived from the satellite imagery (Yao et al., 2022; Imanni et al., 2022). Our study compared the performance of Superpixel CNNs and Multi-Dimensional Fully Convolutional Networks (MD-FCNs) in delineating the field parcels. The results showed that the MD-FCNs were much superior in identifying the field boundaries. GEE's built-in functions facilitate the application of these algorithms, allowing for efficient processing of large datasets (Wang, 2023; Shelestov et al., 2017).

The resulting field boundaries were then uploaded to GEE to give the study area outline, as shown in Figure 21 below.

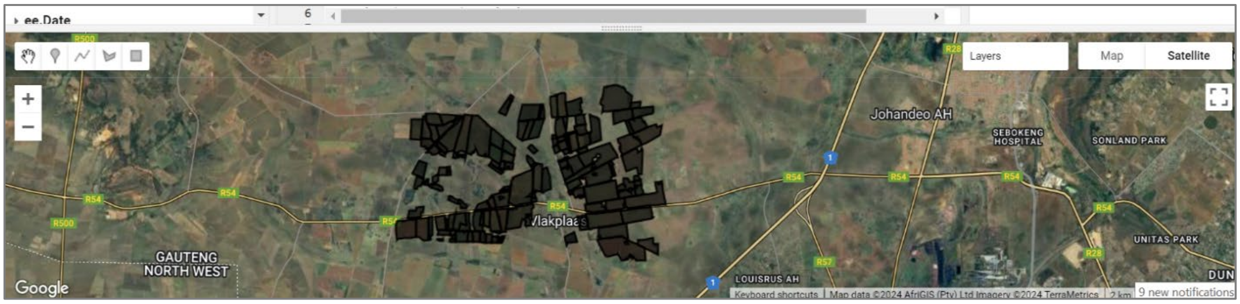

Figure 21: Pilot site loaded onto GEE for ET estimation

Crop water use mapping

To effectively monitor crop water use, it is important to estimate evapotranspiration (ET). Remote sensing methods have been utilised to estimate ET by using different input variables, such as vegetation indices, land surface temperature and meteorological data (Hang et al., 2023; Safdar et al., 2023). For instance, the use of NDVI time series data can help in assessing the phenological stages of crops, whereas thermal data are used to estimate crop temperature, which is critical for accurate water use estimation (Shi et al., 2023; Hang et al., 2023). Additionally, integrating crop models with remote sensing data can enhance the understanding of water consumption patterns and stress detection in crops (Cao et al., 2020).

To estimate crop evapotranspiration, the Penman-Monteith algorithm is being employed in our study site. The algorithm was converted from MATLAB language it was initially written in, to JavaScript for application in GEE. Multiple satellite and meteorological datasets are being used for input variables. For instance, vegetation indices and surface albedo are being retrieved from Sentinel 2 MSI imagery.

The first step was to define and call the model input variables, parameters and constants.

```
img           = ee.Image(img);
//var q         = img.select('q');     // Specific humidity (kg/kg);
var rho       = img.select('rho');

var Pair      = img.select('Pa');        // kPa
var U         = img.select('U');         // m/s
var Tmax      = img.select('Tmax');      // degC
var Tmin      = img.select('Tmin');      // degC
var Tavg      = img.select('Tavg');      // degC

var Rnl       = img.select('Rln');
var Rns        = img.select('Rsn');

var albedo    = img.select('albedo');  // %
var emiss     = img.select('Emiss');   // %
var LST       = img.select('LST_Day_1km');
```

Penman-Monteith model parameters were then estimated from the input variables.

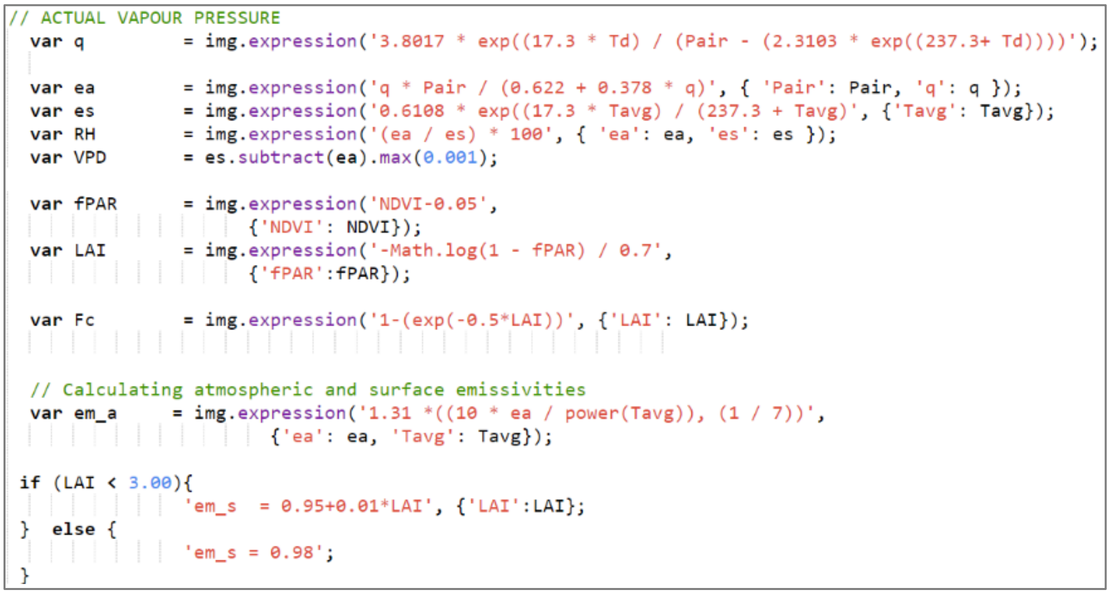

```
// ACTUAL VAPOUR PRESSURE
  var q         = img.expression('3.8017 * exp((17.3 * Td) / (Pair - (2.3103 * exp((237.3+ Td))))');

  var ea        = img.expression('q * Pair / (0.622 + 0.378 * q)', { 'Pair': Pair, 'q': q });
  var es        = img.expression('0.6108 * exp((17.3 * Tavg) / (237.3 + Tavg)', {'Tavg': Tavg});
  var RH        = img.expression('(ea / es) * 100', { 'ea': ea, 'es': es });
  var VPD       = es.subtract(ea).max(0.001);

  var fPAR      = img.expression('NDVI-0.05',
                      {'NDVI': NDVI});
  var LAI       = img.expression('-Math.log(1 - fPAR) / 0.7',
                      {'fPAR':fPAR});

  var Fc        = img.expression('1-(exp(-0.5*LAI))', {'LAI': LAI});


  // Calculating atmospheric and surface emissivities
  var em_a     = img.expression('1.31 *((10 * ea / power(Tavg)), (1 / 7))',
                        {'ea': ea, 'Tavg': Tavg});

 if (LAI < 3.00){
               'em_s  = 0.95+0.01*LAI', {'LAI':LAI};
 }  else {
               'em_s = 0.98';
 }
```

Finally, components of evapotranspiration were computed, and total evapotranspiration was determined.

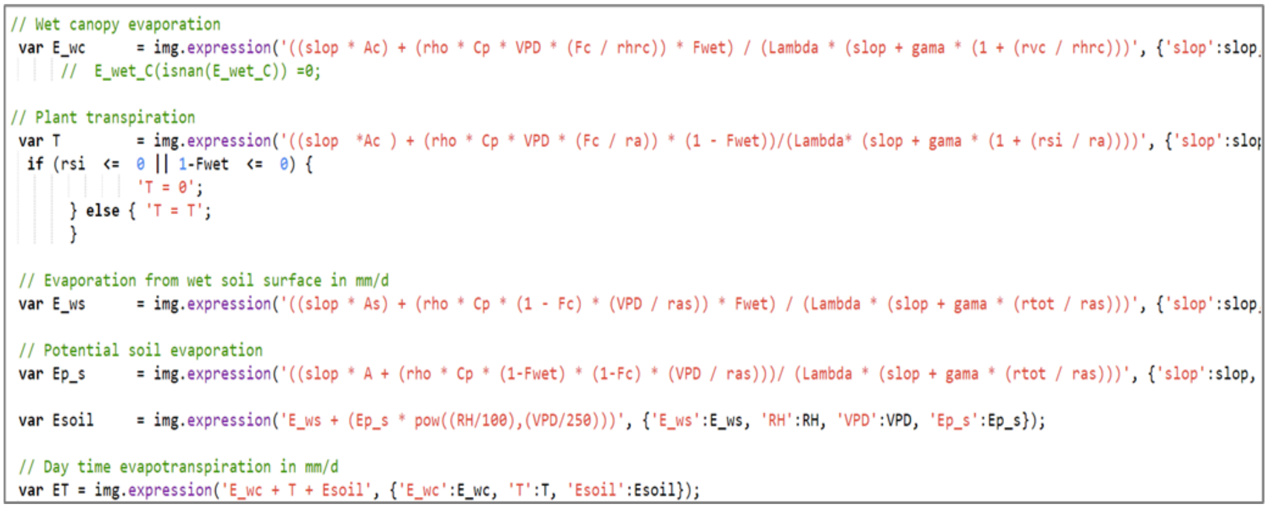

```
// Wet canopy evaporation
 var E_wc      = img.expression('((slop * Ac) + (rho * Cp * VPD * (Fc / rhrc)) * Fwet) / (Lambda * (slop + gama * (1 + (rvc / rhrc)))', {'slop':slop
     //  E_wet_C(isnan(E_wet_C)) =0;

// Plant transpiration
 var T         = img.expression('((slop  *Ac ) + (rho * Cp * VPD * (Fc / ra)) * (1 - Fwet))/(Lambda* (slop + gama * (1 + (rsi / ra))))', {'slop':slop
  if (rsi  <=  0 || 1-Fwet  <=  0) {
           'T = 0';
     } else { 'T = T';
     }

 // Evaporation from wet soil surface in mm/d
 var E_ws      = img.expression('((slop * As) + (rho * Cp * (1 - Fc) * (VPD / ras)) * Fwet) / (Lambda * (slop + gama * (rtot / ras)))', {'slop':slop

 // Potential soil evaporation
 var Ep_s      = img.expression('((slop * A + (rho * Cp * (1-Fwet) * (1-Fc) * (VPD / ras)))/ (Lambda * (slop + gama * (rtot / ras)))', {'slop':slop,

 var Esoil     = img.expression('E_ws + (Ep_s * pow((RH/100),(VPD/250)))', {'E_ws':E_ws, 'RH':RH, 'VPD':VPD, 'Ep_s':Ep_s});

 // Day time evapotranspiration in mm/d
 var ET = img.expression('E_wc + T + Esoil', {'E_wc':E_wc, 'T':T, 'Esoil':Esoil});
```

Map Product Visualisation

GEE provides tools for visualising processed data, enabling users to create interactive maps and dashboards that display crop water use metrics over time (Wijaya, 2023). This visualisation is crucial for stakeholders in agriculture, as it allows for real-time monitoring and decision-making regarding irrigation practices and resource management (Ali, 2023). Furthermore, the ability to analyse temporal changes in crop conditions can help identify areas experiencing water stress, thereby facilitating timely interventions (Dangwal et al., 2015).

The next step after ensuring your model script is debugged and running is to create interactive map product layers of ET, and its components- soil evaporation, interception, and transpiration. This is done by defining your user interface (UI).

```
// Create a panel with vertical flow layout.
var panel = ui.Panel({
  layout: ui.Panel.Layout.flow('vertical'),
  style: {width: '350px'}
}).add(ui.Label(
  'Steps to Follow:\n1)Select growing season,\n2)Select field,\n3)Wait for time series graph to load\n4)Click a bar/date within the graph to view the respective image
  {whiteSpace:'pre'}));

////////////// Seasons selector
// Define Seasons/Dates
var Seasons = {
  '2018/2019': ['2018-12-01','2019-04-30'],
  '2019/2020': ['2019-12-01','2020-04-30'],
  '2020/2021': ['2020-12-01','2021-04-30'],
  '2021/2022': ['2021-12-01','2022-04-30'],
  '2022/2023': ['2022-12-01','2023-04-30'],
  '2023/2024': ['2023-12-01','2024-04-30']};

// Define dummy variable that will store selector output (i.e. season start and end dates)
var selDates;
var s2_ET;
```

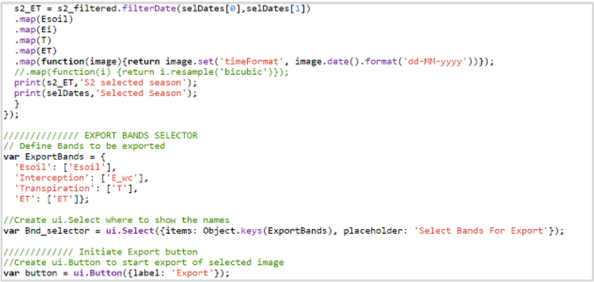

```
  s2_ET = s2_filtered.filterDate(selDates[0],selDates[1])
  .map(Esoil)
  .map(Ei)
  .map(T)
  .map(ET)
  .map(function(image){return image.set('timeFormat', image.date().format('dd-MM-yyyy'))});
  //.map(function(i) {return i.resample('bicubic')});
  print(s2_ET,'S2 selected season');
  print(selDates,'Selected Season');
  }
});

////////////// EXPORT BANDS SELECTOR
// Define Bands to be exported
var ExportBands = {
  'Esoil': ['Esoil'],
  'Interception': ['E_wc'],
  'Transpiration': ['T'],
  'ET': ['ET']};

//Create ui.Select where to show the names
var Bnd_selector = ui.Select({items: Object.keys(ExportBands), placeholder: 'Select Bands For Export'});

///////////// Initiate Export button
//Create ui.Button to start export of selected image
var button = ui.Button({label: 'Export'});
```

You may further add time series graphs of the parameters, summaries, and user configurable options for selecting which field they want to view, including the parameters they want to export.

```
};

///////// UI Setup ///////////////////////////////////////////////////

// Create a panel with vertical flow layout.
var panel = ui.Panel({
  layout: ui.Panel.Layout.flow('vertical'),
  style: {width: '300px'}
}).add(ui.Label(
  'Steps to follow:\n1)Select growing season,\n2)Select field,\n3)Wait for time series graph to load\n4)Click a bar
  {whiteSpace:'pre'}));

```

```
Click on the map to
inspect the layers.
```

EE-PM

is app estimates components of total
apotranspiration of selected crop fields-
il evaporation, crop transpiration, and
terception. These are calculated, displayed,
d can be exported per field:

il evaporation
op transpiration
terception
tal evapotranspiration

Steps to follow:
1)Select growing season,
2)Select field,
3)Wait for time series graph to load
4)Click a bar/date within the graph to view the
5)Click on areas of interest within the image t
6)Select the product for export, then click "Ex

APPENDIX II: CAPACITY BUILDING

One PhD student, Ms Ntanganedzeni Badana, was enrolled at the University of Pretoria under the project. She is working under the supervision of Prof Ramoelo and Dr Majozi on a full-time basis. Her research is focused on using remote sensing models for maize crop evapotranspiration estimation. She has completed her knowledge review paper focusing on remote sensing-based ET models for maize crop water use, as a first manuscript. She has completed the analysis for her second objective- evaluating maize crop ET in rainfed fields.

APPENDIX III: LINKED OUTPUTS

Mthethwa et. al. Review of Remote Sensing Based Techniques for Estimating Evapotranspiration and Their Applicability in Maize Croplands (in preparation)

Mthethwa et. al. Evaluating remote sensing-based evapotranspiration models and products in the Maize Triangle region of South Africa (in preparation)

APPENDIX IV: ACCESS TO THE DATA GENERATED DURING THE PROJECT

All the data that was collected as part of this project is stored (electronic and hard copy) and is accessible from the Council for Scientific and Industrial Research. Kindly contact Dr. Majozi at nmajozi@csir.co.za to gain access to the data.